DESIGN, DEVELOPMENT, AND CHARACTERIZATION OF A PROTOTYPE DIGITAL MAMMOGRAPHY SYSTEM

A Thesis
Presented to
The Academic Faculty

by

Sankararaman Suryanarayanan

In Partial Fulfillment
of the Requirements for the Degree
Doctor of Philosophy in the
School of Biomedical Engineering

Georgia Institute of Technology
May 2006

DESIGN, DEVELOPMENT, AND CHARACTERIZATION OF A PROTOTYPE DIGITAL MAMMOGRAPHY SYSTEM

Approved by:

Dr. Andrew Karellas, Advisor
Department of Radiology
Emory University
School of Biomedical Engineering
Georgia Institute of Technology

Dr. John N. Oshinski
School of Biomedical Engineering
Georgia Institute of Technology
Department of Radiology
Emory University

Dr. Xiaoping P. Hu
School of Biomedical Engineering
Georgia Institute of Technology
Emory University

Dr. Carl J. D'Orsi
Department of Radiology
Emory University

Dr. Ernest V. Garcia
Department of Radiology
Emory University
School of Biomedical Engineering
Georgia Institute of Technology

Date Approved: March 29, 2006

This thesis is dedicated to the loving memory of my father
Dr. S. Suryanarayanan.

ACKNOWLEDGEMENTS

I wish to express my appreciation and gratitude for the many people who have been a positive influence in my life. Firstly, I thank my advisor Dr. Andrew Karellas for being my mentor, colleague, and friend. I feel honored to have worked with such an exceptional scientist of the highest caliber. I will always appreciate his innate quality to inspire me to reach for goals far beyond my comprehension. I am grateful to him for his support, guidance, compassion, generosity, and encouragement.

I thank Dr. Carl D'Orsi for the innumerous discussions and his support for my scientific pursuits. I admire his drive to recognize novel approaches to solve clinical problems and am very appreciative of his efforts in helping me conduct studies related to visual perception. I am very thankful to Dr. Ernest Garcia, Dr. John Oshinski, and Dr. Xiaoping Hu for being flexible and accommodative during this entire process. I also greatly appreciate their comments, suggestions, and advisement.

I wish to express my immense appreciation to my colleagues and friends, Dr. Srinivasan Vedantham and Ioannis Sechopoulos for extending their support to my research efforts. In the same spirit, I thank Ms. Linda Burr and Mr. Christopher Ruffin for their relentless help with all the administrative issues. I would like to specially thank Samantika Subramaniam for her support, affection, encouragement and brightening up my life. I am very appreciative of the technical support provided by Fairchild Imaging Inc., Milpitas, CA during the course of this research and would like to thank Bruce Willy, Francis Pang, Jose Camara, and Steven Onishi for useful discussions and providing technical data during the course of this project.

There are no words that can describe my eternal gratitude to my parents, Dr. Suryanarayanan and Mangala Suryanarayanan. The person I am today is because of their selfless and committed efforts to raise me in the true spirit of life. I owe every success of mine to the innumerable sacrifices that my parents have made. There are many others who have been a source of inspiration, influence, or just been there when I needed them. I wish to share this space to humbly thank them. Thank you.

This study was supported in part by the National Institutes of Health (NIH) grants RO1-CA88792 and RO1-EB002123 from the National Cancer Institute (NCI) and National Institute of Biomedical Imaging and Bioengineering (NIBIB), respectively. Portions of this work were supported by the National Heart, Lung and Blood Institute (NHLBI) and NIBIB grants R01-HL65551 and R01-EB002270 respectively. Some of this work was also supported by an infrastructure grant from the Georgia Cancer Coalition (GCC). The contents are solely the responsibility of the author and do not necessarily represent the official views of the NCI, NHLBI, NIBIB, NIH or GCC.

TABLE OF CONTENTS

LIST OF TABLES

LIST OF FIGURES

LIST OF SYMBOLS AND ABBREVIATIONS

SF	Screen-film
PPV	Positive predictive value
FFDM	Full-field digital mammography
SNR	Signal-to-noise ratio
MRI	Magnetic resonance imaging
DSA	Digital subtraction angiography
LSF	Line spread function
MTF	Modulation transfer function
NPS	Noise power spectrum
NEQ	Noise equivalent quanta
DQE	Detective quantum efficiency
PMMA	Polymethyl-methacrylate
CD	Contrast detail
TFT	Thin film transistor
CMOS	Complementary metal oxide semiconductor
CCD	Charge coupled Device
CR	Computed radiography
IP	Image-phosphor plate
PMT	Photomultiplier tube
TEC	Thermoelectric
DU	Digital units
ROI	Region of interest
AFC	Alternative forced choice

VRF	Human visual response function
HVL	Half value layer
SID	Source-to-imager distance
QE	Quantum efficiency
CsI:Tl	Thallium doped cesium iodide
X	X-ray exposure
mR	X-ray exposure in milli-Roentgen
$\bar{q}_0$	Mean number of x-ray photon fluence (photons/mm^2/mR)
$q_{rel}(E)$	X-ray spectrum normalized normalized to unit area
$\bar{g}_1$	Mean quantum efficiency of phosphor (scintillator)
$\bar{g}_2$	Mean quantum gain
$\bar{g}_4$	Mean fiber optic coupling efficiency
$\bar{g}_5$	Mean CCD quantum and coupling efficiency
t_f	Imager cover plate transmission
a_{pd}	Pixel aperture
ε_{g2}	Poisson excess
$T_3(u,v)$	MTF of phosphor (scintillator)
$T_6(u,v)$	Pixel aperture MTF
$W_8(u,v)$	NPS due to x-ray quanta
$W_{add}(u,v)$	Additive noise
ρ_s	Surface density (mg/cm^2)
f_f	Pixel fill-factor

a_x	Pixel dimension along x-direction
a_y	Pixel dimension along y-direction
p_f	Packing fraction of phosphor scintillator
$W_{CsI:Tl}$	Number of optical photons generated per keV in CsI:Tl
$\mu_{CsI:Tl}$	Attenuation coefficient of CsI:Tl
t	Thickness of scintillator
$\eta_{esc}(z)$	Escape probability
u	Slope parameter
ΔC	Perceived disk thickness
$\phi(t)$	Cumulative Gaussian distribution
M	Number of alternate choices
mGy	X-ray radiation dose in milli-Gray
$pDgN$	Polyenergetic normalized DgN coefficient (mGy/R)
$\phi(E)$	Incident spectra
$\vartheta(E)$	Photon fluence to exposure conversion factor (mR/photons/mm^2)
ς	Probability of K-shell interaction
ω	Fluorescence yield
f_K	K-absorption probability
m_A	Mean gain along path A
m_B	Mean gain along path B
m_C	Mean gain along path C
$T_K(u,v)$	Stochastic blur of K-fluorescence x-rays
E_K	K-edge of CsI:Tl

SUMMARY

Breast cancer is a major health concern in the United States. Mammography is the 'gold standard' for screening breast cancer and screen-film technology is still widely used in the screening for breast cancer. However, screen-film systems have limited dynamic range and contrasts compared to digital systems, and do not offer integrated image processing capabilities. Recently, digital mammography has seen an upsurge in clinical adoption but current digital mammography systems are limited in terms of their spatial resolution. Therefore, high-resolution digital mammography systems with superior signal-to-noise ratio and contrast characteristics need to be explored.

A monolithic, single module high-resolution (39-μm) digital x-ray platform (Fairchild Imaging Inc., Milpitas, CA) was developed and characterized for digital mammography. The architecture was extended to a large area (16 x 24-cm) multi-module solid-state imager with variable resolution (39 and 78-μm). In addition, a four module (16 x 16-cm) imaging architecture with 78-μm pixel was explored for high-resolution contrast enhanced digital mammography for the detection of malignancy-associated angiogenesis. Simulations based on the cascaded linear systems framework were performed in order to characterize the physical properties of the imaging platforms such as the modulation transfer function (MTF), noise power spectra (NPS), and detective quantum efficiency (DQE). Experimental measurements of imager performance was also conducted and compared to model predicted results. Further, perceptual analysis of the prototype imaging platform for digital mammography was performed.

Various imaging platforms were successfully developed and investigated to identify essential parameters for high-resolution digital x-ray breast imaging. The single module prototype exhibited physical characteristics that are favorable for digital mammography. Good agreement between model and experimental results were observed demonstrating the utility of such models for further system improvement. The large area 16 x 24-cm prototype demonstrated superior contrast-detail characteristics compared to a clinical FFDM system (100 μm pixel) at both 39 and 78-μm pixel sizes. Both experimental and theoretical results pointed towards the feasibility of contrast enhanced mammography at mean x-ray glandular dose levels substantially lower than mammography under the conditions investigated. Qualitative analysis of contrast enhanced digital mammography indicated favorable image quality.

CHAPTER 1

INTRODUCTION

Introduction

Breast cancer is the second leading cause of cancer death in women in the United States. According to the American Cancer Society, it is estimated that about 211,240 women in the United States will be found to have invasive breast cancer in 2005 and about 40,410 women will die from the disease ACS (ACS 2005). Given the serious nature of breast cancer, it becomes imperative to research and develop new methods for early breast cancer detection. The main focus of this work is to identify technical parameters that can improve the performance of digital x-ray imaging systems for breast cancer detection.

Screen-film Mammography

Mammography continues to prevail as the most widely used technique for breast cancer screening. For many years, screen-film (SF) technology has been the only image capture and display medium for mammography. This technology's dominating characteristic is its high-spatial resolution capability in the range of 16 to 20 line pairs/mm (lp/mm) while delivering good contrast. Further, the advances in screen and film technology and film processing techniques have contributed to significant improvements in mammographic image quality. It is a clinically well established technique for initial detection and follow-up. Screen-film is considered to be most effective in the detection and characterization of subtle microcalcifications, but its ability

to image low contrast features such as masses and architectural distortions depends on several factors that include proper exposure and film processing conditions (Nishikawa *et al* 1987, Yaffe *et al* 1988). The visualization of subtle soft tissue abnormalities located in a dense background can be particularly challenging in SF. Images of malignant masses are shown in Figure 1.1 and malignant microcalcifications are shown in Figure 1.2 as examples of radiographic features in mammography.

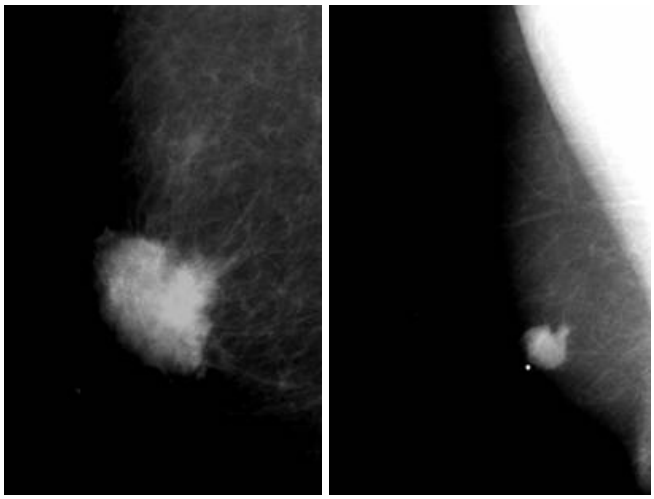

Figure 1.1. *Mammographic images of malignant masses (courtesy of Carl J. D'Orsi, M.D.).*

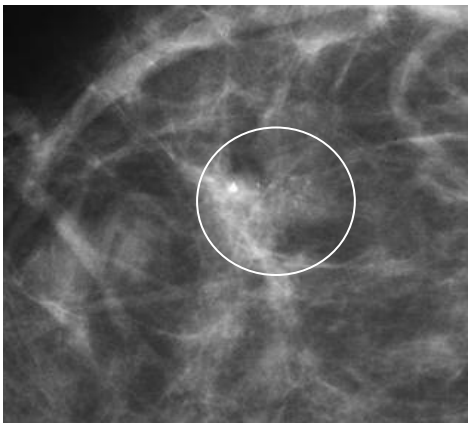

Figure 1.2. *Examples of a classic malignant microcalcification cluster (courtesy of Carl J. D'Orsi, M.D.).*

The main limitations of SF are associated with its limited dynamic range, contrast characteristics and granularity (Trauernicht and Van Metter 1988, Yaffe and Rowlands 1997, Karellas *et al* 2004). Nevertheless, SF technology is a low cost, low risk, and proven method for the early detection of non-palpable breast cancer, and has been shown to reduce breast cancer mortality through early detection (Thurfjell and Lindgren 1996). The sensitivity of SF mammography is about 80% (Rosenberg *et al* 1996) and may be significantly less in dense breast (Rosenberg *et al* 1998). The positive predictive value (PPV) of findings after biopsy range between 20 to 40% and the remainder is benign. From a logistical standpoint, image archival and communication of film is becoming more difficult, with a growing need to have screening facilities at one location and interpretation at another location. Moreover, the mailing of images to another radiologist for consultation is neither economical nor practical with film.

Digital Mammography

In pursuit of a viable alternative, in the mid 1980s, attempts were made to explore electronic imaging as a substitute for SF mammography and radiography (Herron *et al* 1984, Nishikawa *et al* 1987, Oestmann *et al* 1988, Shaber *et al* 1988, Yaffe *et al* 1988). Valuable contributions to x-ray imaging including suggestions for using digital sensors for mammography have also been made by several investigators (Herron *et al* 1990, Roehrig *et al* 1994). The term "digital mammography" refers to any technology that is used to detect, display, archive, and communicate mammographic images electronically. Digital mammography, in general, offers favorable properties compared to SF technology such as linear response to exposure, increased dynamic range, higher contrast, ability to adjust and process images, easy data transportability and storage (Vedantham *et al*

2000a). The early clinical experience with digital mammography was obtained from small-field imaging systems that were designed for stereotactic core biopsy, lesion localization, and spot views. These systems are used today and typically employ a scintillator as the primary image detector that was optically coupled to a charge-coupled device (CCD). They deliver good spatial resolution in the range of 6-12 lp/mm depending on the particular image sensor and also have excellent contrast characteristics and dynamic range (Karellas *et al* 1992, Roehrig *et al* 1994, Gambaccini *et al* 1996, Hejazi and Trauernicht 1997, Taibi *et al* 1997, Vedantham *et al* 2000c, Evans *et al* 2002). The best of these devices can deliver higher spatial resolution than some full-field mammography systems, however they cover only an image area of about 60 x 60 mm. Although in digital mammography solid-state electronic devices capture x-ray images, the images can either be viewed on an electronic display (cathode ray tube or flat panel type) or film, if the entire image needs to be viewed at high resolution. At the present time, the advent of sophisticated displays, digital mammography practices have more or less transformed to digital media from the point of image capture to image display. The potential impact of digital mammography in the early diagnosis and management of breast cancer was deemed very favorable (Shtern 1992) and several equipment manufacturers have endeavored in this field. Today, at least three types of clinical digital mammography systems are in clinical use in the United States. Unlike earlier small-field systems, today's digital mammography systems are large in area and are termed full-field digital mammography (FFDM) systems. The characteristics of these systems vary between manufacturers and a review of current trends has been addressed (Karellas *et al* 2004). Past clinical studies have indicated that current first generation digital

mammography is equivalent to SF (Lewin *et al* 2001, Skaane *et al* 2003). The initial clinical results from studies using an FFDM system with 100 μm pixel suggest that the PPV of digital mammography may be higher than for SF (Lewin *et al* 2001, Lewin *et al* 2002, Skaane *et al* 2003). The results of a recent comprehensive clinical study involving a variety of digital mammography systems indicated that the overall diagnostic accuracy of digital and SF mammography as a means of screening for breast cancer was similar, although digital mammography was more accurate in, (i) women under the age of 50, (ii) women with radiographically dense breasts, and (iii) premenopausal or perimenopausal women (Pisano *et al* 2005).

Motivation

Despite the advantages of FFDM over SFM, the performance of digital mammography compared to film for specific types of features, particularly for very subtle microcalcifications, remains to be established. The large area contrast properties of FFDM suggest that its ability to detect soft tissue masses and architectural distortions is likely to exceed that of film but it is not quite as clear for the detection of microcalcifications, a mammographic feature that is frequently associated with the presence of malignancy. The larger pixel size and the resulting lower spatial resolution than that of SF warrants particular attention in the optimization of FFDM systems with respect to detectability of subtle microcalcifications.

At the present time there no consensus on a preferred digital technology or performance specifications, and a user has to carefully select a detector technology in order to achieve desired performance metrics (Noel and Thibault 2004). For example,

clinical amorphous silicon (a-Si:H)-based FFDM systems have a pixel pitch (center-to-center distance between two adjacent pixels) of 100 μm (Vedantham *et al* 2000a, Suryanarayanan *et al* 2004a) and amorphous selenium (a-Se)-based clinical FFDM systems have a pixel pitch of 70 μm (Saunders *et al* 2005). Smaller pixel pitch in digital mammography is offered by a slot-scan system based on charge coupled device (CCD) technology (Tesic *et al* 1999) and a photon counting detector system in a slot scan geometry (Aslund *et al* 2004, Hemdal *et al* 2005). In addition, smaller sampling distances are offered by photostimulable storage phosphor technology (Siebert *et al* 2004). When subtle calcifications are visualized, their edges may not appear to be as sharp when compared to similar observations with spot film views, and this may possibly be related to the relatively large pixel size of conventional digital imaging sensors. Various studies point to the possible need for higher spatial resolution in digital mammography (Cowen *et al* 1997, Rong *et al* 2002, Yamada *et al* 2003, Ruschin *et al* 2005). In a recent study, Yamada and colleagues (Yamada *et al* 2003) concluded that high spatial resolution is required in digital mammography to successfully differentiate between microcalcifications. In another recent study, Ruschin *et al* (2005) found improved performance in terms of microcalcification shape determination at pixel sizes much below 100 μm. Current large area flat-panel digital mammography imagers have pixel sizes in the range of 70-100 μm, but it is desirable to explore the high resolution aspects of digital mammography beyond what is commercially available for full-field non-scanning systems. Unfortunately, this cannot be done presently with a-Si:H and amorphous selenium (a-Se) detectors because pixel sizes at about or below 50 μm are currently not technically and economically feasible. Further, at small pixel sizes the

relative influence of electronic noise could be high thereby reducing signal-to-noise (SNR) ratio which is a concern with all types of detectors.

Apart from spatial resolution, the other key factor that influences visualization of subtle lesions is contrast. Although, current digital mammography systems provide improved contrast compared to SF technology, it is still challenging to visualize extremely subtle mass-type lesions. As conventional mammography cannot image angiogenesis it becomes all the more important to investigate contrast enhanced digital mammography for visualization of early malignant angiogensis. Clinical studies using Gd-DTPA enhanced digital subtraction imaging of the breast with magnetic resonance imaging (MRI) have demonstrated the potential ability to provide accurate diagnosis, extent of disease and multi-centricity (Flanagan *et al* 1995). Further, independent clinical trials conducted in Canada (Warner *et al* 2001) and The Netherlands (Stoutjesdijk *et al* 2001) for women at high-risk of hereditary breast cancer indicate that contrast-enhanced MRI may be a superior to screen-film mammography and that a large-scale clinical study is needed. While MRI may have a significant role, a review of the state-of-the-art in MR imaging of the breast (Orel and Schnall 2001) addresses several of the issues and concerns, such as cost, the ability to detect small lesions. MRI of the breast has demonstrated increased sensitivity but with moderate to good specificity (Schnall 2001, Schnall 2003, Kriege *et al* 2004).

A recent pilot clinical study (Shumak *et al* 2001), using the 100 μm pixel size digital mammography detector to evaluate the potential of digital subtraction angiography (DSA) of the breast, indicated that non-ionic iodinated contrast media injected digital subtraction images can provide qualitatively similar information to studies performed

with Gd-DTPA contrast-enhanced MRI. These results motivate further exploration of this technique as a potentially faster, high-resolution and less expensive alternative to MRI. While early investigations into the applicability of DSA (Watt *et al* 1985, 1986) and dual-energy imaging (Johns and Yaffe 1985) for diagnosis of breast cancer showed promising results, these investigations were limited by the available technology at that time. More recently, clinical studies using contrast enhanced digital subtraction mammography technique performed with a 100 mm pixel detector showed promising results (Lewin *et al* 2001, Lewin *et al* 2003). In a recent study, Lawaczeck and colleagues (Lawaczeck *et al* 2003) investigated a range of contrast media for energy subtracted digital mammography. However, they restricted themselves to using a conventional mammography tube which did not permit the investigation of higher k-edge contrast agents such as Iodine. The impact of x-ray filters on exposure levels with iodine as the contrast media has been explored (Kanno *et al* 2003), and the results demonstrate the potential for exposure reduction with certain filter materials that have atomic numbers close to iodine. In another investigation, the usefulness of contrast enhanced digital mammography was studied using non-ionic solution of iodine as the contrast agent (Skarpathiotakis *et al* 2002, Jong *et al* 2003). The investigators concluded that the results were encouraging and warranted further research.

The developments in digital mammography provide new techniques for imaging angiogenesis in the breast and other processes hitherto unattainable with SF techniques (Jong *et al* 2003). Angiogenesis is a precursor to certain types of breast cancers (Tuncbilek *et al* 2003, Turhal *et al* 2004). The focus of this work is to explore the high-

resolution digital mammography and contrast enhanced digital mammography based on imager physical characteristics.

Approach

A combination of theoretical and experimental methods is used throughout this work for the design, development, and characterization of an imaging platform for mammography. Since the focus of the work described here is to explore and understand the characteristics of advanced imaging methods for high-resolution and contrast enhanced digital mammography, the metrics used are selected to reflect the signal and noise characteristics of the imaging chain. The following universally accepted physical metrics such as modulation transfer function (MTF), noise power spectra (NPS), and detective quantum efficiency (DQE) were used as the basis to assess imager performance. The theoretical methods used in this work are based on a linear systems framework that can be used to quantitatively derive the signal and noise propagation properties of an imaging system at each stage in the imaging chain. An important aspect of this technique is that it facilitates rapid prototyping of imaging systems and can be used to understand the impact of various key system design parameters on metrics such as the DQE. Physical parameters do not always give the complete picture and it therefore becomes necessary to understand the perceptual nature of an imaging system. For this purpose, psychophysical metrics such as detection and contrast-detail (CD) characteristics were used to study the performance of high-resolution digital mammography.

Thesis Organization

The organization of the topics described in this work closely resembles the actual progression of research projects that form the basis of this thesis. Given the nature of the work presented here, it only seems logical to address each research topic in detail, as a separate entity while relating its impact on performance on an overall basis.

Chapter 2 provides a comprehensive survey of literature in the area of digital mammography. It describes the current state-of-the–art in digital mammography and the contributions of these technologies for breast imaging.

Chapter 3 introduces the basic design of the imaging platform developed as part of this study for high and variable resolution digital mammography. A description of a single module imager is provided which served as the basic platform for various studies in this research. Further, a description of a large area multi-modular imaging platform is also provided which evolved from the single module platform. In addition, the architecture of a large area multi-frame imager for contrast enhanced mammography is described.

Chapter 4 introduces the application of theoretical formulations to study imaging performance in terms of MTF and DQE for digital mammography. In this chapter the parameters that greatly influence system performance are described. The models are applied for a clinical FFDM and the prototype single module imaging platform.

Chapter 5 describes the empirical physical characteristics of the prototype single module imager and a clinical FFDM system under a various x-ray spectral conditions.

Chapter 6 compares the perceptual characteristics of the prototype large area high-resolution digital mammography platform to a clinical FFDM system specifically targeted at the detection of small objects.

Chapter 7 introduces the application of theoretical formulations based on the parallel cascaded approach for contrast enhanced digital mammography. As in Chapter 4, this chapter the parameters that influence system performance.

Chapter 8 describes the empirical characterization of a prototype for contrast enhanced digital mammography and investigates the feasibility of this application.

Chapter 9 provides an overall assessment of the technical feasibility for large area, high resolution digital mammography and contrast enhanced digital mammography. In addition, futuristic trends in x-ray imaging of the breast are highlighted.

Scope of Work

This thesis presumes that the reader is familiar with the basic physics and certain technical and clinical aspects of mammography and x-ray imaging. While the intention of this thesis is to provide information on the advancement of technology for digital mammography, it does not cover the fundamentals in great detail. However, an effort has been made to include discussions on certain physical aspects, and relevant terms and symbols have been explained.

CHAPTER 2

PROGRESS IN DIGITAL MAMMOGRAPHY

Introduction

Digital mammography does not refer to a specific technology but rather includes a broad range of detector technologies. These technologies differ in design and properties to a large extent. There may be dedicated technologies specific for a mammography system or may be a cassette-type technology that can be easily migrated across various mammography units. The dedicated digital detectors can be classified into stationary or scanning detectors, while the stationary detectors may be further classified as indirect scintillator-based detectors or direct x-ray conversion detectors. A schematic representation of the various technologies is shown in Figure 2.1.

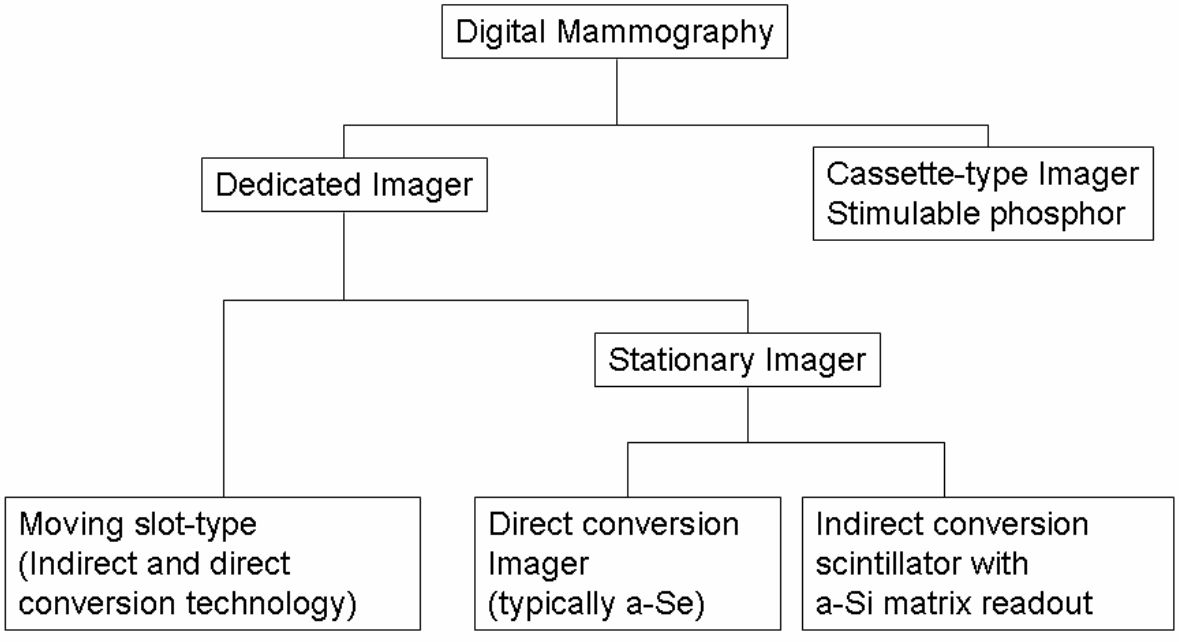

Figure 2.1. *Current technological approaches for digital mammography (with permission from RSNA, Karellas et al. 2004).*

Dedicated Imaging Technologies

These types of technologies have been specifically developed to operate as a separate entity and cannot be used as an added module to a SF unit. The two main approaches in this type of technology are indirect conversion and direct conversion (Drewery *et al* 1991). Indirect x-ray conversion technologies typically use a scintillator to convert x-ray to optical photons which are then detected by a digital detector. The most common scintillator that is used for digital mammography is thallium doped cesium iodide (CsI:Tl) due to its attractive optical properties. In direct conversion, x-rays are directly converted to an electric signal by the detector with no intermediate optical conversion stage.

Indirect X-ray Conversion Detectors

At the present time, the most popular indirect x-ray conversion approach for digital mammography is using a combination of a flat-panel a-Si:H with thin film transistors (TFT) (Antonuk *et al* 1997, Vedantham *et al* 2000a, Albagli *et al* 2003, Jee *et al* 2003, Suryanarayanan *et al* 2004a) and a suitable scintillator such as CsI:Tl. Other indirect approaches that use CCDs (Karellas *et al* 1992, Williams *et al* 1999b, Vedantham *et al* 2000c) or complementary metal oxide semiconductor (CMOS)-type pixel matrix photodetectors (Smith *et al* 1999, Graeve and Weckler 2001) are viable alternatives and are of potential interest. The scintillator, CsI:Tl is vapor-deposited directly onto a-Si:H in a pseudo-fiberoptic structure that suppresses lateral light diffusion and reduces degradation of spatial resolution. The x-ray photons incident on the scintillator are converted to visible light photons and are subsequently detected by the a-Si:H sensor and readout through a TFT array. This approach has been successfully

implemented for digital mammography at a pixel size of 100 μm (Vedantham *et al* 2000a, Vedantham *et al* 2000b, Suryanarayanan *et al* 2004a). Technological and economic barriers limit the production of such large area detectors at smaller pixel sizes below 50 μm. In a recent study, the contrast detail analysis of an a-Si:H-based FFDM and a SF system indicated superior CD performance by the digital technology (Suryanarayanan *et al* 2002). A representation of this type of technology is shown in Figure 2.2.

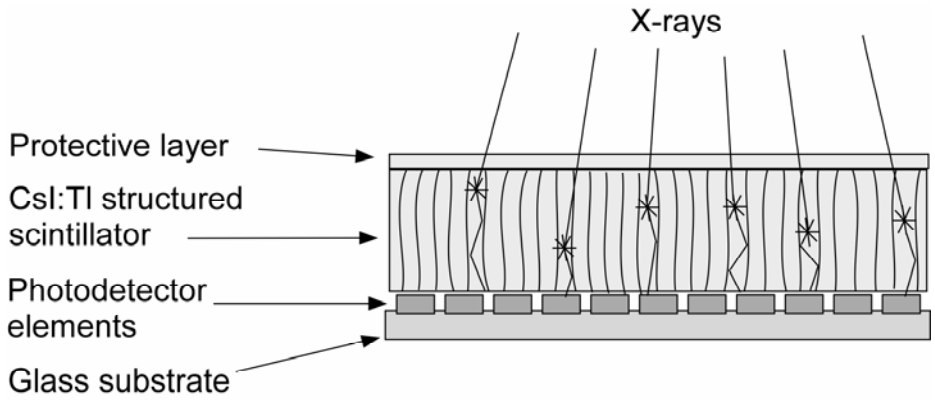

Figure 2.2. *X-ray detection using an a-Si:H-based detector (with permission from RSNA, Karellas et al. 2004).*

Earlier indirect x-ray conversion digital imagers for mammography used CCD modules onto which a scintillator was coupled using fiberoptic tapers. Despite the high spatial resolution, this approach has been discontinued due to the bulkiness of the imager and the loss of optical signal due to demagnification between the scintillator and CCDs. The demagnification effect between the phosphor and CCD not only reduces signal level but also degrades spatial resolution (Karellas *et al* 1992, Hejazi and Trauernicht 1997, Yaffe and Rowlands 1997). The low signal levels demanded very low noise levels during system design in order to maintain a reasonable SNR. This required

thermoelectric cooling of the system adding to further design complications. Indirect x-ray conversion approach of using tiled CCDs that are optically coupled to a scintillator by a non-tapering (straight) fiberoptic is a viable option and is currently used in one of the commercially available slot-scanning mammography systems (Tesic *et al* 1999).

Slot-Scan Mammography

In slot-scan mammography, a narrow fan beam scans the breast in a direction parallel to the chest wall. The detector used in this approach is typically a series of fiberoptic-coupled tiled CCDs coupled to scintillator (Holdsworth *et al* 1990, Maidment *et al* 1993, Jing *et al* 1998, Tesic *et al* 1999). Good x-ray scatter rejection is attained due to the inherent nature of the slot, and this obviates the need for an antiscatter grid thereby making it possible to use lower radiation dose to the patient, while offering the potential of higher contrast. However, such scanning systems require considerable time to scan (about 4 sec) which creates problems associated with both patient and mechanical movement. However, it appears that motion artifacts due to the prolonged exposure time do not present a major issue (Boyle *et al* 1999). Tungsten (W) is the preferred target slot scanning system because of the high x-ray tube heat load requirements of the slot-scan approach. Presently, one clinical system uses a single slot of width about 1 cm and length of about 22 cm with variable pixel sizes of 27 or 54 μm.

Direct X-ray Conversion Detectors

Currently, the only direct x-ray conversion material used for clinical digital mammography is amorphous selenium (a-Se). Selenium was used in the 1970s and 80s for xeroradiography and xeromammography. However, xeromammography was later

abandoned due to technological issues and SF became the gold standard. In recent years, there has been substantial progress in a-Se technology, specifically in the charge readout methods (Rowlands *et al* 1991, Neitzel *et al* 1994, Zhao and Rowlands 1997, Zhao *et al* 2001, Zhao *et al* 2003). Direct conversion does not make use of an intermediate scintillator and x-rays are directly converted to electrons after interaction in the photoconductive layer of the detector. The concept of direct x-ray conversion is illustrated in Figure 2.3. Other direct x-ray detection materials such as cadmium zinc telluride (Mainprize *et al* 2002) and mercuric iodide (Jee *et al* 2001, El-Mohri *et al* 2003) are being explored.

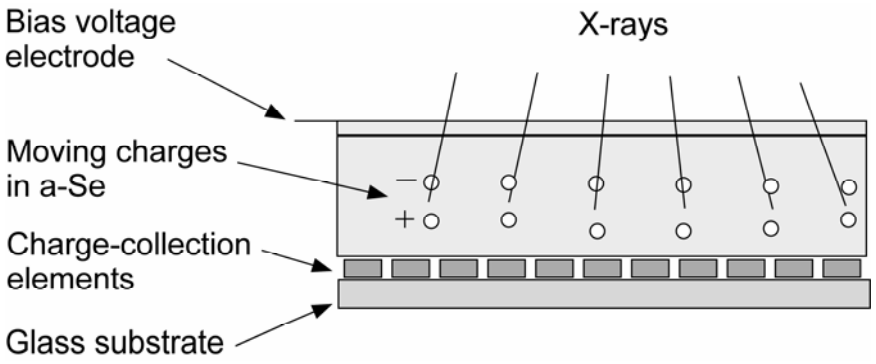

Figure 2.3. *X-ray conversion using an a-Se-based detector (with permission from RSNA, Karellas et al. 2004).*

Active matrix array is now the standard charge readout approach in a-Se and is used in commercially available digital mammography systems. A pixel size of 70 μm is easily attainable that results in good spatial resolution, and detective quantum efficiency (Saunders *et al* 2005). A high voltage bias (mushroom structure) can be applied in order to collect the generated charges which are then readout using thin-film transistors (TFT)

(Waechter *et al* 1996). The removal of the intermediate scintillator layer in a-Se results in the improvement of spatial resolution (Saunders *et al* 2005).

Photostimulable Phosphor Plates

Photostimulable phosphor radiography commonly known as computed radiography (CR) has been used successfully for several x-ray imaging procedures since the early 80s (Sonoda *et al* 1983). A cassette comprising an image-phosphor plate (IP) typically consisting of BaFBr:Eu^{2+} crystals on a suitable substrate is used as the primary detector of x-rays.

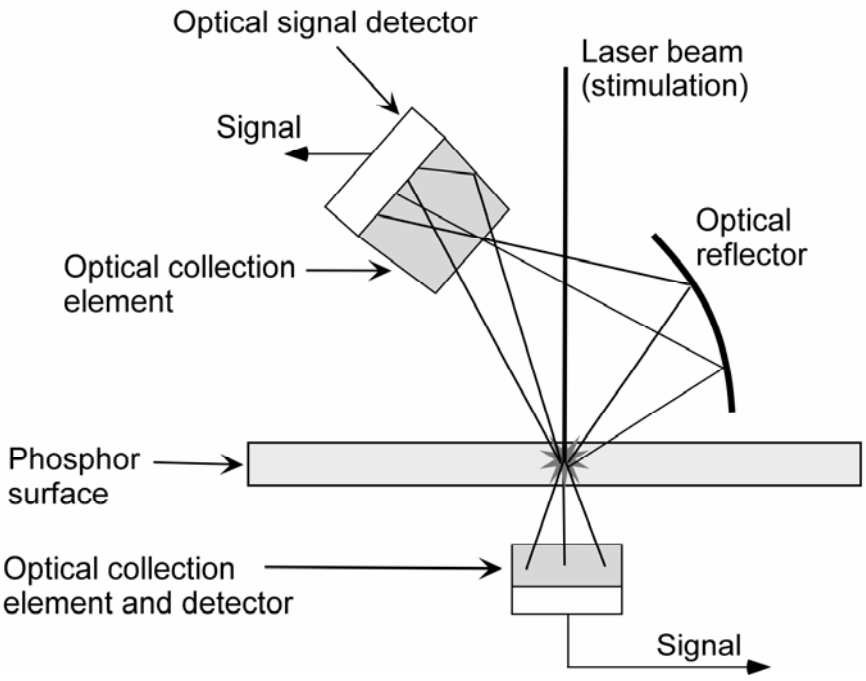

***Figure 2.4**. Signal read-out from a CR plate (with permission from RSNA, Karellas et al. 2004).*

As a result of x-ray interaction with the phosphor, Br-vacancies act as traps (f-centers) for the electrons that migrate to the conduction band of the crystal. This forms a latent image

which remains stable for several hours due to the trapping effect of the electrons. The number of electrons that are trapped is proportional to the x-ray exposure. The stored signal is then read out by stimulating the IP with an intense scanning laser beam that scans the entire IP in a raster fashion (Figure 2.4) (Arakawa *et al* 1999, 2000). Laser stimulation causes the electrons return to the ground state by emitting light near the ultraviolet-blue region of the electromagnetic spectrum. The emitted light is then detected using a photomultiplier tube (PMT), or other suitable photodetectors and reconstructed to form an image. In current systems, the complete CR readout and image formation is achieved in a time frame that is about 45 sec shorter than film processing but emerging technology based on line scans enable processing in the order of seven seconds per plate (Schaetzing *et al* 2002). The characterization of CR equipment has been the subject of several studies (Sanada *et al* 1991, Dobbins *et al* 1995, Arakawa *et al* 1999, Bradford *et al* 1999, Flynn and Samei 1999, Arakawa *et al* 2000, Fetterly and Hangiandreou 2001, Fetterly and Schueler 2003, Seibert *et al* 2004). The readout of CR plates presents significant challenges due to light scattering within the phosphor layer that could degrade spatial resolution and the frequency dependent DQE, $DQE(f)$ of the system. New technological developments have enabled the efficient readout of IPs with a sampling of 50 to 100 microns with high light collection efficiency by reading the plate from both sides (Arakawa *et al* 1999, 2000, Fetterly and Schueler 2003, Seibert *et al* 2004). This technique has been shown to improve the signal collection efficiency, spatial resolution and detective quantum efficiency compared to the standard techniques of single side reading (Arakawa *et al* 2000, Fetterly and Schueler 2003, Seibert *et al* 2004). A unique advantage of CR technology is that it can be used with existing mammographic

equipment and does not require a dedicated digital mammography system. Further, CR technology has many of the advantages of other digital detectors such as dynamic range, contrast enhancement, image processing, storage, and transmission.

Emerging Technologies

The advances in digital detectors have spurred a growth in novel system designs and applications for mammography such as photon counting (Aslund *et al* 2004), x-ray phase contrast imaging (Arfelli *et al* 1998, Pisano *et al* 2000, Wu and Liu 2003), tomosynthesis (Niklason *et al* 1997, Suryanarayanan *et al* 2000, Suryanarayanan *et al* 2001, Wu *et al* 2003, Wu *et al* 2004), and breast computed tomography (Raptopoulos *et al* 1996, Boone *et al* 2001, Chen and Ning 2002).

CHAPTER 3

DESCRIPTION OF IMAGING PLATFORMS

Introduction

The imaging platform that was chosen was based on CCD technology. The motivating factors for choosing this platform are numerous: (i) CCD technology has the ability to offer very small pixel sizes, (ii) multiple pixel sizes on the same platform can be achieved via “binning, (iii) the noise properties of CCDs are favorable for studies at low x-ray exposure levels, (iv) scintillator materials can be easily swapped, and (v) multiple modules can be tiled to form a larger imager.

Single Module Imager

In collaboration with Fairchild Imaging Inc. (Milpitas, CA), a solid-state monolithic prototype imager of size 8 x 8-cm with a fundamental pixel size of 39-μm

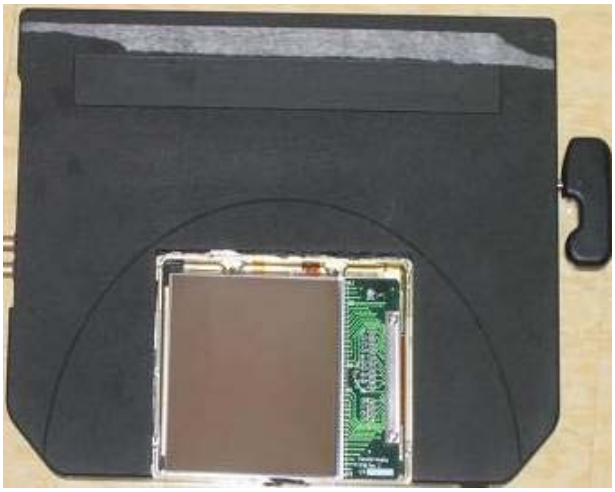

Figure 3.1. *Single module 8 x 8 cm imager without the cover plate (manufactured by Fairchild Imaging Inc., Milpitas, CA) .*

and unity fill factor was developed based on CCD technology (Figure 3.1). Each monolithic CCD module is 3-side buttable. The monolithic CCD module consists of 2048 x 2048 pixel elements (39-μm pixel) in the fundamental (un-binned pixel) operating mode. The CCD design incorporates a full-frame architecture that is operated using 3 phase clocking. An on-chip amplifier is provided at each end of the horizontal register. Each of the two on-chip amplifiers consists of a two-stage source follower (Figure 3.2).

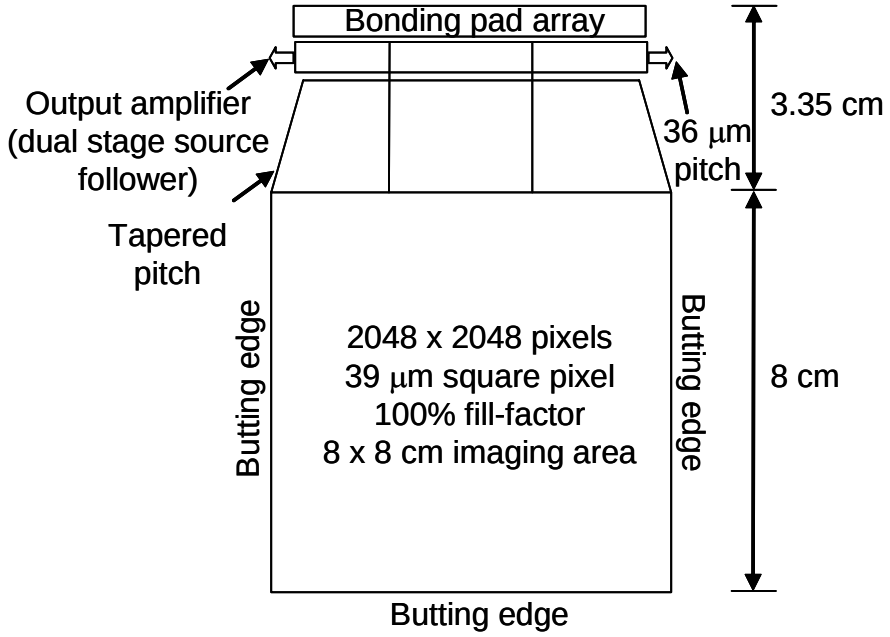

Figure 3.2. *Basic architecture of the single module imager.*

The CCD is directly coupled to a non-tapering fiber optic faceplate plate (Schott North America Inc., Southbridge, MA) with 6 μm fibers and 9.5 degree bias cut with a numerical aperture of 1.0. A thallium-doped cesium-iodide (CsI:Tl) scintillator with a thickness of 150-μm deposited on an amorphous carbon substrate (Hamamatsu Corporation, Bridgewater, NJ) and coupled to the fiberoptic faceplate. A foam-type material was placed over the scintillator substrate and the complete assembly was

pressure bonded with a detector cover plate. The design is such that the scintillator can be easily changed. The detector and electronics were packaged as a cassette and operated without any liquid circulation for cooling. The interaction of x-rays in the CsI:Tl scintillator generates optical photons that are channeled through its columnar structure and are detected by the photosensitive elements of the CCD. The signal is read out by low-noise electronic circuitry and digitized to 12-bit digital values. The prototype imager was mounted on a modified mammography system (GE Medical Systems, Milwaukee, WI) such that the source-to-detector distance was 66 cm (Figure 3.3). The mammography system uses a selectable target, either molybdenum (Mo) or rhodium (Rh) with selectable filtration of Mo or Rh.

Figure 3.3*. Integration of the prototype imager with a mammography system.*

Multi-Module Imager

The multi-module 16 x14 cm imager (Figure 3.4) was formed by tiling the single module CCDs in a 2 x 3 array fashion. The basic CCD architecture was the same as that of the single module imager. The detector and electronics are housed in an enclosure slightly larger than the 16 x 24 cm array dimensions, and operated without any liquid circulation for cooling. Fans are mounted to the enclosure to remove heat from the electronics. A key feature of this large area device was the availability of 39 and 78-μm pixel modes using pixel binning. Another, interesting feature of this device was the availability of two gain settings, 5 e-/DU and 20 e-/DU, which provided flexibility to control signal saturation under certain x-ray exposure conditions. The signal is read out by low-noise electronic circuitry and digitized to 16-bit digital values.

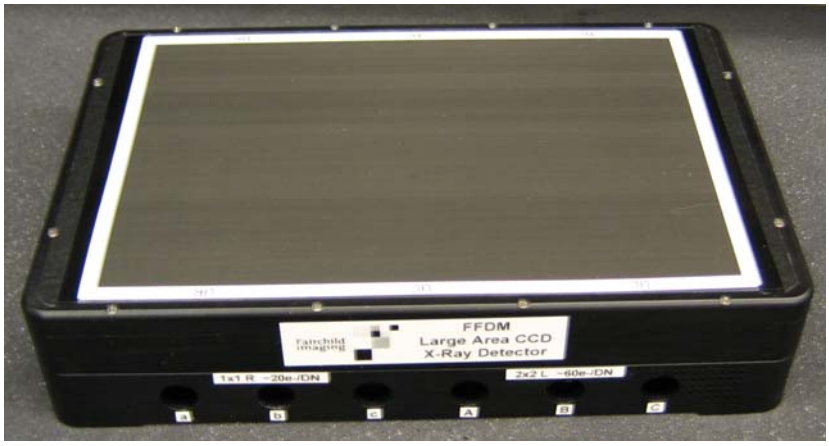

Figure 3.4. *Large area 16 x 24 cm prototype imager (manufactured by Fairchild Imaging Inc., Milpitas, CA).*

Imager for Contrast Enhanced Mammography

The imaging platform originally developed for angiography (Vedantham *et al* 2004b) was modified for higher resolution applications such as contrast enhanced mammography (Figure 3.5). The imaging platform consists of a 2 x 2 array of CCDs. The individual CCDs are three-side buttable and are 8 x 8 cm in dimension. The

fundamental pixel pitch of each CCD is 39 μm thereby forming an array of 2048 x 2048 pixels per imaging module. However, the system was set to operate in a 2 x 2 binning or 78 μm pixel pitch mode. Each CCD module has 8 readout ports and was designed to run at 6.865 frames/sec. The frame rate was achieved by an interline architecture and by using all the ports for readout. The general concept for this sensor was proposed to Fairchild Imaging Inc. by our research team.

The main advantage of the interline architecture is that it permits data readout while the present frame is being integrated due to the optical opacity of the interline channel. However, this causes a loss of geometrical fill factor. The width of the interline channel is 19 μm and this corresponds to a fill

Figure 3.5. *Large area 16 x 16 cm prototype imager for contrast enhanced mammography (manufactured by Fairchild Imaging Inc., Milpitas, CA).*

factor of 0.513. Once the charge collection and integration process is complete, the charges are transferred to the interline channel. Pixel binning is achieved by transferring 2 rows of charges from the interline channel to the vertical summing well (vertical

binning) and by 2 columns of charges in the vertical summing well to the horizontal summing well (horizontal binning), thereby resulting in a 2 x 2 binned configuration. No liquid circulation or thermoelectric (TEC) cooling is used, however some cooling is achieved via built-in air-circulation with fans. The platform is designed to be coupled to a scintillator with a 1 inch-thick straight fiber optic plate (Schott North America Inc., Southbridge, MA) facilitating easy scintillator replacement. A schematic of the architecture is shown in Figure 3.6.

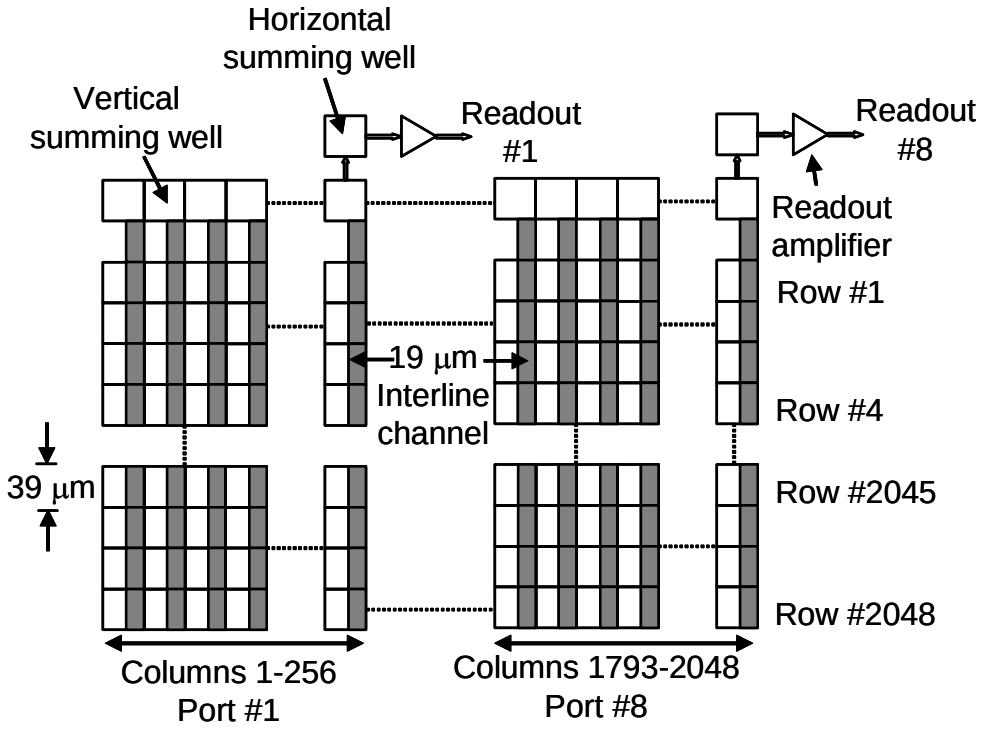

Figure 3.6*. Architecture of an 8 x 8 cm CCD module for contrast mammography.*

Conclusion

Various prototype platforms were developed based on CCD technology. The platforms described in this section facilitate the study of the impact of various physical

parameters under controlled conditions. The described platforms were used as the basis for theoretical and experimental studies in this research.

CHAPTER 4

THEORETICAL SYSTEM ANALYSIS OF DIGITAL MAMMOGRAPHY

Introduction

The performance characteristics of the prototype high-resolution imager and a clinical FFDM system were studied using a mathematical framework based on cascaded linear systems theory. A computer simulation model was implemented using the Interactive Data Language software (IDL 5.6, Research Systems Inc., Boulder, CO). The objective was to understand the influence of various system parameters on the $DQE(f)$ characteristics, specifically for the prototype. In addition, the model was validated for the clinical FFDM system. Comparisons of both the systems were performed under comparable clinically relevant x-ray exposure conditions. The details of empirical $DQE(f)$ measurements for both systems are discussed in chapter 5.

The reason for choosing $DQE(f)$ as a metric was because it represents the fidelity of an x-ray imaging system and takes into account both the signal and noise transfer characteristics. Further, it is an objective metric that is universally accepted. Detailed descriptions of the cascaded linear systems analysis of x-ray imaging systems that were used in this study have been provided by various investigators (Rabbani *et al* 1987, Cunningham *et al* 1994, Siewerdsen *et al* 1997, 1998a, 1998b, Williams *et al* 1999b, Antonuk *et al* 2000, Zhao *et al* 2003). This linear systems framework can be used to quantitatively derive the signal and noise propagation properties of an imaging system at each stage in the imaging chain. An important aspect of this approach is that it facilitates rapid prototyping of imaging systems and can be used to understand the impact

of various system parameters on key metrics such as the $DQE(f)$. Various investigators (Siewerdsen *et al* 1997, 1998a, 1998b, Williams *et al* 1999b, Evans *et al* 2002, Ganguly *et al* 2003, Jee *et al* 2003, Zhao *et al* 2003, Vedantham *et al* 2004a) have applied variants of the cascaded linear systems framework to predict the performance of x-ray imaging modalities. In the past, similar approaches have been used to study CCD-based digital mammography systems (Williams *et al* 1999b, Evans *et al* 2002).

In this study, system parameters such as pixel size, scintillator thickness, x-ray spectra, exposure, scintillator packing density, dark current, charge, integration time, and pixel fill-factor were varied in order to study their effects on the $DQE(f)$ characteristics of the prototype high-resolution imager. For the existing clinical FFDM system, the model was adapted and validated against experimental $DQE(f)$ data. Modeling was performed based on known parameters of the imager and by making reasonable assumptions.

This chapter is organized as follows: (i) the theoretical analysis of the high resolution imager is discussed, (ii) a brief description of the theoretical analysis of the clinical FFDM system is provided, (iii) simulation results for the high-resolution imager is presented, (iv) the application of simulation for the clinical FFDM system is presented, and (v) comparison of the prototype to the clinical FFDM system are made for certain conditions.

Methods

Prototype High-Resolution System Analysis

The complete imaging chain was modeled as a series of cascading stages specific to the imaging configuration used in this study. The approach followed similar modeling that has been performed in the past for a-Si:H indirect imagers by Siewerdsen *et al* (1997, 1998a, 1998b) and Jee *et al* (2003). At each stage, the signal and noise terms were derived for the system described in this study based, on the physical processes occurring at that stage.

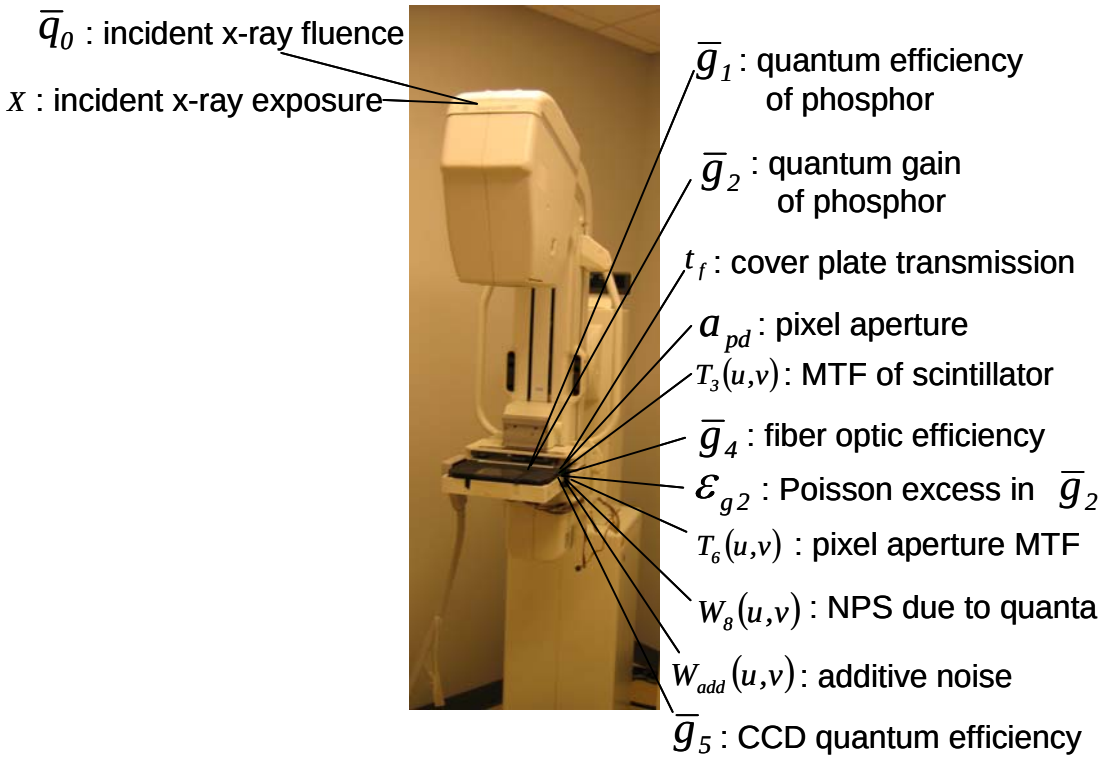

Figure 4.1. *Mathematical representation of the high-resolution mammography system.*

The physical stages that were modeled were, x-ray quanta incident on the imager (stage 0), attenuation of x-ray in the scintillator (stage 1), optical quanta generation and

emission (stage 2), scintillator optical blurring (stage 3), fiber-optic coupling (stage 4), absorption of optical quanta in the imager (stage 5), pixel presampling MTF (stage 6), noise power spectra aliasing (stage 7), and additive noise (stage 8). A representation of the various stages is shown in Figure 4.1. The fundamental model parameters used for this part of the study are listed in Table 4.1.

Table 4.1. Estimates of input parameters used for the high-resolution imager

Photons/keV, $W_{CsI:Tl}$	55
Scintillator surface density (mg/cm^2), ρ_s	48
Fiber optic coupling efficiency, g_4	0.41
Quantum efficiency, g_5	0.34
Gain (e-/DU)	123
Dark current (pA/cm^2)	12
Read noise (e- rms)	10

A description of the various stages, assumptions, and approaches to either estimate or derive the model parameters is discussed below. Following the various cascading stages for the imaging geometry , the signal at the output of the final stage (stage 8) was computed according to the description provided by Rabbani *et al* (1987) and Siewerdsen *et al* (1997,1998a,1998b) as

$$\phi(u,v) = t_f \bar{q}_0 \bar{g}_1 \bar{g}_2 \bar{g}_4 \bar{g}_5 T_3(u,v) T_6(u,v) f_f a_x a_y \qquad [1]$$

where t_f is the x-ray transmission loss through the detector cover plate, $\bar{q}_0$ is the mean number of x-ray quanta per unit exposure, $\bar{g}_i$ (where i=1,2,4,5) is the gain of each imaging stage, $T_3(u,v)$ is the optical blur of the scintillator, $T_6(u,v)$ is the pixel presampling MTF, f_f is the pixel fill-factor, and a_x and a_y are the 'x' and 'y' dimensions of

the pixel. Following the framework of Rabbani *et al* (1987) and the description provided by Siewerdsen *et al* (1997,1998a,1998b), the NPS in the final stage (stage 8), with the inclusion of aliasing was obtained in a form that is essentially the same as the one derived by Siewerdsen *et al* (1997, 1998a,1998b) as

$$W_8(u,v) = t_f \bar{q}_0 \bar{g}_1 \bar{g}_2 \bar{g}_4 \bar{g}_5 f_f^2 a_x^2 a_y^2 \left[1 + \bar{g}_4 \bar{g}_5 \left(\bar{g}_2 + \varepsilon_{g2}\right) T_3^2(u,v)\right] T_6^2(u,v) ** III_7(u,v) + W_{add8}(u,v) \quad [2]$$

where $III_7(u,v)$ represents 2D aliasing of the NPS. Additive noise, W_{add} was added to Eq. 2 after aliasing to account for noise sources other than x-ray photon noise. In Eq. 2, ε_{g2} represents the Poisson excess of that gain stage. The $DQE(f)$ was computed as the ratio of the square of the signal to the total NPS inclusive of additive noise at a given exposure level.

$$DQE(u,v) = \phi^2(u,v) \Big/ W_8(u,v)\bar{q}_0 \quad [3]$$

The primary difference in the geometry used in this paper versus the description provided in APPENDIX A of Siewerdsen *et al* (1997) is the presence of an extra fiber optic coupling stage (stage 4) with associated gain, g_4 and accounting for transmission t_f through the detector cover plate.

Imaging Stages

Incident X-ray Quanta: In this stage, the mean number of x-ray quanta per exposure, $q_o \Big/ X$ that is incident on the detector cover plate after traversing through 45 mm of polymethyl-methacrylate (PMMA) was computed based on the definition of Roentgen (Johns and Cunningham 1983). Spectral simulations for this computation were

performed using the software catalogue (SRS-78) provided by the Diagnostic Radiology and Magnetic Resonance Special Interest Group of the Institute of Physics and Engineering in Medicine (Cranley *et al* 1997). The tables provided in this catalogue rely on the x-ray tube spectral emission modeling method of Birch and Marshall (Birch and Marshall 1979). The incident spectra were computed by assuming a 0.8 mm Be window, 30 μm Mo filter (Tkaczyk *et al* 2001), 25 μm Rh filter (Tkaczyk *et al* 2001) and an appropriate thickness of PMMA as additional filtration medium. The source-to-detector distance was 66 cm and the emission angle was estimated to be about 15^{o} at the center of the imager. The actual number of quanta that interact with the scintillator was then computed by accounting for transmission, t_f through the detector cover plate and scintillator substrate (Tkaczyk *et al* 2001, Vedantham *et al* 2004a). A transmission of 0.90 was used for the scintillator substrate based on the manufacturer provided data sheet (Hamamatsu 2000). The cover plate transmission with 45 mm poly-methyl methacrylate (PMMA) filtration was measured to be 0.81 for 26 kVp, Mo/Mo (target/filter), 0.84 for 28 kVp, Mo/Rh, and 0.85 for 30 kVp, Rh/Rh.

Quantum Efficiency: The energy dependent quantum efficiency (QE) was computed as

$$g_1(E) = 1 - exp[-(\mu(E)X)] \qquad [4]$$

where $\mu(E)$ is the energy-dependent linear attenuation coefficient of CsI:Tl and X is the thickness. The mass attenuation coefficients of CsI:Tl were obtained from the Physical Reference Data of the National Institute of Standards and Technology (Hubbell and Seltzer 1997). The surface density, ρ_s (mg/cm^2) of the scintillator sample was estimated from the manufacturer (Hamamatsu Corp., Bridgewater, NJ) provided data for other similar samples. These were used to compute $\mu(E)$, and finally, the energy-dependent

QE, which was then weighted by the incident x-ray spectrum normalized to unit area and represented as $q_{rel}(E)$ to provide an average QE, $\bar{g}_1$ where

$$\bar{g}_1 = \int g_1(E) q_{rel}(E)\, dE \qquad [5]$$

Quantum Gain: The generation and emission of optical quanta from the scintillator are described with an average quantum gain, $\bar{g}_2$. As described by Siewerdsen *et al* (1997, 1998a, 1998b), this stage was modeled as the product of two sub-stages that accounted for optical gain and optical escape efficiency. In the case of mammography where the energies are typically below the k-edge of the CsI:Tl scintillator, the number of optical quanta emitted per absorbed x-ray photon at a distance z towards the imaging array can be expressed as (Siewerdesen 1997, Rowlands and Taylor 1983)

$$g_2(E,z) = W_{CsI:Tl} E \eta_{esc}(z) \qquad [6]$$

where $W_{CsI:Tl}$ is the number of optical photons generated per keV, E is the energy of the incident x-ray photon, and $\eta_{esc}(z)$ is the probability of escape of an optical photon generated at a distance z from the output side of the scintillator and traversing towards the imaging array . The depth dependant optical escape efficiency was obtained by fitting a n-order polynomial to the results of Hillen *et al* (1991). If the scintillator of thickness t is divided into n sub-layers each of thickness Δt, then the effects of x-ray attenuation, optical photon generation and emission from each of the sub-layers can be modeled as

$$g_1(E)\, g_2(E,z) = \exp\left(-\mu_{CsI:Tl}(E)\, p_f\, (t-z)\right)\left[1-\exp\left(-\mu_{CsI:Tl}(E)\, p_f\, \Delta t\right)\right] g_2(E,z) \qquad [7]$$

where $\mu_{CsI:Tl}(E)$ is the linear attenuation coefficient of the scintillator and p_f is the packing fraction computed from the estimated scintillator surface density data. The number of optical quanta generated for an incident x-ray photon of energy E is

$$g_1(E)g_2(E) = \int_{z=t}^{0} g_1(E)g_2(E,z)dz \qquad [8]$$

and the mean quantum gain, $\bar{g}_2$ is (Siewerdsen 1997)

$$\bar{g}_2 = \frac{\int q_{rel}(E)g_1(E)g_2(E)dE}{\bar{g}_1} \qquad [9]$$

The quantum-gain variance of this stage can be expressed in terms of the Poisson excess and Swank factor computed from absorbed energy distributions (AEDs) (Swank 1973, Rowlands and Taylor 1983, Trauernicht and Van Metter 1988, 1990, Ginzburg and Dick 1993, Siewerdsen *et al* 1997, 1998a).

Scintillator Blur: The stochastic spread of optical quanta, $T_3(u,v)$ due to the scintillator, was experimentally determined by first measuring the pre-sampling modulation transfer function (MTF) and then deconvolving the effect of the finite pixel size of the imager (Williams *et al* 1999b, Vedantham *et al* 2004a). The resulting optical blur was fitted to a function of the form $1/1+Hf+Hf^2$ where H is the fit-parameter and f is the spatial frequency (Vedantham *et al* 2004a).

Optical Coupling and Absorption Efficiencies: The probability that an optical photon emanating from the scintillator reaches the imager via the fiber-optic plate is determined by the optical coupling efficiency, $\bar{g}_4$. The value of $\bar{g}_4$ was determined by the technique described by Hejazi and Trauernicht (1997) by taking into account fiber transmission, Fresnel reflection losses, and fiber core fill factor (Hejazi and Trauernicht 1997) and was

estimated to be about 0.41. The fiber related parameters were obtained from the manufacturer provided data (Schott North America Inc, Southbridge, MA). The QE of the imaging device, $\overline{g}_5$, was determined from the manufacturer (Fairchild Imaging Inc, Milpitas, CA) provided data sheet and was estimated to be 0.34 corresponding to the emission spectrum of CsI:Tl.

Pixel Presampling MTF: The pixel presampling MTF was approximated as the sinc response of the pixel, $T_6(u,v)$ with pixel dimensions a_x and a_y in the x and y directions being equal. A fill factor of 1 was used based on the pixel geometry of the imager modeled in this study except where specified.

Noise Power Spectra Aliasing and Additive noise: The experimentally estimated NPS in digital systems is always aliased due to the finite pixel geometry. In order to account for this effect, noise aliasing is introduced as described by Siewerdsen *et al* (1997, 1998a, 1998b). The total additive electronic noise was computed by taking into account dark current, integration time, quantization step size, and read noise. The values of the various noise terms are shown in Table 4.1. The noise values in terms of electrons were added in quadrature and the resulting additive noise was estimated as described by Vedantham *et al* (2004) and added to provide the NPS at the output of the final.

Clinical FFDM System Analysis

The clinical FFDM system was modeled similar to the description provided for the high-resolution imager with a few variations (Suryanarayanan *et al* 2004a):
(i) The clinical system has a fixed pixel pitch of 100 μm, (ii) a Lorentzian fit of the

form $1/\left(1+Hf^{2}\right)$ was used to fit the scintillator MTF data, (iii) the fiber optic coupling efficiency, $\overline{g}_4$ is set to unity as the scintillator is directly deposited on the a-Si:H substrate eliminating any fiber optics, (iv) based on measured transmission factors (Tkaczyk *et al* 2001), detector enclosure transmission factors, t_f were assume to be in the order 0.80 for the Mo/Mo spectra, 0.81 for MoRh, and 0.86 for RhRh with 45 mm PMMA filtration., (v) scintillator packing fraction was estimated to be 0.80 (~36.08 mg/cm^2) (Rowlands *et al* 2001), (vi) the photodiode coupling efficiency including the quantum efficiency was assumed to be 0.49 (Jee *et al* 2003), (vii) the pixel fill-factor was assumed to be 0.75 (Muller 1999), and (viii) additive noise was added based on empirical measurements of the dark NPS.

Results

X-ray Spectra

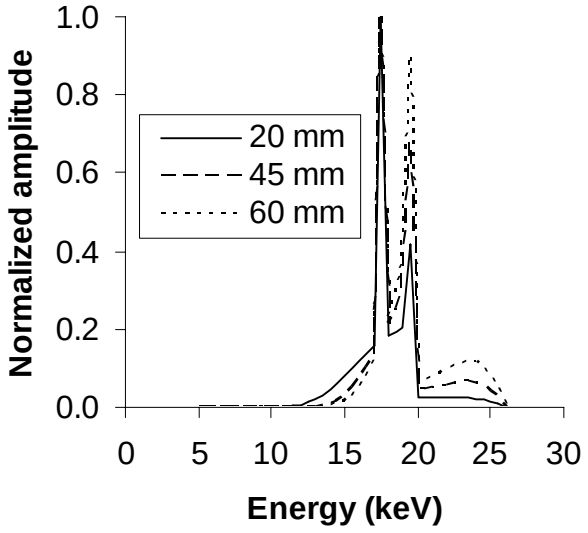

Figure 4.2*. Simulated x-ray spectra for various beam hardening conditions.*

X-ray spectral simulations for a 26 kVp, Mo/Mo target filter and various PMMA filter conditions are shown in Figure 4.2. The progressive decrease in low energy x-ray counts with increased filtration is noticeable. Similar simulations were performed for Mo/Rh and Rh/Rh conditions.

Prototype High-Resolution System

All the simulated $DQE(f)$ results reported in this section are for 26 kVp, Mo/Mo, 39 μm pixel, 150 μm CsI:Tl scintillator, 45 mm PMMA filtration, and 10 mR detector entrance exposure unless specified differently. The experimentally measured MTF for CsI:Tl scintillators with thickness in the range 150-525 μm is shown in Figure 4.3. The analytical function described previously appears to provide a good fit to the data. As expected, a decrease in MTF with increasing scintillator thickness was observed.

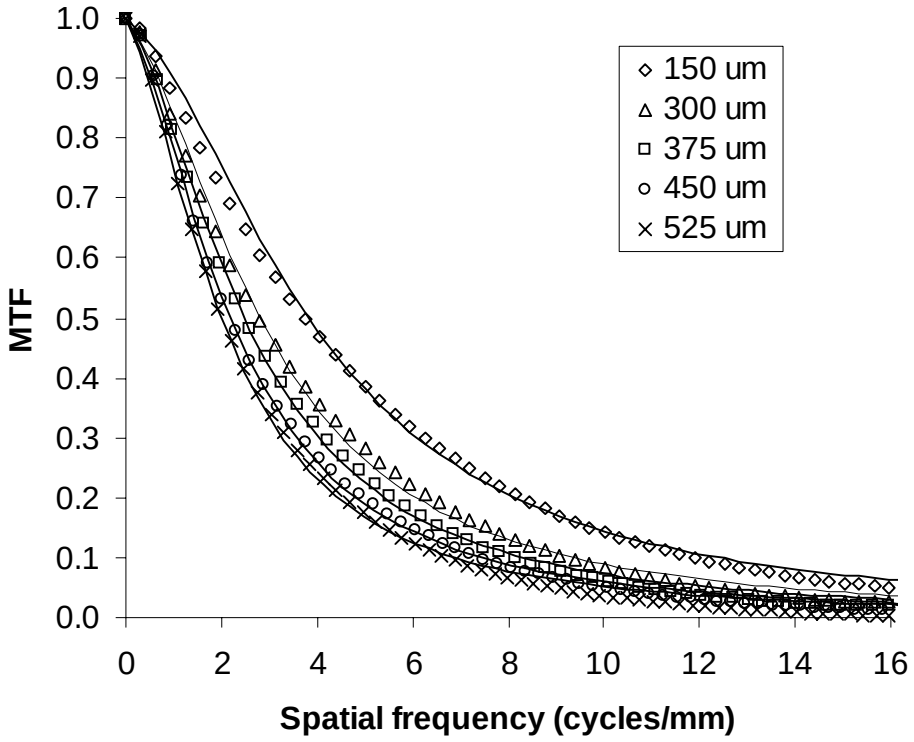

Figure 4.3. *Relationship between MTF fit parameter H and CsI:Tl scintillator thickness.*

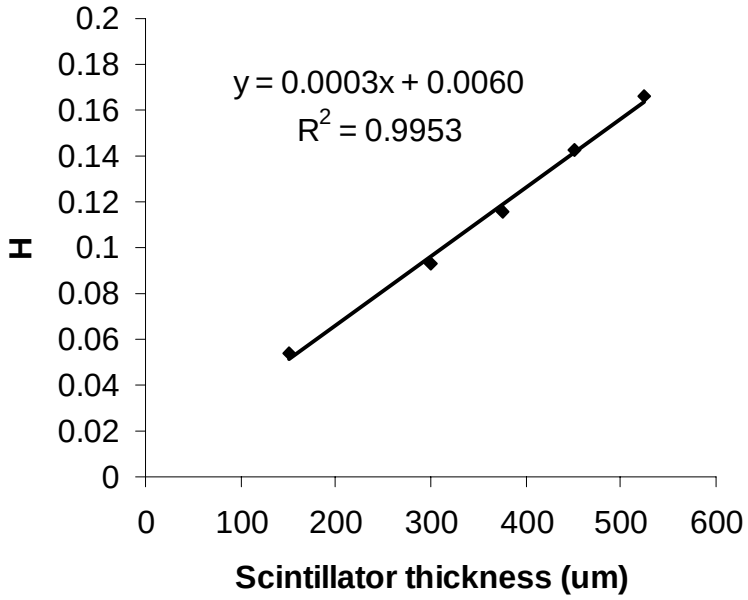

Figure 4.4. *Fitted empirical MTF data for various CsI:Tl scintillator thickness*

A plot of the MTF fit parameter *H* versus scintillator thickness is shown in Figure 4.4. Simulated scintillator MTF characteristics with estimated *H* parameter values are shown in Figure 4.5 for four thickness conditions.

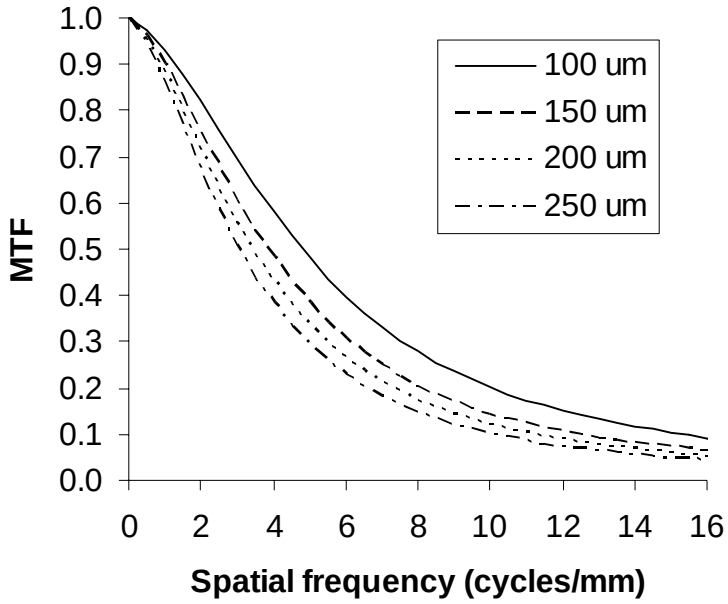

Figure 4.5*. Derived MTF for various CsI:Tl scintillator thickness conditions.*

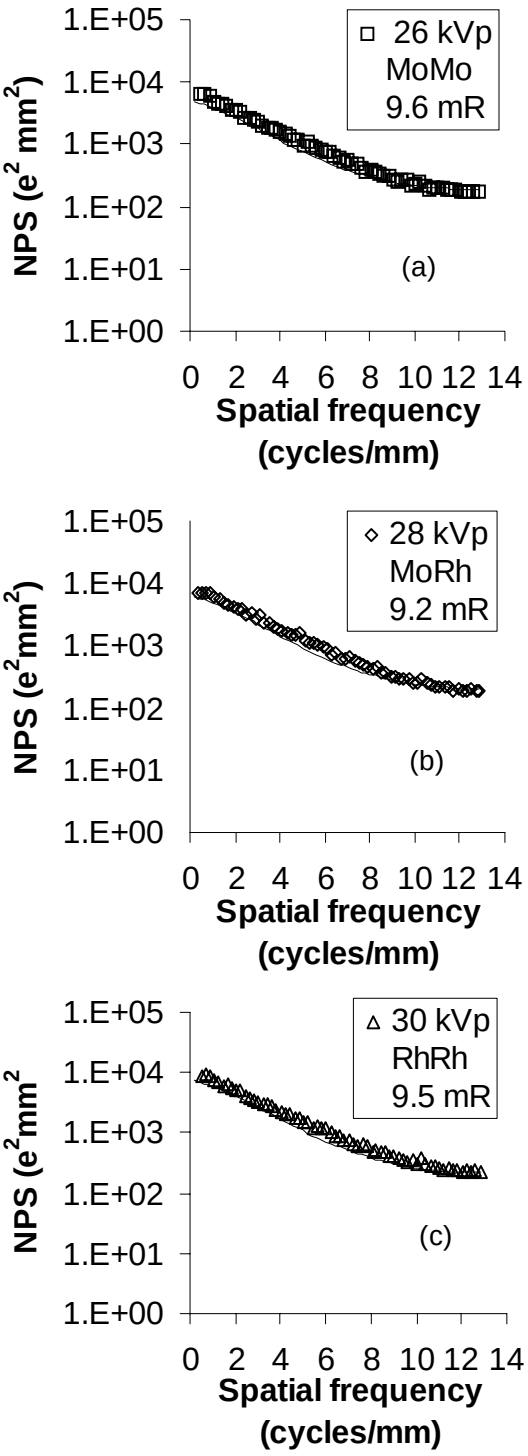

Figure 4.6. *Theoretical (smooth line) and experimental NPS(f) for (a) Mo/Mo, (b) MoRh, and (c) RhRh x-ray spectral conditions.*

The theoretically predicted $NPS(f)$ data show similar characteristics as experimentally estimated $NPS(f)$ under various x-ray spectral conditions (Figure 4.6). Further, the predicted $DQE(f)$ characteristics are similar to experimental measurements for various conditions thereby validating model performance (Figure 4.7).

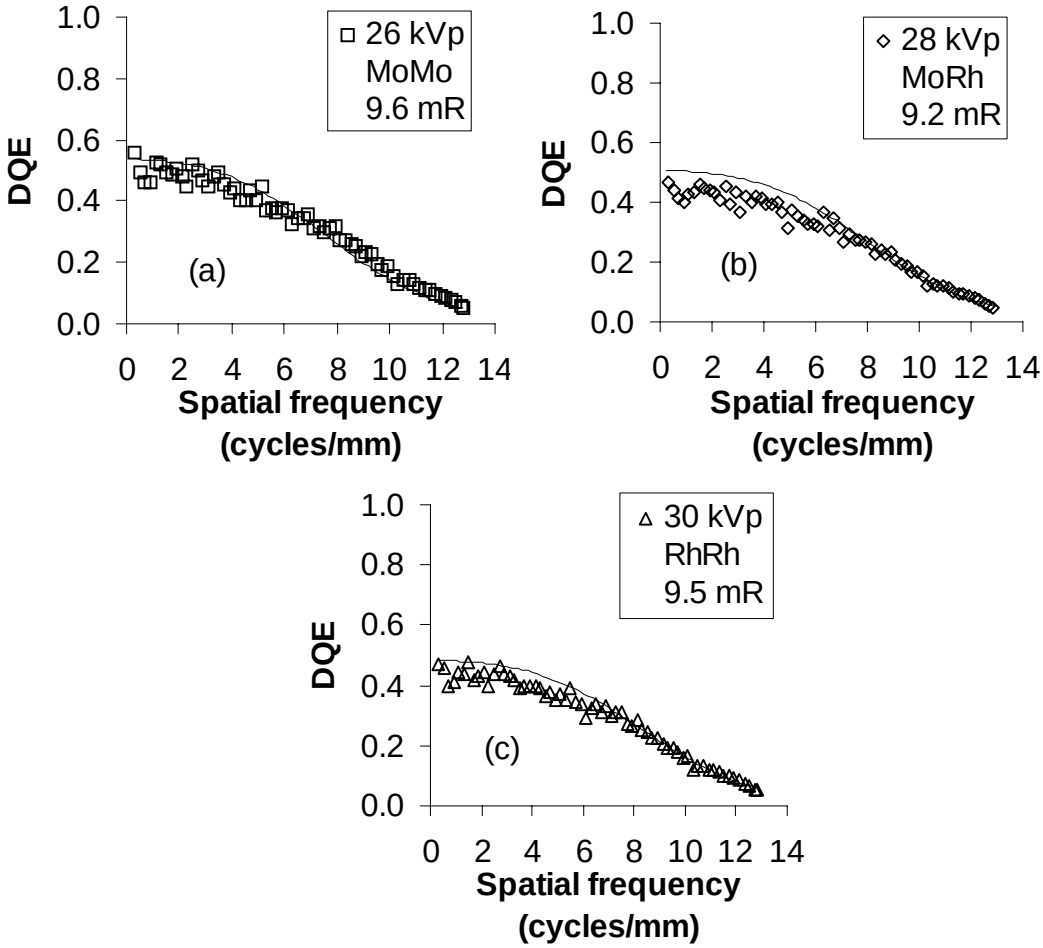

Figure 4.7. *Theoretical (smooth line) and experimental DQE(f) for (a) Mo/Mo, (b) MoRh, and (c) RhRh x-ray spectral conditions.*

The effect of scintillator thickness on $DQE(f)$ characteristics is shown in Figure 4.8 indicating an improvement in low frequency $DQE(f)$ and degradation in high-frequency

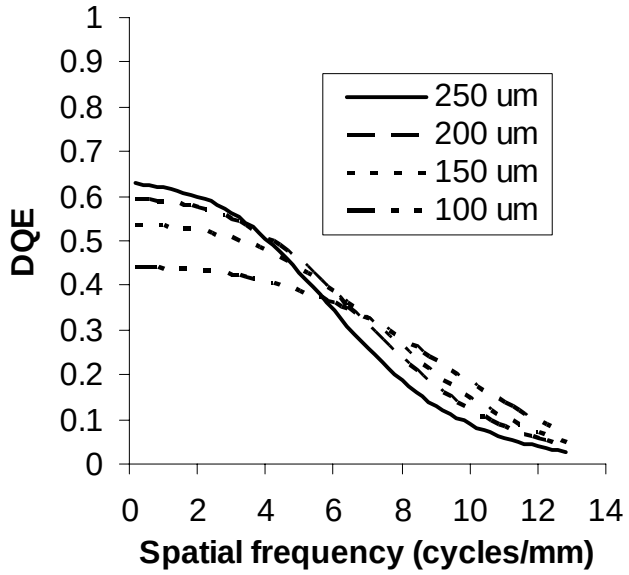

Figure 4.8. *Effect of CsI:Tl scintillator thickness on DQE(f).*

$DQE(f)$ with increasing thickness. Variation in pixel size with a 150 μm-thick CsI:Tl scintillator resulted in a noticeable decrease in zero frequency DQE, $DQE(0)$ for a 12 μm pixel configuration while large pixels appear to have a negligible effect (Figure 4.9).

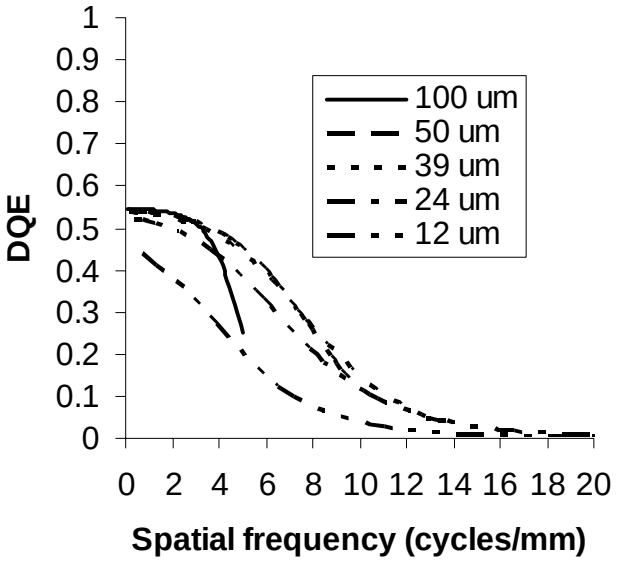

Figure 4.9. *Effect of pixel size on DQE(f).*

The packing efficiency of the scintillator appears to have a direct impact on $DQE(f)$ across all spatial frequency components (Figure 4.10). Decreasing optical coupling efficiency between the scintillator and fiber optics shows a progressive

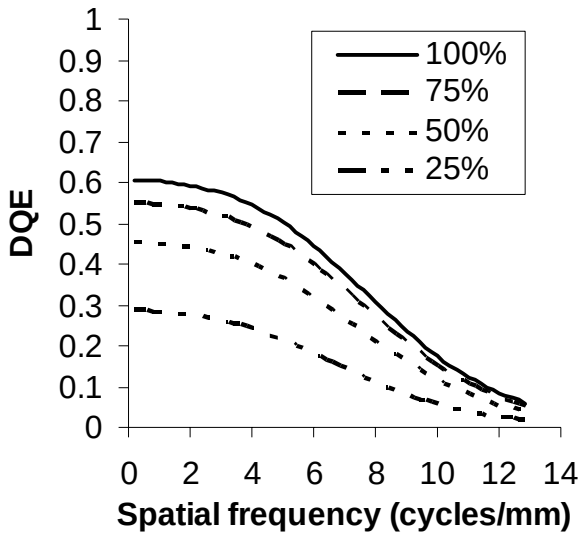

Figure 4.10. *Effect of CsI:Tl scintillator packing fraction on DQE(f).*

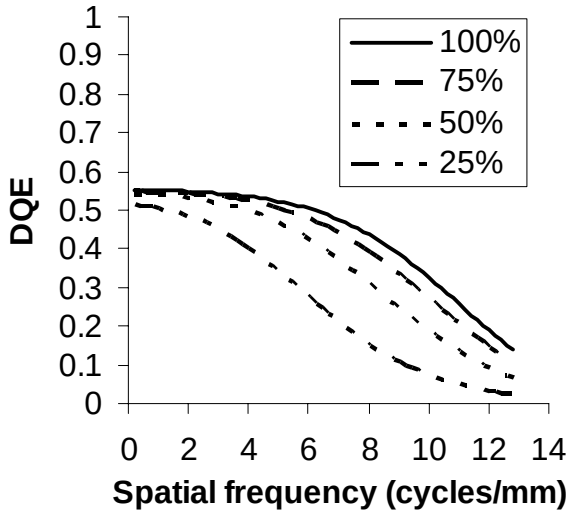

Figure 4.11. *Effect of optical coupling efficiency on DQE(f).*

reduction in $DQE(f)$ from higher to lower spatial frequencies (Figure 4.11). The effect of charge integration time is shown in Figure 4.12 that indicates a decrease in $DQE(f)$ with increasing integration time due to increased dark noise accumulation. The

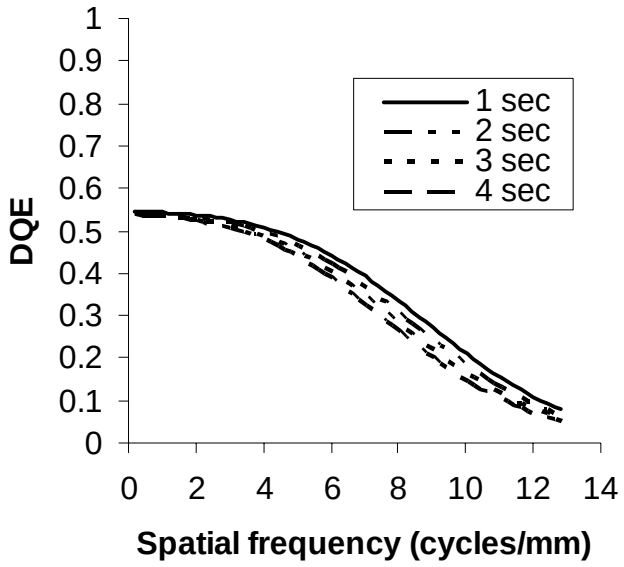

Figure 4.12. *Effect of integration time on DQE(f).*

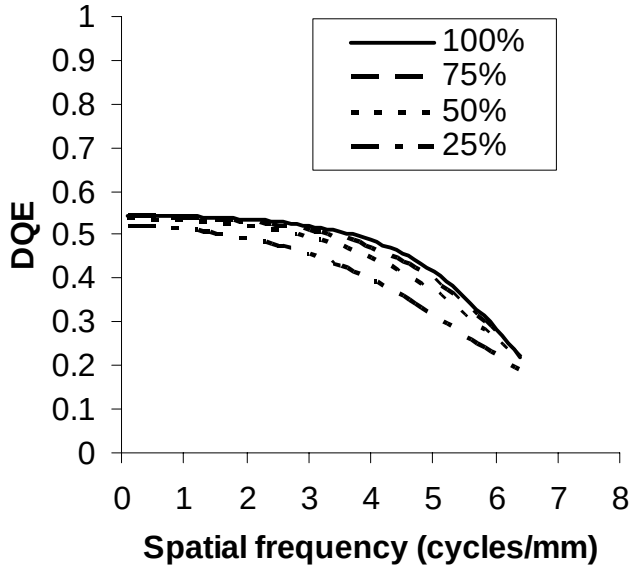

Figure 4.13. *Effect of pixel fill-factor on DQE(f). A pixel size of 78 μm was used for this simulation.*

effect of pixel fill-factor for a 78 mm pixel size is shown in Figure 4.13.

Clinical FFDM System

The theoretically predicted and empirically measured $DQE(f)$ data for 26 kVp, with 45 mm PMMA filtration at ~ 10 mR detector entrance exposure for various target/filter conditions is shown in Figure 4.14.

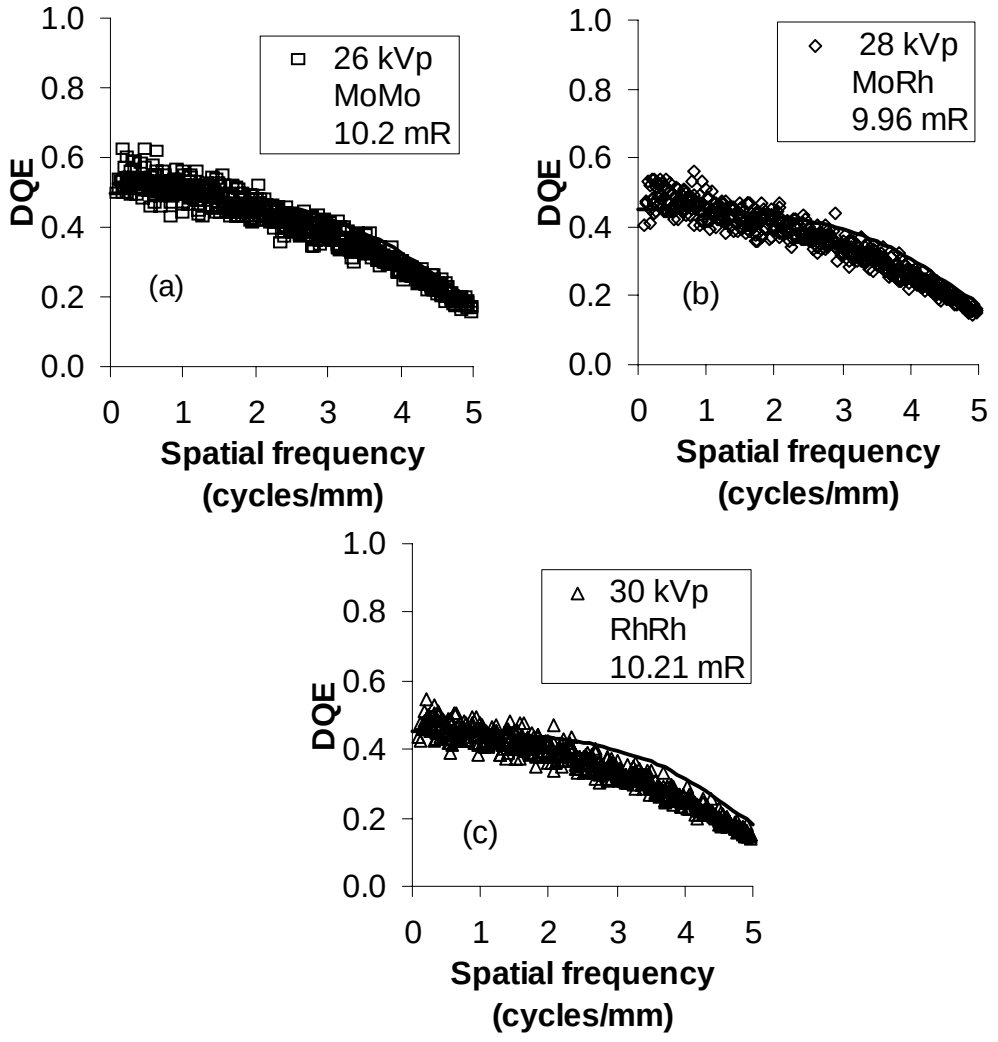

Figure 4.14. *Theoretical (smooth line) and experimental DQE(f) for (a) Mo/Mo, (b) MoRh, and (c) RhRh x-ray spectral conditions for the clinical FFDM system .*

Comparison of Prototype and Clinical FFDM System

The computed $DQE(0)$ for the prototype imager with 39 μm pixel pitch and an a-Si:H-based clinical FFDM with 100 μm pixel pitch at various exposures are nearly identical (Figure 4.15a). In order to model the $DQE(0)$ for the a-Si:H imager an additive noise was assumed to be 1500 e- rms (Siewerdsen *et al* 1997, Glick *et al* 2002). The data in Table 4.1 was used to compute the additive noise for the prototype. For the $DQE(f)$ of the clinical FFDM system, the empirically estimated additive noise in e^2mm^2 was used. The high-resolution prototype exhibits much better $DQE(f)$ characteristics (Figure 4.15b).

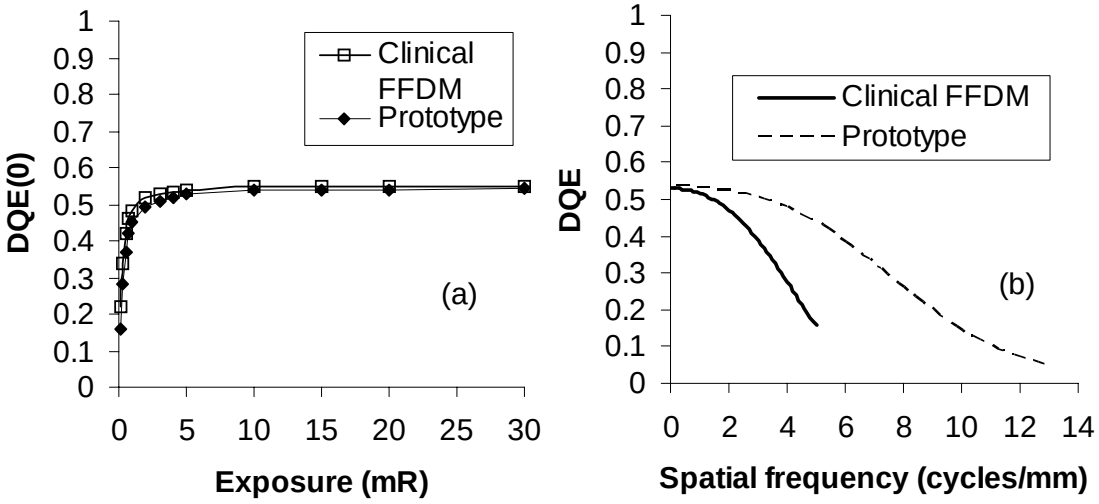

Figure 4.15*. (a) DQE(0) and (b) DQE(f) comparison between the high-resolution prototype and clinical FFDM system.*

Discussion

The MTF characteristics, over the range of scintillator thickness conditions that were studied (100-250 μm) (Figure 4.5), appear to be suitable for digital mammography and comparable to existing clinical FFDM systems (Suryanarayanan *et al* 2004a, Suryanarayanan *et al* 2005). Due to the small pixel architecture of the imager, thicker scintillators could be used for improved $DQE(0)$ at the expense of MTF. However, due to smaller pixel sizes, the resolution capabilities of the imager might still be adequate even with a drop in MTF, due to increased scintillator thickness. Improvement in MTF performance could be achieved by advanced pixilated scintillator designs (Nagarkar *et al*). The theoretical computations agree well with experimental $NPS(f)$ (Figure 4.6) and $DQE(f)$ (Figure 4.7) characteristics (Suryanarayanan *et al* 2005) at different x-ray spectral conditions and can potentially be applied to model other similar imaging configurations. The increase in $DQE(0)$ with increasing scintillator thickness (Figure 4.8) is attributed to the proportional increase in quantum efficiency (QE). However, the decrease in $DQE(f)$, at higher spatial frequencies is due to the degradation in optical blur with increasing scintillator thickness. Nevertheless, the $DQE(f)$ exhibits substantial improvement to about 5 cycles/mm for the pixel size and range of scintillator thickness conditions studied, given that many clinical FFDM units have a Nyquist sampling limit of 5 cycles/mm (Suryanarayanan *et al* 2004a). The reduction in high frequency $DQE(f)$ at larger pixel sizes (Figure 4.9) could be attributed to aliasing effects that tend to increase the $NPS(f)$ below the Nyquist limit. The substantial decrease in $DQE(f)$, with a 12 μm pixel configuration (Figure 4.9), can be attributed to the reduced signal per unit area

and to the larger contribution of additive noise to total system noise. Scintillator packing density has a direct effect on the overall $DQE(f)$ across all spatial frequencies due to its direct impact on QE (Figure 4.10). Since QE has a direct bearing on the relative amplitude of $DQE(f)$ irrespective of frequency, an increase in QE translates into an overall increase in $DQE(f)$. The degradation in $DQE(f)$, with decreasing optic coupling efficiency, is due to the reduction in signal contribution and quantum noise contribution to the total system noise (Figure 4.11). Simulation results for the conditions in this study indicate that increasing coupling efficiency is likely to enhance $DQE(f)$, especially in the mid to high spatial frequency range. Higher optical coupling efficiency could potentially be attained by using index matching materials between the coupling layers and eliminating intermediate stages, such as fiber optic face plates, provided the imager is protected or is not susceptible to damage due to direct x-ray interactions. Dark current and charge integration time have similar effects on $DQE(f)$ in that an increase in either parameter causes a reduction in $DQE(f)$ (Figure 4.12). This is expected, as increase in integration time leads to an increase in dark noise, thereby degrading $DQE(f)$. Typically, a one second acquisition time frame should suffice for an average breast thickness but exposure times in the order of 0.5-3 seconds are typically encountered in mammography. Further, reduction in dark noise can be achieved by using suitable semiconductor bulk materials or through cooling mechanisms. Read noise can be reduced by designing low noise electronics. Reduction fill-factor reduces the signal capacity of the pixel as the active area of the pixel decreases which reduces $DQE(f)$. It also degrades the pixel presampling MTF which results in

faster $DQE(f)$ roll-off as fill-factor decreases (Figure 4.13). It should be noted that CCDs offer 100% fill-factor and reduced fill-factors are usually observed with other technologies such as a-Si:H and a-Se.

The clinical FFDM system exhibits favorable $DQE(f)$ characteristics for mammography. The progressive decrease in $DQE(f)$ with Mo/Rh and Rh/Rh target-filter combinations compared to Mo/Mo can also be attributed to the reduction in quantum efficiency of the scintillator due to the relative increase in the higher energy component of the x-ray spectra. Overall, the model agrees well with the empirical data under these conditions (Figure 4.14).

The similar $DQE(0)$ performance between the two imaging systems (Figure 4.15a) illustrates the potential for high-resolution digital mammography with pixel sizes much less than 100 μm. The better $DQE(f)$ performance of the prototype at higher frequencies is also encouraging (Figure 4.15b) and could facilitate better microcalcification detection and characterization.

Conclusion

The purpose of this study was to simulate and assess the impact of various parameters on the performance of a high-resolution digital mammography system. The values of the input parameters used in the model were based on published values or reasonable assumptions. However, the model described here can be used to identify trends during system design. Further, system specific parameters, when available, can be

used in conjunction with similar mathematical modeling to develop a well performing application specific imaging system.

CHAPTER 5

EXPERIMENTAL SYSTEM ANALYSIS OF DIGITAL MAMMOGRAPHY

Introduction

The physical characteristics of the prototype high-resolution single module imager and the clinical FFDM system were studied (Suryanarayanan *et al* 2005). Metrics such as $MTF(f)$, $NPS(f)$, noise equivalent quanta, $NEQ(f)$ and $DQE(f)$ were investigated under various clinically relevant mammographic spectral conditions that included three target/filter combinations (Mo/Mo, Mo/Rh, and Rh/Rh). The goal was to analyze the performance of the prototype imager and benchmark it against the clinical FFDM system in order to determine the clinical viability of such high-resolution platforms from a physical standpoint. If a high-resolution system does not exhibit favorable noise and $DQE(f)$ characteristics, then the development of such platforms is likely to lose its significance. Hence, the complete characterization of these devices is very important. This chapter is organized as follows: first, the methods used to measure and compute the $DQE(f)$ of the prototype high-resolution system is described, followed by the techniques used to compute the $DQE(f)$ of the clinical FFDM system. Finally, some of the results between the systems are compared.

Methods

The following empirical methods were used for $DQE(f)$ computation under various x-ray spectral conditions.

Prototype High-Resolution System

Presampling $MTF(f)$ *Measurements*: The presampling $MTF(f)$ was measured using the slanted slit-technique (Fujita *et al* 1992) under the following x-ray spectral conditions: 26 kVp: Mo/Mo, 28 kVp: Mo/Rh, and 30 kVp, Rh/Rh. A 10 μm ($\pm$ 1 μm) wide slit (Cardinal Health, Hicksville, NY) made from tungsten of thickness 1.5 mm, and length 5.5 mm ($\pm$ 0.1 mm), was placed at a slight angle (less than 4^o) both along and perpendicular to the anode cathode-axis at the center of the detector and the area around the slit was covered with Pb in order to prevent imager saturation at very high exposures and also to reduce any scatter that may be present around the slit area. No anti-scatter grid, breast support plate or PMMA was present in the x-ray beam path and the slit was placed on top of the detector cover-plate. The source-to-imager (SID) distance was set to 66 cm. The tube voltage (kVp) was fixed for a given target-filter combination and the mAs varied to obtain line spread functions (LSFs) with tails that were not significantly affected by electronic noise after subtraction of a dark image, which was acquired without an x-ray exposure. A finely sampled LSF was generated from individual LSFs

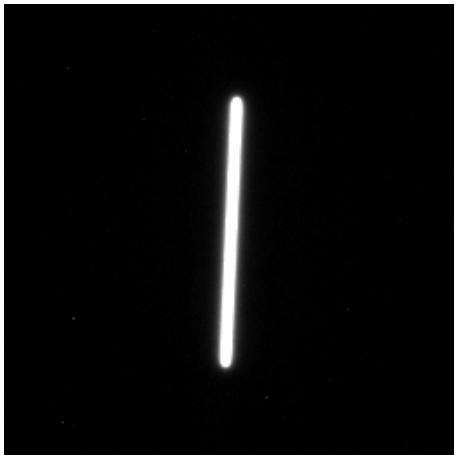

Figure 5.1. *Radiographic image of the slit used for MTF measurements.*

and normalized to a peak value of one, which was Fourier transformed (FT) and deconvolved of the finite dimension of the slit by dividing the resultant FT by the sinc of the slit width in the frequency domain to provide the presampling $MTF(f)$ (Fujita *et al* 1992). A radiographic image of the slit is shown in Figure 5.1.

Noise Power Spectra Measurements: The $NPS(f)$ was first determined under the following spectral conditions: 26 kVp: Mo/Mo, 28 kVp: Mo/Rh, and 30 kVp: Rh/Rh with PMMA blocks of thickness 20, 45, and 57 mm mounted on the output of the tube housing. A total of nine different spectral conditions were investigated in this part of the study as outlined in Table 5.1. A range of exposures between 9.2 to 10.5 mR was maintained at detector entrance for all the nine different conditions as shown in Table 5.1. The $NPS(f)$ were also measured at 26 kVp:Mo/Mo with 45 mm of PMMA mounted on the tube housing at detector entrance exposures of 1.1, 4.8, 9.6, and 19.4 mR. Anti-scatter grid was not used for any of the $NPS(f)$ measurements and the collimator was adjusted to the smallest setting that the system would allow, so that the collimated x-ray beam was 9 x 9 cm at the surface of the detector. For each spectral and PMMA thickness

Table 5.1. Exposure conditions that were used for $NPS(f)$ estimation of the high-resolution prototype system at various kVp, target/filter, and PMMA thickness combinations.

PMMA thickness (mm)	26 kVp Mo/Mo	28 kVp Mo/Rh	30 kVp Rh/Rh
20	9.6	9.7	10.2
45	9.6	9.2	9.5
57	10	10.5	9.7

condition, 25 “flood” images ere acquired immediately after the acquisition of 25 “dark” images that were acquired at the same exposure time period but without x-rays. The

acquisition time of the CCD was set at 4 seconds for all exposures because automatic synchronization between the digital imager and the x-ray generator was not available. Offset correction was performed by subtracting each dark frame from a subsequently acquired flood image frame. Using an acquisition period of 4 seconds ensured complete capture of the x-ray exposure by the imager. A region of interest (ROI) consisting of 768 x 768 pixels was cropped from each image and corrected for bad-pixels and field non-uniformity. Bad pixels were deemed as those that deviated from the mean by more than 10 standard deviations (Bath *et al* 2002) which were about 0.14-0.16% of the pixels in each image ROI. The images were then flat-field corrected by dividing each image ROI by an average ROI image and scaling the result by the mean value of the average ROI image. An example of flat correction is shown in Figure 5.2.

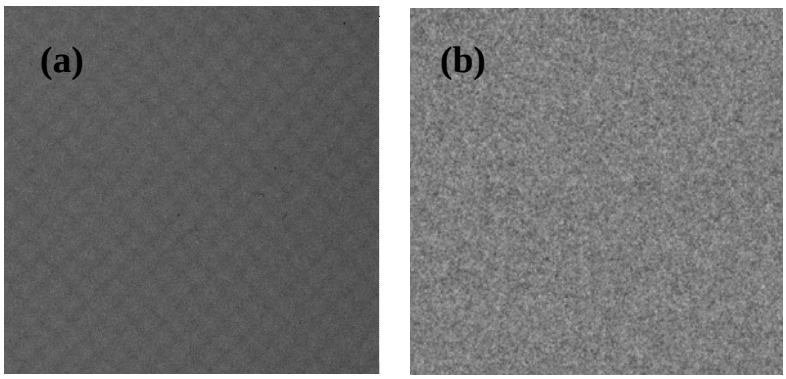

Figure 5.2. *Example of an image ROI (a) before and (b) after flat correction.*

For each experimental condition, nine, non-overlapping 256 x 256 pixel ROIs were extracted from each 768 x 768 pixel image resulting in 225 ROIs (25 x 9) that were used for NPS analysis. Preceding NPS estimation, the ROIs were trend corrected by fitting a two-dimensional polynomial surface fit to the data values in each ROI and

subtracting it from the corresponding ROI (Samei and Flynn 2003). The mean signal value, μ_{ROI} of each ROI was subtracted from the ROI image as

$$difference\ ROI_{Struc}(x,y) = ROI(x,y) - \mu_{ROI} \quad [1]$$

to obtain 'zero mean' images which were used in computing the ensemble average of the squares of the magnitude of the Fourier transformed images. The raw NPS was estimated as described by Dobbins *et al* 1995 as

$$NPS_{raw}^{struc}(u,v) = \frac{\left\langle \left| FFT(difference\ ROI_{struc}(x,y) \right|^2 \right\rangle}{N_x N_y} \Delta_x \Delta_y \quad [2]$$

where Δ_x and Δ_y are the pixel sizes in x and y directions respectively, (Δ_x = 0.039 μm, Δ_y = 0.039 μm) and N_x and N_y are the number of elements in the x and y direction respectively, (N_x = 256, N_y = 256). The normalized NPS was then obtained as (Dobbins *et al* 1995)

$$NPS_{norm}^{struc}(u,v) = \frac{NPS_{raw}^{struc}(u,v)}{(mean\ signal\ of\ \ average\ ROI)^2} \quad [3]$$

A two-dimensional (2D) NPS was obtained that included the fixed pattern noise of the detector and a one-dimensional (1D) NPS, $NPS(f)$ where $f = \sqrt{u^2 + v^2}$ was obtained by averaging 4 rows on either side of the horizontal axis (serial read direction that is perpendicular to chest wall), $'u'$ and vertical axis (parallel read direction that is parallel to chest wall), *'v'*, of the 2D NPS (Dobbins *et al* 1995).

In addition, $NPS(f)$ estimation was performed subtracting an average image from each of the 768 x768 image ROIs. This was done in order to check for any

differences in $NPS(f)$ due to elimination of fixed pattern and varying non-stochastic effects (Williams *et al* 1999a).

$$difference\ ROI_{No\ Struc}(x,y) = ROI(x,y) - \langle ROI(x,y) \rangle \quad [4]$$

The subtracted ROIs were then used to compute $NPS_{raw}^{No\ Struc}(u,v)$ and $NPS_{norm}^{No\ Struc}(u,v)$ using the formalism specified in Equations 2 and 3. In this case, the NPS was corrected for the loss in variance introduced due to the background subtraction procedure in Equation 4 (Granfors and Aufrichtig 2000, Floyd *et al* 2001). The NPS was analyzed both along the serial and parallel read directions of the prototype imager.

Detective Quantum Efficiency Computation: The $DQE(f)$ was computed from the measured $MTF(f)$ and $NPS(f)$ as

$$DQE(f) = \frac{MTF^2(f)}{NPS_{norm}(f) q_0} \quad [5]$$

where q_0 is in photons/mm^2. The value of q_0 / X where X is the exposure (mR) was computed based on the definition of Roentgen (Johns and Cunningham 1983). Spectral simulations were performed as described in chapter 4 under the "Imaging Stages" section. The procedure described for "Incident X-ray Quanta" in chapter 4 was used with the appropriate amount of PMMA. No cover transmission was included here as the x-ray exposure prior to entering the imager was desired. The incident exposure was measured with a calibrated mammographic ionization chamber and exposure meter (MDH 1515, RadCal Corp., Monrovia, CA). The exposures were measured a few centimeters above the detector plane and corrected using inverse square law. Lead sheets were placed below the chamber to minimize back scatter.

Clinical FFDM System

The methods described in the previous section were used to compute the $DQE(f)$ of the clinical FFDM system (Suryanarayanan *et al* 2004a) under various x-ray spectral conditions as shown in Table 5.2. Unlike the prototype system, the images from the clinical system are already bad-pixel and flat-field corrected which obviated the need for such correction steps (Suryanarayanan *et al* 2004a). Further, the structural components in the clinical imager were negligible after correction, and hence, the structure free $NPS(f)$ was estimated for all conditions (Equation 4 followed by Equations 2,3, and 5).

Table 5.2. Exposure conditions that were used for $NPS(f)$ estimation for the clinical FFDM system at various kVp, target/filter, and PMMA thickness combinations.

PMMA thickness (mm)	26 kVp Mo/Mo	28 kVp Mo/Rh	30 kVp Rh/Rh
20	10.2	10.4	9.8
45	10.2	10.0	10.2
60	10.3	10.7	10.2

Results

Prototype High-Resolution System

The signal response of the imager is linear over the range of detector entrance air kerma conditions that were used in this study as shown in Figure 5.3. The presampling $MTF(f)$ that was measured along the parallel read direction without any PMMA in the beam for Mo/Mo, Mo/Rh and Rh/Rh target/filter combinations is shown in Figure 5.4a. The spatial resolution at the 10% $MTF(f)$ level is close to 10cycles/mm. The $MTF(f)$ curves along the parallel read direction and the serial read direction measured at 26 kVp

for Mo/Mo are nearly identical indicating a symmetric response along orthogonal directions as shown in Figure 5.4b.

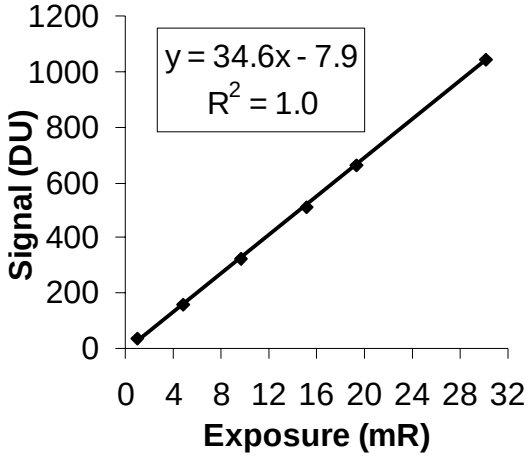

Figure 5.3. *Mean large area signal characteristics of the imager indicate a linear response over a range of detector entrance exposure conditions.*

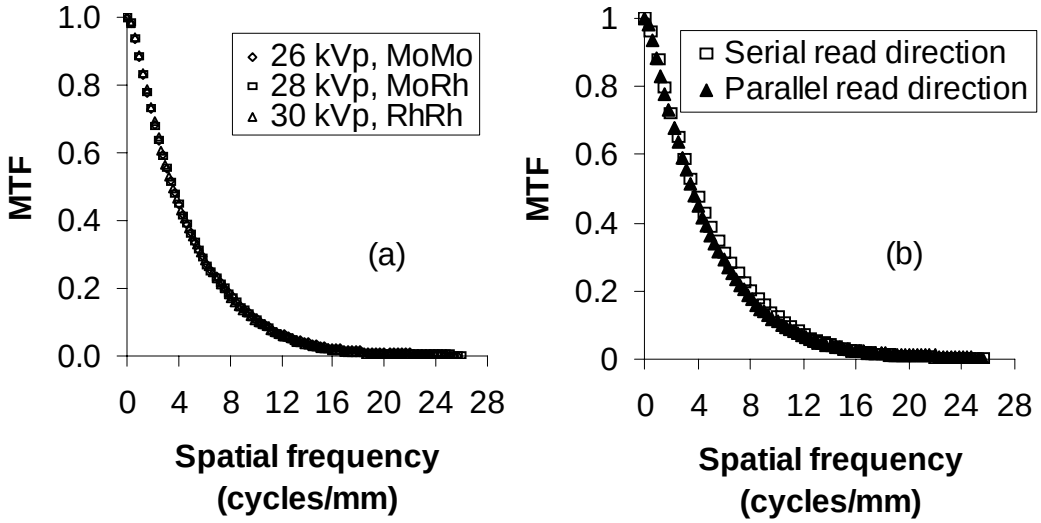

Figure 5.4*. Measured MTF(f) characteristics of the system at (a) various target/filter and kVp conditions and (b) CCD serial and parallel readout directions .There appears to be no degradation in characteristics under these conditions.*

The normalized two-dimensional dark image NPS and the NPS obtained with 26 kVp, Mo/Mo and 45 mm PMMA (9.6 mR) are shown in Figure 5.5 respectively. The

one-dimensional NPS along the serial and parallel read directions for the 26 kVp, Mo/Mo with 45 mm PMMA condition obtained at detector entrance exposure of 9.6 mR is shown in Figure 5.6 indicating virtually identical NPS along orthogonal directions. The NPS with and without fixed pattern noise is shown in Figure 5.7 indicating negligible effect of such noise sources.

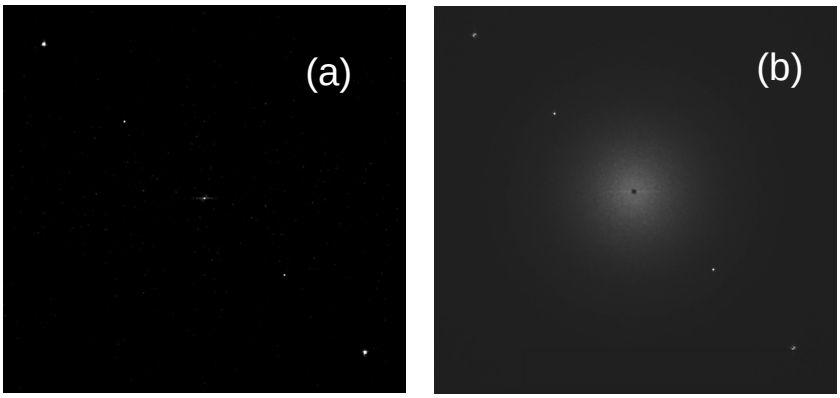

Figure 5.5*. Estimated two-dimensional NPS(u,v) under (a) no x-ray exposure (dark) and (b) entrance exposure of 9.6 mR.*

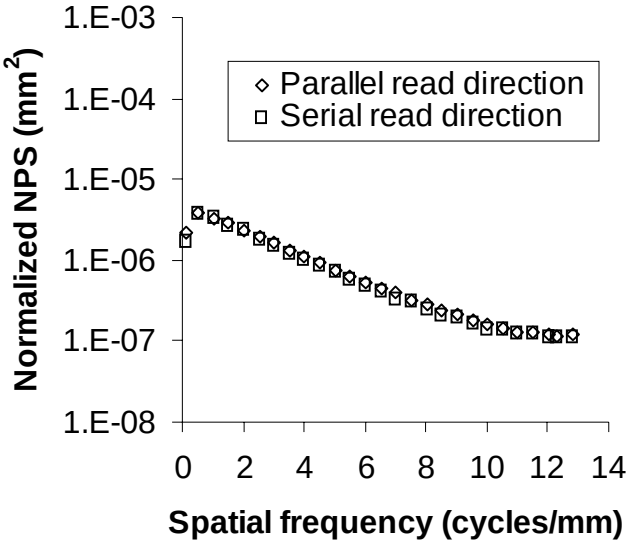

Figure 5.6. *Normalized NPS(f) along orthogonal directions for the 26 kVp, Mo/Mo, 45 mm PMMA spectral condition at ~10 mR showing nearly identical spatial frequency response.*

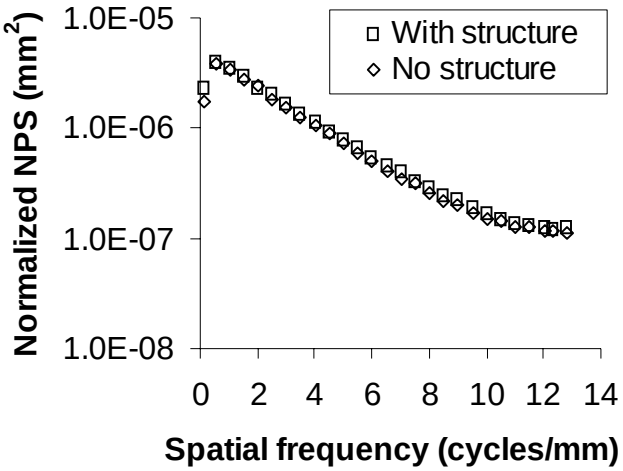

Figure 5.7*. Comparion of NPS(f) with and without fixed pattern noise correction.*

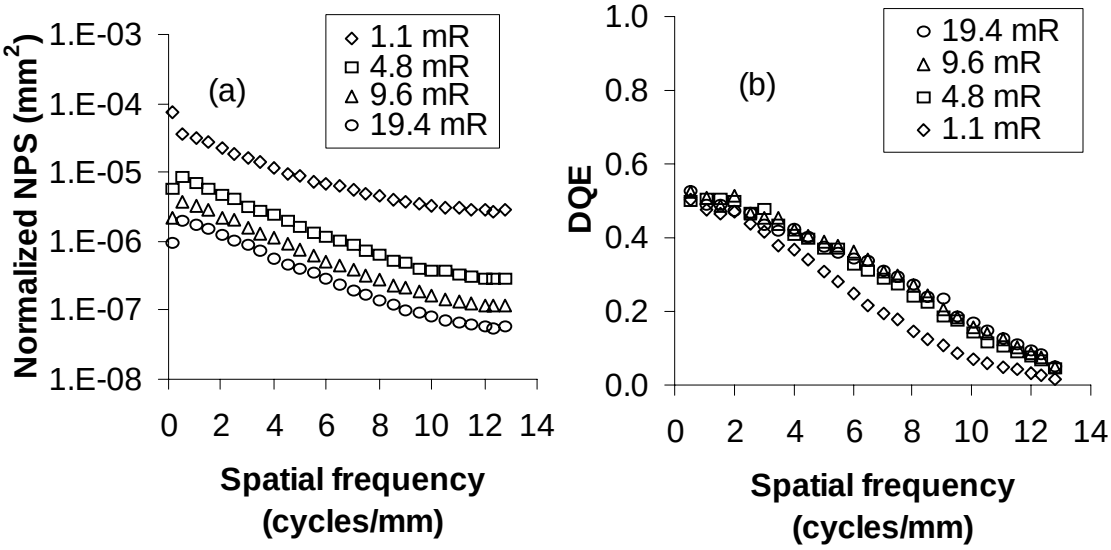

Figure 5.8. *Exposure dependence of (a) normalized NPS(f) and (b) DQE(f) response of the prototype imager for 26 kVp, Mo/Mo spectra with 45 mm PMMA.*

The dependence of $NPS_{normalized}(f)$ and $DQE(f)$ for the 26 kVp, Mo/Mo and 45 mm PMMA configuration on the detector entrance exposure is shown in Figures 5.8a and 5.8b indicating a decrease in $DQE(f)$ at spatial frequencies greater than 2 cycles/mm at

~1 mR. There appears to be negligible variation in $DQE(f)$ with detector entrance exposures in the range of ~5-19 mR. For each PMMA thickness that was used in this study, the $NEQ(f)$ along the serial CCD read direction exhibits a marginally increasing trend with increasing kVp and corresponding target/filter combination (Figure 5.9). A similar trend in $NEQ(f)$ was observed along the parallel CCD read direction.

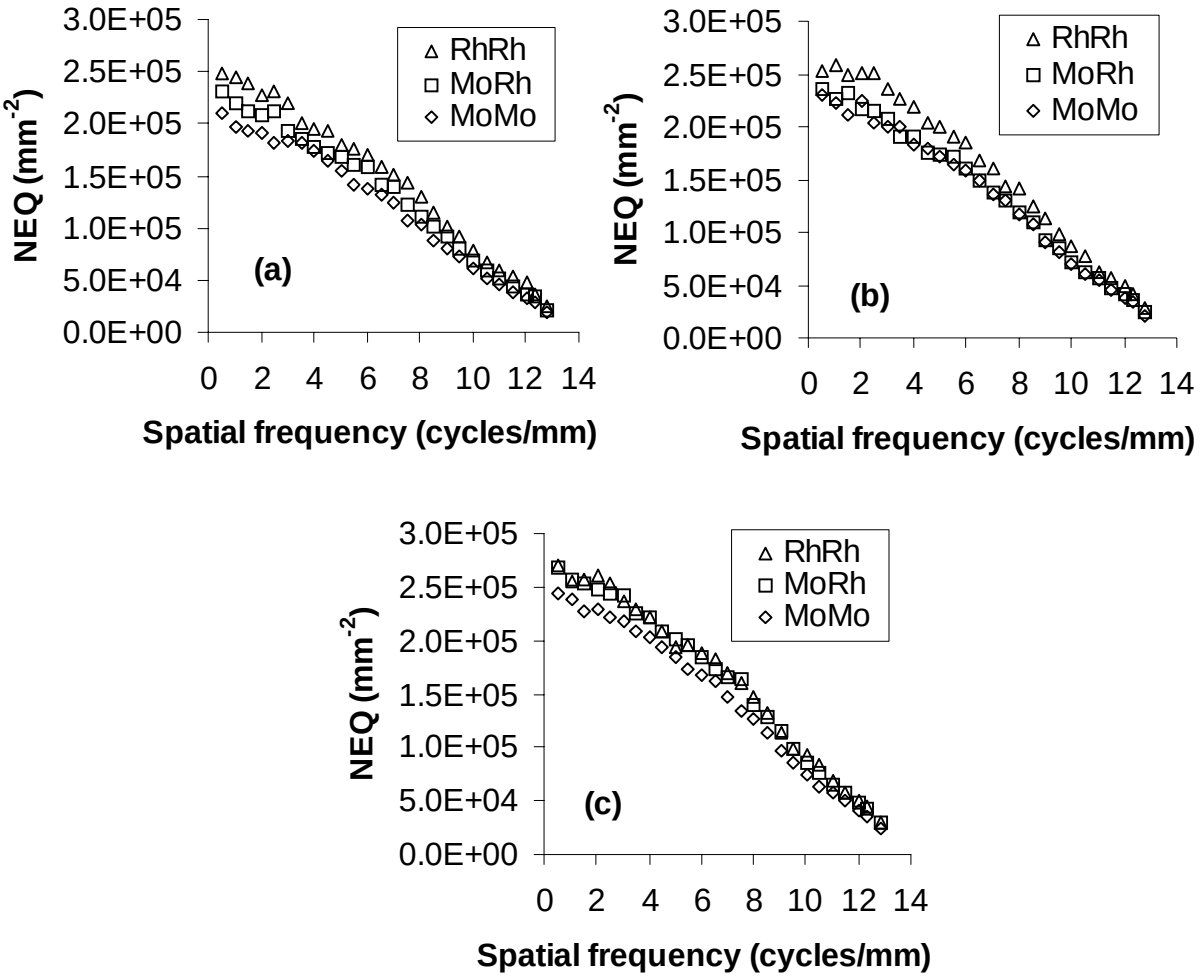

Figure 5.9*. NEQ(f) along the serial read direction with (a) 20 mm, (b) 45 mm, and (c) 57 mm PMMA filtration at 26 kVp, Mo/Mo, 28 kVp, Mo/Rh and 30 kVp, Rh/Rh measured ~10 mR (Table 5.1). Both an increase in x-ray spectral hardening and shifting to higher energy spectra results in a marginal increase in NEQ(f).*

For each PMMA thickness that was used in this study, a marginal decrease in low to mid-frequency $DQE(f)$ is observed along both serial and parallel CCD read directions with increasing kVp and corresponding target/filter combination as shown in Figures 5.10 and 5.11 respectively.

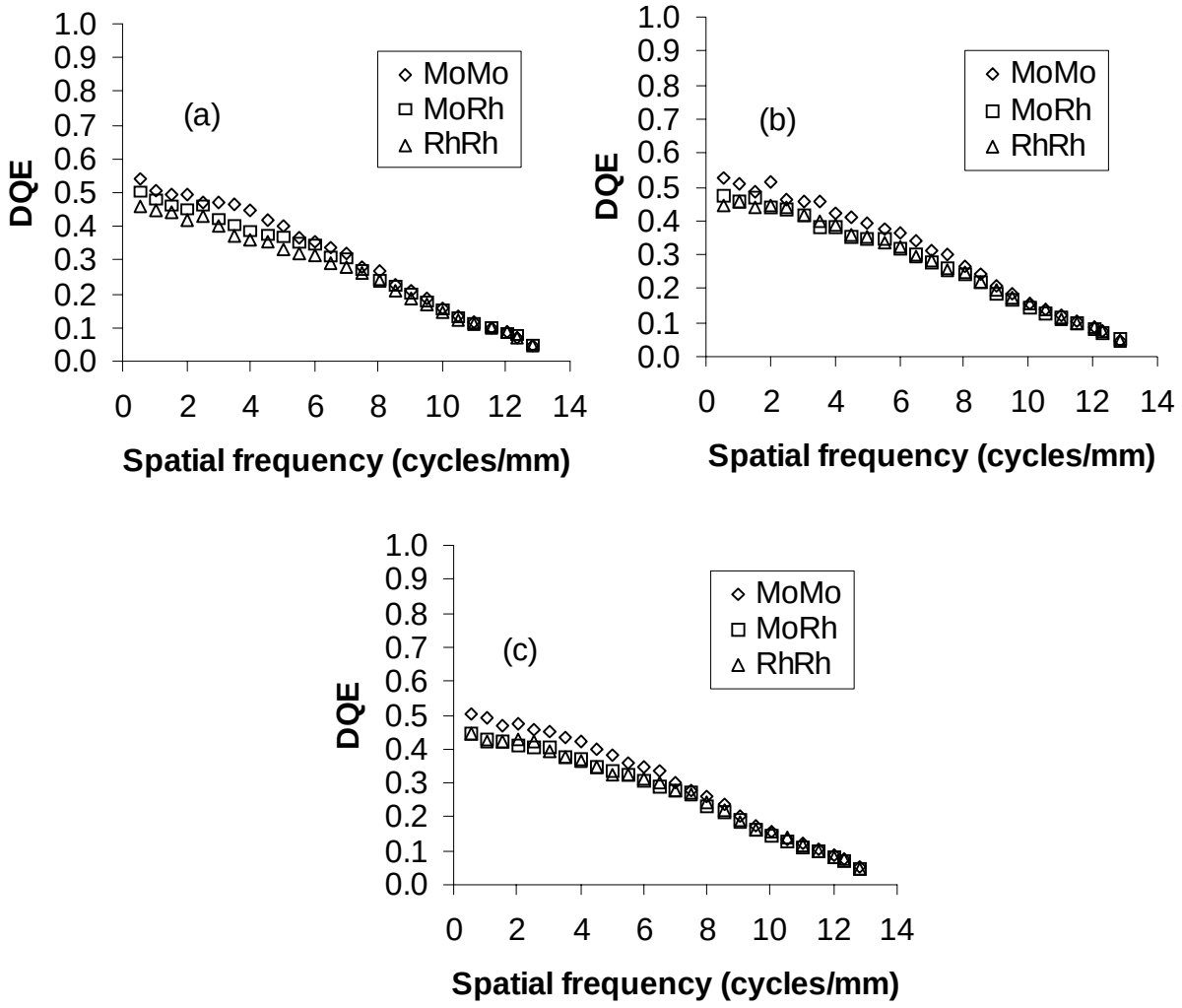

Figure 5.10. *DQE(f) along the serial read direction with (a) 20 mm, (b) 45 mm, and (c) 57 mm PMMA filtration at 26 kVp, Mo/Mo, 28 kVp, Mo/Rh, and 30 kVp, Rh/Rh measured ~10 mR (Table 5.1). A marginal decrease in* $DQE(f)$ *is observed with Mo/Rh and Rh/Rh compared to Mo/Mo target/filter combinations.*

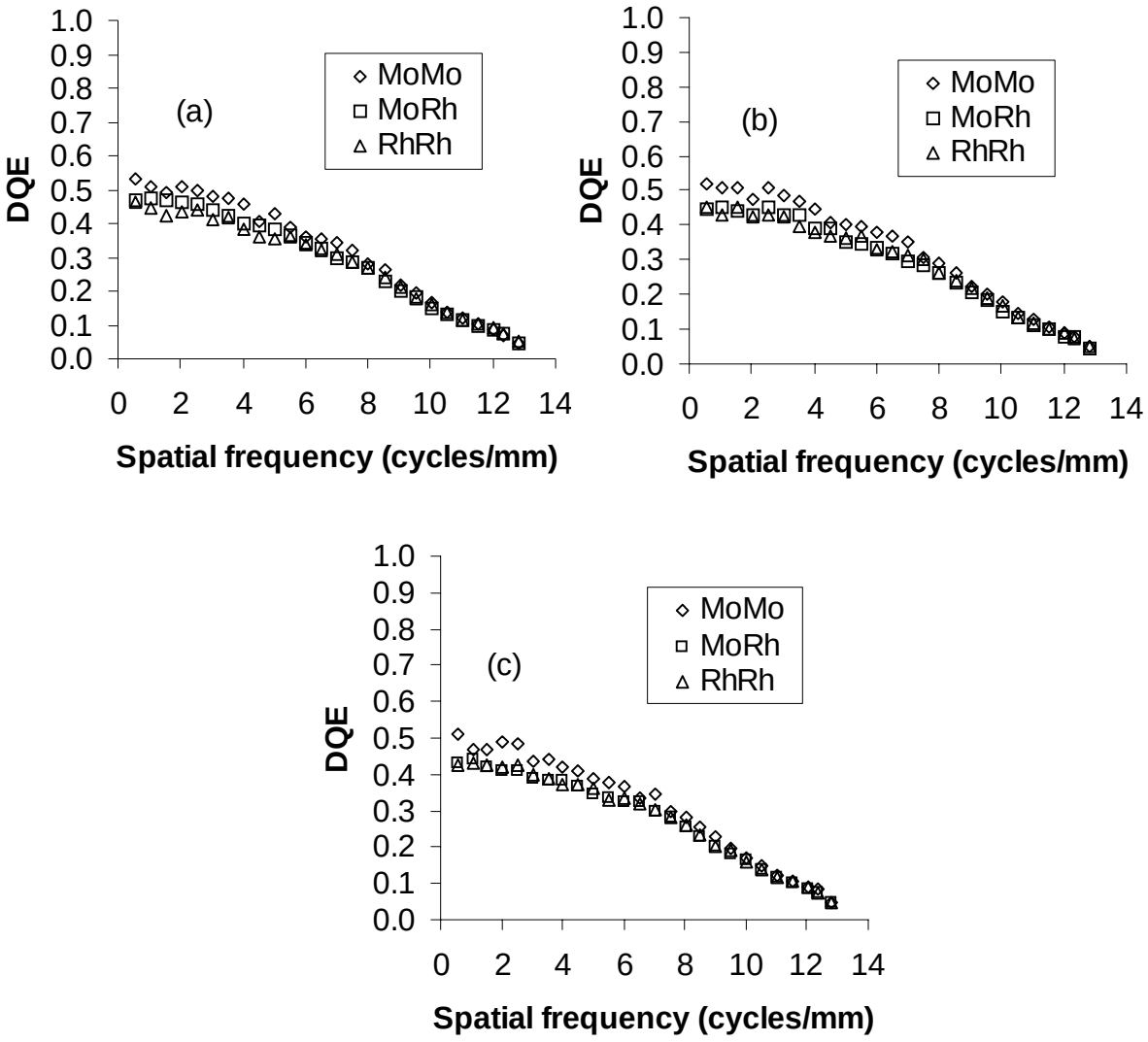

Figure 5.11. *DQE(f) along the parallel read direction with (a) 20 mm, (b) 45 mm, and (c) 57 mm PMMA filtration at 26 kVp, Mo/Mo, 28 kVp, Mo/Rh, and 30 kVp, Rh/Rh measured ~10 mR (Table 5.1). A marginal decrease in* $DQE(f)$ *is observed with Mo/Rh and Rh/Rh compared to Mo/Mo target/filter combinations.*

For a fixed kVp and target/filter, negligible change in $DQE(f)$ was observed with increasing PMMA thickness (Figure 5.12). Overall, the system resulted in zero frequency $DQE(0)$ in the range 0.45 to 0.55 across all kVp, target/filter, and PMMA combinations that were investigated.

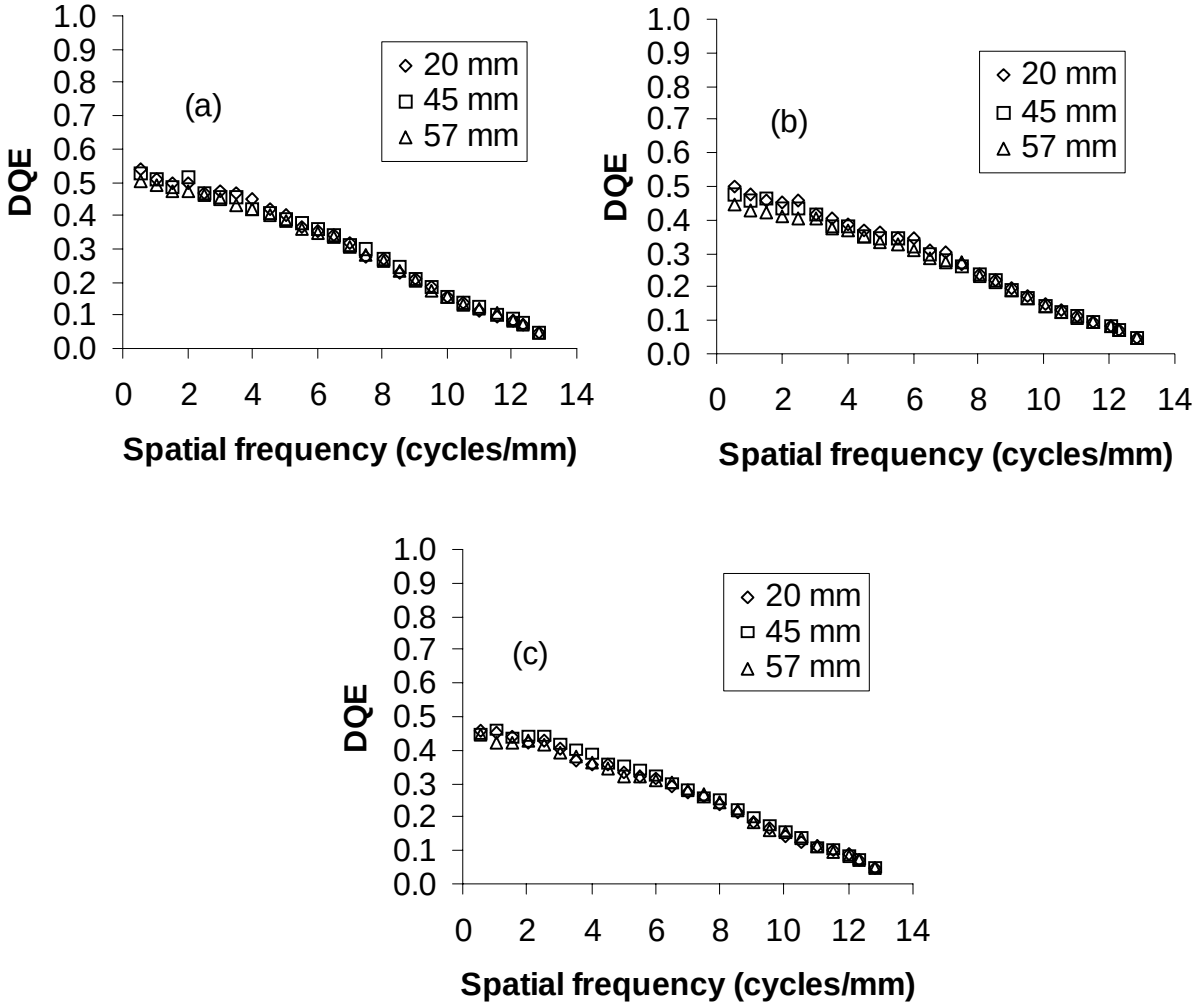

Figure 5.12*. DQE(f) at (a) 26 kVp, Mo/Mo (b) 28 kVp, Mo/Rh, and (c) 30 kVp, Rh/Rh measured ~10 mR (Table 5.1) showing negligible reduction in DQE(f) with increasing PMMA filtration under these x-ray spectral conditions.*

Clinical FFDM System

The presampling $MTF(f)$ measured without any additional PMMA filtration for the Mo/Mo target/filter combination is shown in Figure 5.13a. An MTF of approximately 30% is observed at the Nyquist frequency of 5 cycles/mm. The variation in $DQE(f)$ with target/filter for a given PMMA thickness is illustrated in Figures 5.13b,

5.13c, and 5.13d. For each spectral condition, the zero frequency DQE decreases with increased beam hardening (Table 6). In addition, relatively higher DQE characteristics observed with Mo/Mo compared to Mo/Rh and Rh/Rh.

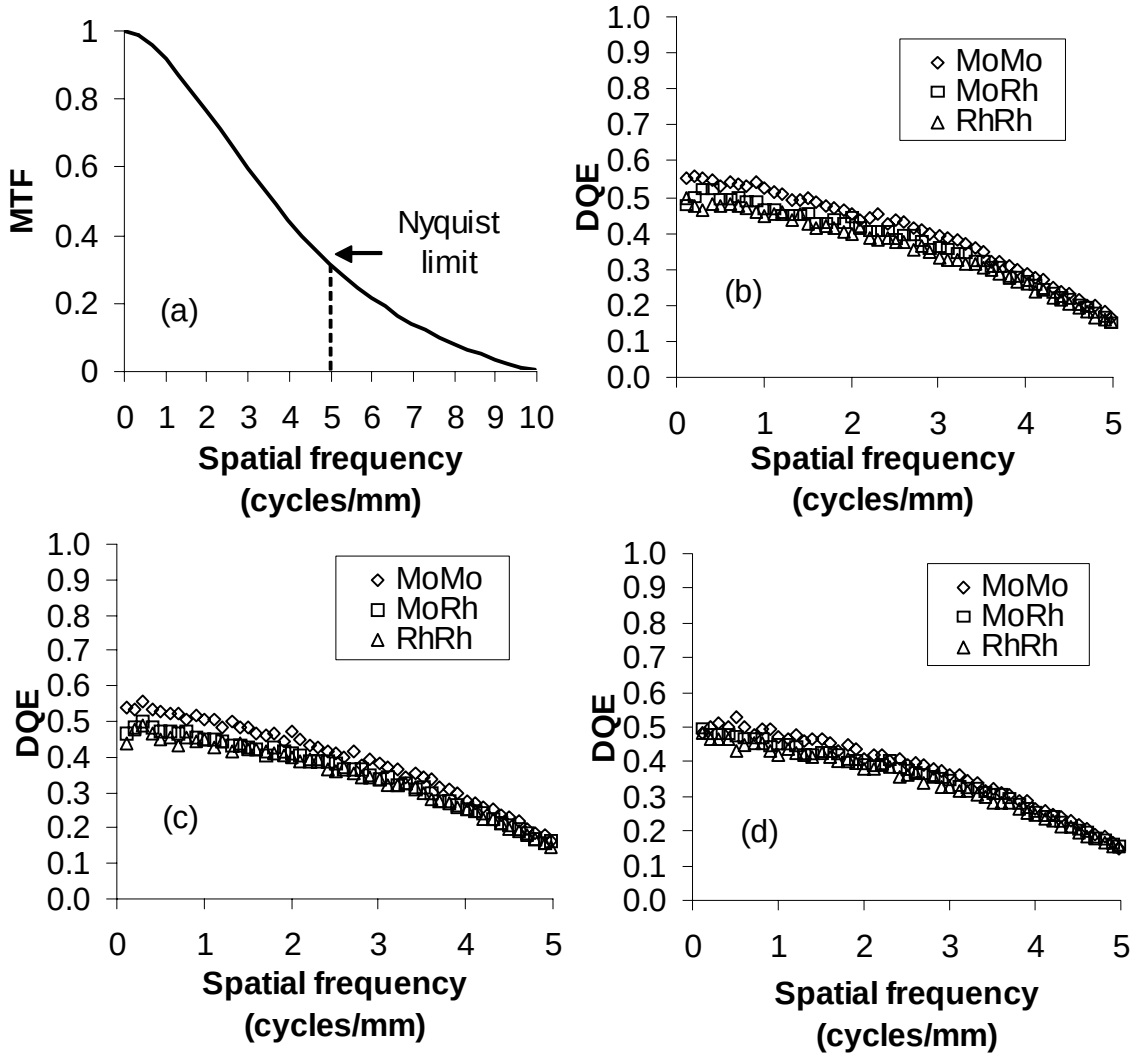

Figure 5.13. *(a) MTF of the clinical FFDM system. DQE(f) characteristics of the FFDM system with (b) 20 mm, (c) 45 mm, and (d) 60 mm PMMA filtration at various target/filter combinations measure ~10 mR (Table 5.2). In general, a marginal decrease in DQE is observed with 28 kVp Mo/Rh and 30 kVp Rh/Rh spectra compared to 26 kVp Mo/Mo.*

Comparison of Prototype and Clinical FFDM System

A comparison of the experimentally measured $MTF(f)$ and $DQE(f)$

characteristics of the prototype and clinical FFDM is shown in Figure 5.14 and 5.15 respectively. It appears that the prototype outperforms the clinical system under the conditions investigated.

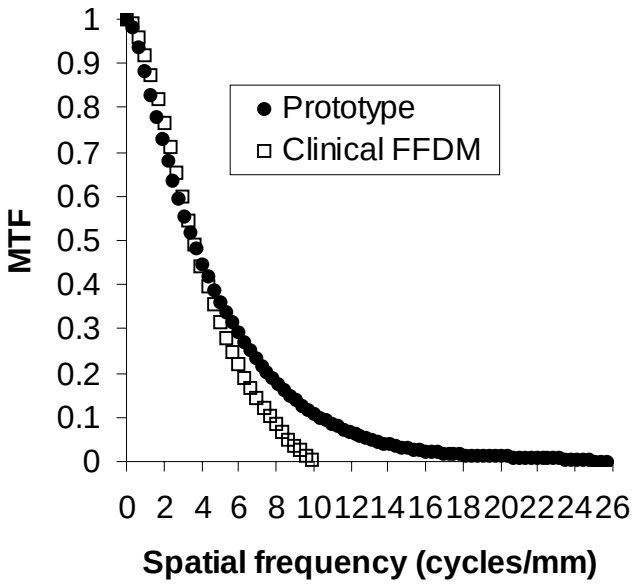

Figure 5.14. *Comparison of MTF(f) characteristics of the prototype and clinical FFDM system.*

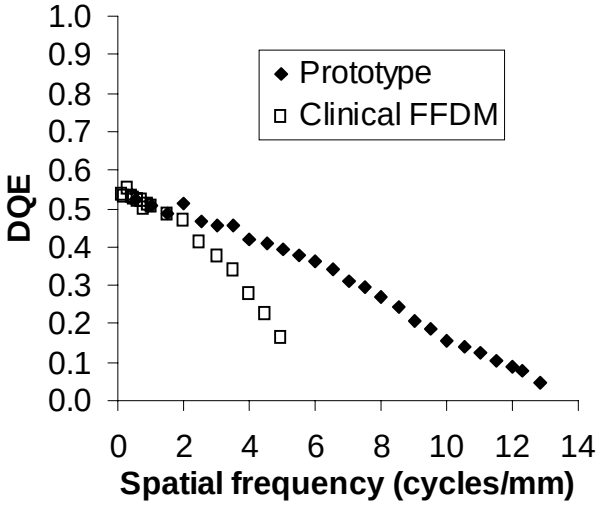

Figure 5.15. *Comparison of MTF(f) characteristics of the prototype and clinical FFDM system at 26 kVp, MoMo with 45 mm PMMA at an entrance exposure ~10 mR.*

Discussion

The prototype CCD and electronics were successfully packaged into an x-ray cassette format that enables easy integration with existing mammography systems. The imager is operable under mammographic conditions without any cooling by liquid circulation. The imager was found to be linear over the typical range of entrance air kerma encountered in mammography under the breast region (Figure 5.3). The prototype imaging system exhibits $MTF(f)$ characteristics comparable to other commercially available digital mammography systems. There was no degradation in $MTF(f)$ with variation in kVp and target-filter (Figure 5.4) as all the energy conditions investigated in this study were below the k-edge of CsI:Tl (Tkaczyk *et al* 2001, Suryanarayanan *et al* 2005). Further, the $MTF(f)$ along orthogonal directions were virtually identical indicating a symmetric frequency response. The nearly identical orthogonal $MTF(f)$ characteristics could be attributed to the unity fill factor as there is no interline structure in the pixels for charge readout. In this study, $MTF(f)$ was measured without any PMMA filtration as the primary focus was to attain the detector $MTF(f)$ while minimizing the effects of scatter. Other investigators have shown the effect of scatter degradation on $MTF(f)$ using an edge test device (Tkaczyk *et al* 2001) under open field conditions but have also demonstrated that such effects can be eliminated by suitable collimation. The slit technique was used in this study as it is preferable for determining high-frequency response (Cunningham and Reid 1992).

The dark 2D NPS shown in Figure 5.5a exhibits fixed pattern noise along the diagonal which can be attributed to the clocking mechanism in the imager for charge transfer and readout. This noise manifests itself in the 2D NPS estimated under both dark

and x-ray acquisition conditions. The NPS along the *u* and *v* axis are virtually identical indicating a symmetric noise power frequency response as shown in Figure 5.5b. The identical $NPS_{normalized}(f)$ along the serial and parallel read directions confirms the symmetric nature of noise in this device (Figure 5.6). Further, it appears that noise contribution by the fixed structural components in the imager are negligible (Figure 5.7). The $NPS_{normalized}(f)$ clearly exhibits exposure dependence as expected (Figure 5.8a). The reduction in $NPS_{normalized}(f)$ is due to the relatively larger increase in average signal with exposure compared to noise. The decrease in $DQE(f)$ at 1.1 mR might be attributed to the increased contribution of dark noise to total noise at such low detector entrance air kerma, especially since the device was operated without any liquid circulation cooling (Figure 5.8b). The long integration time (4 sec) used in this study is likely to have impacted the $DQE(f)$ thereby causing a reduction at ~1 mR. At higher detector entrance air kerma the DQE characteristics are virtually identical implying that the system is x-ray quantum noise limited.

The marginal increase in $NEQ(f)$ at Mo/Rh (28 kVp) and Rh/Rh (30 kVp) target/filter (and kVp) conditions compared to Mo/Mo (26 kVp) (Figure 5.9) could be attributed to the relative increase in the mean energy levels of incident x-ray spectra that lead to an increase in the generation of optical quanta from the scintillator. It is possible that the relative decrease in quantum efficiency is offset by the increased optical quanta generation at higher energy spectral conditions, thereby leading to an increase in $NEQ(f)$. Similar reasoning could be applied to the increase in $NEQ(f)$ with increased PMMA thickness.

The marginal decrease in $DQE(f)$ at Mo/Rh (28 kVp) and Rh/Rh (30 kVp) target/filter (and kVp) conditions compared to Mo/Mo (26 kVp) for a given PMMA thickness condition, may be attributed to the larger increase in the incident number of x-ray quanta per square millimeter relative to the increase in $NEQ(f)$ at the detector entrance air kerma that were studied (Figures 5.10 and 5.11). For the kVp and target/filter conditions that were investigated in this study, increasing PMMA thickness appears to have little effect on the $DQE(f)$ as the increase in $NEQ(f)$ with increasing PMMA thickness was offset by the increase in the incident number of x-ray quanta per square millimeter (Figure 5.12). Overall, for the spectral conditions investigated in this study, the variation in $DQE(f)$ was only marginal. Similar reasoning can be applied to explain the marginal decrease in $DQE(f)$ for the clinical FFDM system (Figure 5.13).

The relatively higher $MTF(f)$ beyond 5 cycles/mm could be attributed to the small pixel size (39 μm) in the prototype CCD compared to the pixel pitch (100 μm) of the a-Si:H FFDM system (Figure 5.14). The higher $DQE(f)$ of the prototype is due to the low noise and small pixel size of the imager (Figure 5.15).

Conclusion

Based on the results of this study, a large-area, high-resolution digital imager with good performance characteristics for mammography appears feasible. The prototype system exhibits $MTF(f)$ and $DQE(f)$ characteristics that is comparable to those of a-Si:H-based clinical digital mammography systems (Vedantham *et al* 2000a, Suryanarayanan *et al* 2004) while providing higher spatial resolution. Although the focus

of this investigation was digital mammography, the imager can be configured for other applications such as small animal imaging that require high-resolution.

CHAPTER 6

PERCEPTUAL ANALYSIS

Introduction

The goal of this part of the study was to compare the perceptual characteristics of the large area prototype and clinical FFDM system. Specifically, the impact of pixel size for two phantom thickness conditions was explored in terms of their contrast-detail (CD) characteristics. Observer independent metrics such as $MTF(f)$ and $DQE(f)$ describe the physical characteristics of a system but they do not provide a description of the visual or perceptual information content of the images. On the other hand, imaging characteristics have been analyzed by investigators using CD techniques (Hall *et al* 1995, Liu *et al* 1997, Wang and Langer 1997, Suryanarayanan *et al* 2002, Suryanarayanan *et al* 2004b) that provide useful insights into the image quality aspects of an imaging system. Contrast-detail performance is also a widely used quality control tool to assess clinical imaging systems. An important factor that motivates CD analysis is that it encompasses the observer or the 'end user' as part of the imaging chain, which is critical if an imaging system is either used or is intended for clinical imaging (Wang and Langer 1997). Contrast-detail methodology can be extremely useful as a precursor study before clinical trials, to determine system performance or compare the performance among different systems. Contrast-detail evaluation may reveal strengths or deficiencies in the system that may need remediation before the onset of the clinical studies.

Methods

Prototype FFDM System

The large area multi-module imager described in Chapter 3 was used for these studies. As described earlier this imaging platform offers pixel configurations of 39 and 78 μm. Both pixel sizes were investigated in this study.

Clinical FFDM System

A clinical full-field digital mammography system (Senographe 2000D, GE Medical Systems, Milwaukee, WI) was used to acquire the images for this study. The system comprises a columnar CsI:Tl scintillator coupled to an amorphous silicon (a-Si:H) photodiode array with a pixel pitch of 100 μm providing a field of view of approximately 19 x 23 cm. The system is capable of operating in three different auto-exposure modes that can be selected based on the preference for either lower dose or higher contrast. The digital mammography system stores images in two formats, raw and processed.

Contrast Detail Phantom

A commercially available contrast-detail phantom (CDMAM 3.2, Fluke Biomedical, Cleveland, OH) was used as the test object in this study. The phantom consists of a thin aluminum base that contains circular gold disks that are logarithmically sized from 0.10 to 3.2 mm in diameter and 0.05 to 1.6 μm in thickness. The disks are arranged in a matrix of squares such that, within each square, one disk is centrally placed and an additional disk is randomly placed at one of the four corners. Within each square, both the central and corner disks have the same diameter and thickness. However, along

a row of squares, the disk thickness is constant while logarithmically varying in diameter and along a column the diameter remains constant while the thickness varies logarithmically. For the purpose of this study additional acrylic was added to bring the total thickness of the phantom to 45 and 58 mm respectively. The main advantage of this phantom is the presence of a randomly spaced corner disk in each square that facilitates alternative forced choice experiments. An x-ray image of the phantom acquired using the prototype is shown in Figure 6.1.

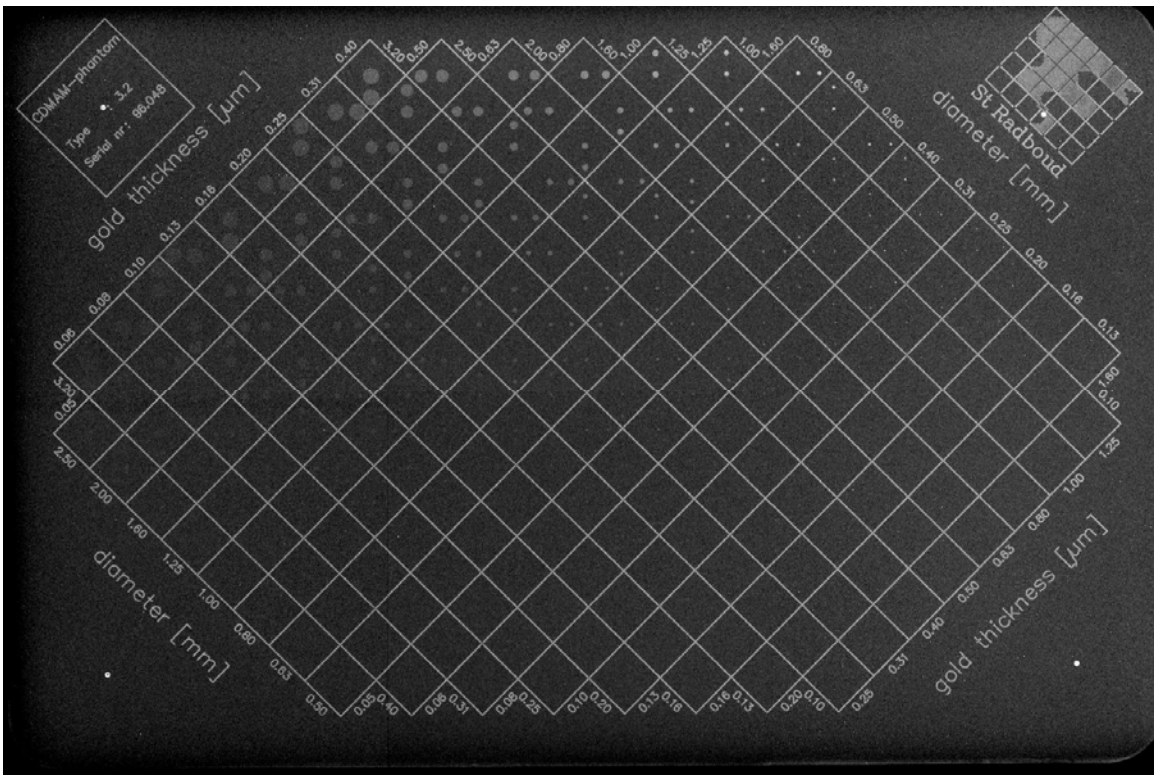

Figure 6.1. *Image of the CDMAM phantom acquired using the large area prototype in the 78 µm pixel mode (developed by Thijssen et al., Department of Radiology, University Medical Centre Nijmegen, the Netherlands).*

Image Acquisition

Images of the CDMAM phantom were first acquired using the clinical FFDM system in the 'contrast-auto' mode for emphasis on image contrast. The phantom was compressed using the compression paddle and the anti-scatter grid was not removed to simulate a clinical situation. The mammography system automatically selected the kVp, mAs, target/filter for both phantom thickness conditions. Under the conditions investigated, the system selected 28 kVp, 145 mAs, Mo/Mo for the 45 mm thick CDMAM phantom, and 31 kVp, 85 mAs, Rh/Rh for the 58 mm thick CDMAM phantom condition. A total of 12 images were acquired for each phantom thickness condition and the raw images were selected for this study. The raw images are automatically bad pixel and flat-field corrected by the clinical system.

The prototype system was integrated with an older mammography unit (Senographe DMR, GE Medical Systems, WI). The source-to-detector distance (SID) of 66 cm was nearly identical to the clinical system. The imager was placed approximately 1 cm below the anti-scatter grid. Before acquiring the images for the study, a calibration was performed to match the exposures between the clinical and lab system. For this purpose, exposures were first measured with the clinical system at the desired tube voltage (28 and 30 kVp) and target/filter (Mo/Mo and Rh/Rh) condition and a specific mAs condition using a calibrated mammographic ionization chamber and exposure meter (MDH 1515, RadCal Corp., Monrovia, CA), and then corrected using the inverse square law to compute the detector entrance exposure. Next, the exposures were measured with the laboratory mammography unit under identical conditions. The ratio of the two exposure values provided the correction factor (CF) that needed to be applied for

acquiring the images using the laboratory mammography unit with the prototype imager. As with the clinical FFDM system, 12 images images were acquired for each phantom thickness (45 and 58 mm) and pixel condition (39 and 78 μm). The images were dark subtracted, flat-field, and bad-pixel corrected. A summary of the technique factors used to acquire the images is shown in Table 6.1.

Table 6.1. *Required mAs for clinical and laboratory mammography units to obtain identical exposures.*

Phantom thickness (mm)	kVp and target/filter	mAs used with clinical system	Computed mAs for lab system	mAs used with lab system
45	28, Mo/Mo	145	211	200
58	30, Rh/Rh	85	113	110

Disk diameters between 0.13 to 0.31 mm were used in this study. For each disk diameter six disk thickness levels were selected to encompass a range that ensured 100% perception of at least one disk for each diameter to a barely perceivable disk.

Image Display

A visual user interface program was developed using Interactive Data Language (IDL 5.5, Research Systems Inc, Boulder, CO). All images were displayed on a DICOM calibrated clinical gray scale flat-panel display system (DOME C5i, Beaverton, OR). The program was designed to display a square ROI from the phantom image in random order. Visual cues were provided at each of the four corners of the square where one of the corners contained the disk (Figure 6.2). The size of the displayed square ROI depended on the imager and pixel size used to acquire the phantom image. Each

displayed ROI was adjusted using an automatic contrast enhancement technique that ensured the best possible contrast. In order to achieve this, histogram analysis was performed to compute the density function of each ROI with reference to the maximum digital value of that ROI image. The digital value corresponding to the maximum number of pixels was computed and the display threshold was set at half this value. A reference image that contained a high contrast version of the disk was displayed above

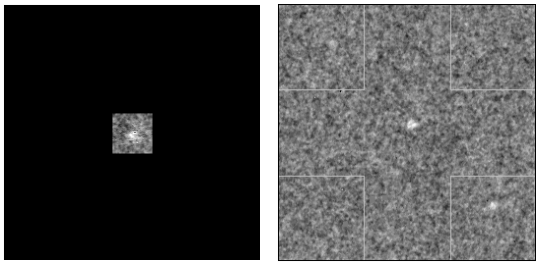

Figure 6.2. *Example of a reference image (left) and a ROI image (right).*

the image ROI in order to provide the observer with information related to the detection task. It was ensured that the diameter of the disk in reference image always matched the diameter of the disk in the image ROI. An automated messaging feature was implemented that indicated to the observer when 25, 50, 75, and 100% of the observation session was completed.

Observer Study

A total of 6 observers that included four board certified radiologists with specialization in mammography and two graduate students with experience in medical imaging participated in this study. The whole study was divided into three parts and each part was divided into two sessions yielding a total of six sessions (two phantom thickness conditions X three pixel sizes). An observer had to do the two sessions on a given day

and each session took about 25-30 minutes. In a given session an observer had to independently view 360 image ROIs (5 disk diameters X 6 disk thickness X 12 image replications). It took three visits per observer to complete the whole study. Before commencing each session, observers were trained till they felt comfortable with the task. All observations were conducted in a darkened room. All observation sessions were randomized between observers to minimize any systematic effects. Since this was a forced choice study, an observer had to indicate the location of the corner disk in one of the four corner squares with a mouse click and was encouraged to arrive at the best estimate in cases where the disk was not perceivable. Observer responses were automatically recorded as a true positive (TP) or false positive (FP) event.

Data Analysis

Based on the recorded responses, for each disk diameter 'percentage correct' or 'proportion correct' values were computed for each observer and disk thickness as the number of correct responses to the total number of image replications (12 in this case). To analyze the 'proportion correct' detection data, a signal detection model was used that hypothesizes a continuous decision variable internal to the observer with Gaussian probability density functions for the presence or absence of the disk(Ohara *et al* 1989, Aufrichtig 1999, Aufrichtig and Xue 2000). The distance between the means of these two overlapping distributions can be represented as $d'=u.\Delta C$ where *'u'* is the slope parameter that needs to be determined and ΔC is the disk contrast (perceived disk thickness). As described by Ohara *et al*., (Ohara *et al* 1989) one can then relate the probability of correct choice, $p(d')$ to the slope parameter *'u'* as

$$p(d') = p(u\Delta C) = \int_{t=-\infty}^{\infty} [\phi(t)]^{M-1} \frac{1}{\sqrt{2\pi}} \exp\left(\frac{-(u\Delta C - t)^2}{2}\right) dt \qquad [1]$$

where $\phi(t)$ is the cumulative Gaussian distribution and the slope parameter *'u'* is estimated using a maximum-likelihood algorithm developed using MATLAB (Version 6, The MathWorks Inc., Natick, MA) (Ohara *et al* 1989). A comprehensive description of the maximum-likelihood technique that was implemented in this investigation has been be provided by Ohara *et al*. This study can be described as having *K* trials defined as *K=N.L* where *N* was the number of repetitions and at *L* disk thickness levels. The derivation of Aufrichtig (Aufrichtig 1999) was used to compute the variance of *'u'* for all *K* trials as

$$\sigma_u^{\,2} = \frac{1}{\sum_{k=1}^{N.L} \frac{1}{\sigma_{u_k}^{\,2}}} = \left(\sum_{k=1}^{N.L} \frac{\left(\frac{dp_k}{dd'_k}\right) \Delta C_k^{\,2}}{p_k(1-p_k)} \right)^{-1} \qquad [2]$$

From the estimated mean value and variance of *'u'*, Eq. 1 can be used to generate percent correct detection curves, p(d') substituting the computed value of *'u'* , the value of M (4 in this case), and the contrast or disk thickness levels.

Contrast Detail Characteristics

The CD characteristics were obtained at the 62.5% detection threshold level as this provided a threshold between chance (25%) and 100% correct detection. For each observer and diameter the perceived disk thickness corresponding to the 62.5% correct detection threshold point in the detection curve was computed. Linear interpolation of adjacent points was performed wherever applicable (Figure 6.3).

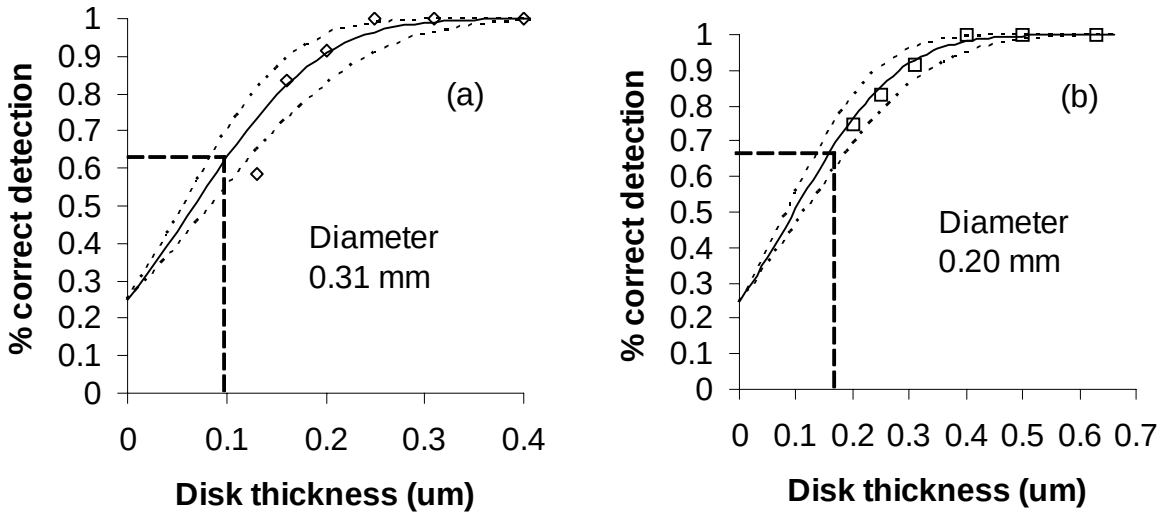

Figure 6.3*. Percent correct detection curves for a single observer for disk diameters of (a) 0.31 and (b) 0.20 mm. Similar detection curves were fitted for all observers and diameters. The perceived disk thickness was computed as the disk thickness corresponding to 62.5% correct detection.*

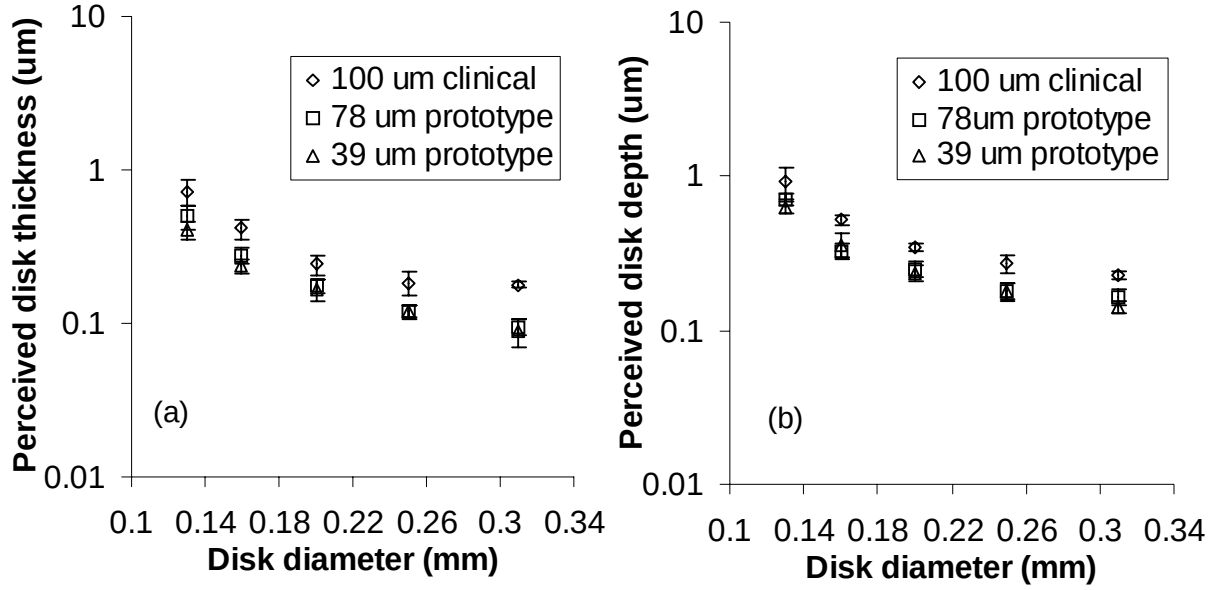

Figure 6.4. *Average CD characteristics of six observers at 62.5% detection threshold. The prototype indicates lower (better) threshold CD characteristics at (a) 45 mm and (b) 58 mm CDMAM phantom thickness conditions compared to the clinical system.*

Contrast-detail characteristics were derived for all diameters, observers, and phantom thickness conditions. Finally, the corresponding contrast detail curves from individual observers were averaged in order to obtain average CD characteristics (Figure 6.4).

Statistical Analysis

Repeated-measures analyses using mixed effects linear models were performed for the perceived disk depth outcome as measured by each of the 6 observers. A saturated model was fit that included the fixed main effects (phantom thickness, pixel size, and diameter), the two-way statistical interaction including thickness by pixel size, thickness by diameter, pixel size by diameter, and the three-way interaction including thickness by pixel size by diameter. The analyses were performed using a means model by using SAS Proc Mixed (version 8, SAS Institute, Cary NC), providing separate estimates of perceived mean disk depth by thickness, pixel size and disk diameter. A compound-symmetry variance-covariance form in observer measurements was assumed for perceived disk depth and robust estimates of the standard errors of parameters were used to perform statistical tests and construct 95% confidence intervals. All statistical tests were 2-sided and unadjusted for multiple comparisons. A P value of 0.05 or less was considered to indicate statistical significance. The analyses were performed by Kirk Easley, Department of Biostatistics, Rollins School of Public Health, Emory University.

Results

The perceived depth in the 45 and 58 mm phantom changed in significantly different ways across pixel size and disk diameter as shown in Tables 6.2 and 6.3 respectively. For the 45 mm thick phantom, the mean perceived disk depth for both 39

and 78 μm pixel sizes were statistically lower (better) compared to the 100 μm pixel at each disk diameter. The mean depth was higher for the 78 μm pixel size compared to the 39 μm pixel at disk diameters of 0.13 and 0.16 mm but not for disk diameters of 0.20, 0.25, and 0.31 mm indicating superior performance of the 39 μm pixel at 0.13 and 0.16 mm disk diameters (Table 6.2).

Table 6.2. Comparison of the effect of pixel size for a phantom thickness of 45 mm at various disk diameters.

	Pixel size (μm)		
Disk diameter (mm)	100 vs. 78	100 vs. 39	78 vs. 39
0.13	P < 0.0001	P < 0.0001	P < 0.0001
0.16	P < 0.0001	P < 0.0001	P < 0.0001
0.20	P = 0.0003	P = 0.0003	P = 0.10
0.25	P < 0.0001	P < 0.0001	P = 0.77
0.31	P < 0.0001	P < 0.0001	P = 0.19

For the 58 mm thick phantom, the mean perceived depth at 39 and 78 μm pixel sizes were statistically lower (better) then the 100 μm pixel. The mean perceived disk depth was higher for the 78 μm pixel size compared to the 39 μm at disk depths 0.13 and 0.16 mm but not at 0.20 and 0.25 mm disk diameters (Table 6.3).

Table 6.3. Comparison of the effect of pixel size for a phantom thickness of 58 mm at various disk diameters.

	Pixel size (μm)		
Disk diameter (mm)	100 vs. 78	100 vs. 39	78 vs. 39
0.13	P = 0.0045	P = 0.0017	P = 0.003
0.16	P < 0.0001	P < 0.0001	P = 0.04
0.20	P < 0.0001	P < 0.0001	P = 0.09
0.25	P < 0.0001	P < 0.0001	P = 0.59
0.31	P < 0.0001	P < 0.0001	P = 0.05

The mean perceived disk depth at 39 μm is statistically lower for the 45 mm phantom compared to the 58 mm phantom at each of the five disk diameters (Table 6.4). A lower

mean perceived disk depth for the 45 mm phantom compared to the 58 mm phantom was also identified for the 78 μm and 100 μm pixel sizes at each disk diameter (Table 6.4).

Table 6.4. Comparison of the effect of phantom thickness (45 vs. 58 mm) for each pixel size at various disk diameters.

	Pixel size (μm)		
Disk diameter (mm)	39	78	100
0.13	$P < 0.0001$	$P < 0.0001$	$P = 0.026$
0.16	$P < 0.0001$	$P = 0.0002$	$P < 0.0001$
0.20	$P < 0.0001$	$P < 0.0001$	$P < 0.0001$
0.25	$P < 0.0001$	$P < 0.0001$	$P < 0.0001$
0.31	$P < 0.0001$	$P < 0.0001$	$P < 0.0001$

Discussion

The use of contrast detail methodology for the evaluation of clinical imaging systems is widely accepted and such psychophysical characterization of imaging systems provides information on the image quality and diagnostic value of a modality. The CD characteristics summarize the information carrying capacity of an imaging system. The methodology described in this study provides a means to quantitatively assess perception data and characterize imaging performance. Other automated methods (Chakraborty and Eckert 1995, Chan *et al* 1996) can also be used in combination with human observers to analyze system performance.

The focus of this study was to obtain a comparison of imaging performance between two systems at various pixel sizes. The alternative forced choice (AFC) method used here provides an effective means of conducting psychophysical measurements (Burgess 1995). In this investigation, the random orientation of signal location is likely to have mitigated observer learning to a great extent compared to more simplistic CD

experiments where the location of the signal is fixed. Forced choice methods also provide an opportunity to evaluate the CD characteristics at multiple detection threshold levels that is not possible with conventional CD experiments.

The superior performance of the prototype system at 39 and 78 μm pixel sizes compared to the clinical FFDM system can be attributed to the better $MTF(f)$ and $DQE(f)$ characteristics of the prototype especially at higher spatial frequencies. The improved performance of the prototype with the 45 and 58 mm thick phantom demonstrates the viability of such imaging architectures for mammography. The lack of any significant difference between the 39 and 78 μm pixel sizes at larger disk diameters could be attributed to the trade off between high spatial resolution, signal, and noise characteristics. However, the significantly better performance of the 39 μm pixel at disk diameters 0.13 and 0.16 mm demonstrates the resolving capability of such small pixel sizes. The degradation in detection and CD characteristics between the 45 and 58 mm thick phantom could be attributed to a combination of lower signal and increased scatter conditions that could potentially impact the visualization of small low contrast objects.

The increase in detection with the high resolution platform is due to its high resolution and low noise characteristics which has a direct bearing on contrast. Analytically, this can be explained based on the relationship between threshold SNR (SNR_T), contrast (ΔC_T), $MTF(u,v)$, and $DQE(u,v)$ as described by various authors (Ohara *et al* 1989, Aufrichtig 1999, Aufrichtig and Xue 2000) as

$$SNR_T = \frac{\Delta C_T \iint \left| S(u,v) MTF(u,v) VRF(u,v) \right|^2 dudv}{\left[\iint \left| S(u,v) MTF^2(u,v) VRF^2(u,v) \right|^2 DQE^{-1}(u,v) \frac{A^2}{\phi} dudv \right]^{1/2}} \quad [3]$$

where, $S(u,v)$ is the object (disk) spectrum, A is the large area signal, ϕ is the x-ray fluence incident on the imager, and $VRF(u,v)$ is the human visual response function. The *'u'* and *'v'* represent 2D spatial frequencies and are related to the 1D spatial frequency, *f* through rotational symmetry. This can be further simplified as (Aufrichtig 1999, Aufrichtig and Xue 2000)

$$SNR_T = \frac{\Delta C_T F_1 \sqrt{\phi}}{A(F_2)^{1/2}} \quad [4]$$

where

$$F_1 = \iint \left| S(u,v) MTF(u,v) VRF(u,v) \right|^2 dudv \quad [5]$$

and $F_2 = \iint \left| S(u,v) MTF^2(u,v) VRF^2(u,v) \right|^2 DQE^{-1}(u,v) \frac{A^2}{\phi} dudv$ [6]

From Eq.4 it is evident that for a given SNR_T, as ratio of F_1/F_2 increases a lower threshold contrast characteristics can be attained implying superior CD characteristics.

Conclusion

The CD characteristics analyzed in this study were encouraging under the conditions investigated in this study. Based on the results of this study, it appears that the potential impact of low noise and high resolution imaging in digital mammography could be useful specifically in the detection and characterization of microcalcifications. The

study also indicates that detection of small objects is impacted by increased object thickness irrespective of pixel size.

CHAPTER 7

THEORETICAL SYSTEM ANALYSIS OF CONTRAST ENHANCED DIGITAL MAMMOGRAPHY

Introduction

Contrast enhanced mammography using injected iodine contrast agents has been explored in the past by other investigators, as discussed in chapter 1, but has yet to be fully investigated and applied to routine clinical use. Preliminary studies are encouraging but are limited to existing mammography systems at energy and x-ray spectral conditions that are relevant to conventional mammography. In this section, the feasibility of high-resolution contrast enhanced mammography with respect to system design and physical characteristics at higher x-ray energies is explored based on the parallel cascaded linear systems framework (Cunningham 1998, Yao and Cunningham 2001, Cunningham *et al* 2002). A simulation based on the parallel cascaded formalism was implemented to understand physical characteristics such as $MTF(f)$ and $DQE(f)$ under these conditions. In addition, an initial understanding of the dose requirements for this imaging application was obtained.

This chapter is organized as follows: (i) the selection and simulation of x-ray spectra for this feasibility study is discussed, (ii) expected dose levels from this type of x-ray spectra are analyzed, (iii) adaptation and implementation of the theoretical parallel cascaded framework is presented, and (iv) key simulation results are presented. The results are analyzed to obtain insights into the physical performance characteristics and feasibility of high-resolution contrast enhanced digital mammography.

Methods

Spectral Simulation

Spectrum simulation for this computation was performed using the software catalogue (SRS-78) provided by the Diagnostic Radiology and Magnetic Resonance Special Interest Group of the Institute of Physics and Engineering in Medicine (Cranley et al 1997). A 49 kVp, W spectrum was chosen based on a recent study for contrast mammography (Ullman *et al* 2005). The half value layer (HVL) at this x-ray spectral condition was measured to be 1.89 mm of Al. In order to estimate the inherent filtration of the tube, the simulated spectrum was filtered by varying different thickness of Al until the HVL of the simulated spectral condition matched the empirically measured HVL.

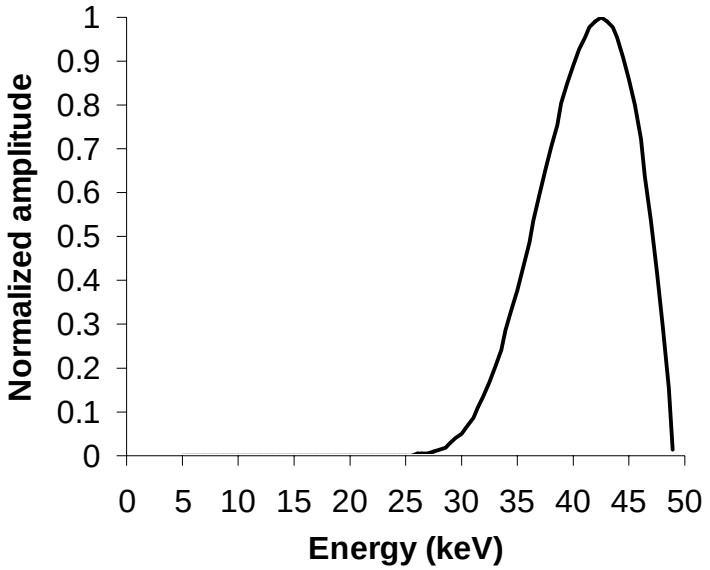

Figure 7.1. *Simulated incident spectrum for contrast mammography at 49 kV with Cu filtration of 0.6 mm.*

This resulted in an inherent tube filtration of 2.93 mm of Al. The incident W spectrum was simulated using the following parameters: 49 kVp, 12^0 anode angle, 2.93 mm inherent Al filtration, and 0.6 mm additional Cu filtration (Figure 7.1).

Preliminary Dose Estimation

In order to estimate the mean glandular dose (x-ray dose imparted to the glandular portion of the breast) for the simulated 49 kVp spectrum, the normalized glandular dose values at different energies, $DgN(E)$ (in mGy/R) for a 5 cm, 50% glandular and 50% adipose breast were fitted using the analytical functions provided by Boone (Boone 2002). The bottom surface of the breast was assumed to be positioned at 65 cm from the focal spot. The photon fluence to exposure conversion factor, $\vartheta(E)$ in mR/photons/mm^2 was computed. Finally, the incident spectrum, $\phi(E)$ was weighted as described by Boone (Boone 2001) to compute the polyenergetic normalized *DgN* coefficient (mGy/R) as

$$pDgN = \frac{\sum_{E_{min}}^{E_{max}} \phi(E)\vartheta(E)DgN(E)}{\sum_{E_{min}}^{E_{max}} \phi(E)\vartheta(E)} \qquad [1]$$

Prototype System Analysis

The modeling described here is similar to the process described in chapter 4 for digital mammography in that the imaging chain is treated as a series of cascading stages. A major difference in this model, compared to the model described for digital mammography, is the inclusion of parallel processes as described in detail by Cunningham (Cunningham 1998, Cunningham *et al* 2002) and Yao (Cunningham 1998,

Yao and Cunningham 2001). As before, at each stage the signal and noise terms were derived for the system described in this study based on the actual physical processes occurring at that stage. The physical stages that were modeled were, x-ray quanta incident on the imager (stage 0), attenuation of x-ray in the scintillator (stage 1), optical quanta generation and emission (stage 2), scintillator optical blurring (stage 3), fiber-optic coupling (stage 4), absorption of optical quanta in the imager (stage 5), pixel presampling MTF (stage 6), noise power spectra aliasing (stage 7), and additive noise (stage 8). The four module, large-area 16 x 16 cm imager with 78 μm pixel was used as the basic platform for simulations in this study.

Imaging Stages

Incident X-ray Quanta (stage 0): The mean number of x-ray quanta per exposure, q_o/X incident on the detector cover plate after traversing through 45 mm of PMMA was computed based on the definition of Roentgen (Johns and Cunningham 1983). Spectral simulations for this computation are as described earlier. The source-to-detector distance was 66 cm and the emission angle was estimated to be about 12^o at the center of the imager. The actual number of quanta that interact with the scintillator was then computed by accounting for transmission, t_f through the detector cover plate and scintillator substrate (Tkaczyk *et al* 2001, Vedantham *et al* 2004a). A transmission of 0.95 was used for the scintillator substrate based on the manufacturer provided data sheet (Hamamatsu 2000). The cover plate transmission, t_f with 45 mm poly-methyl methacrylate (PMMA) filtration was measured to be 0.90 at 49 kVp W spectra with 0.6 mm Cu filtration. The post PMMA incident x-ray spectrum is shown in Figure 7.2.

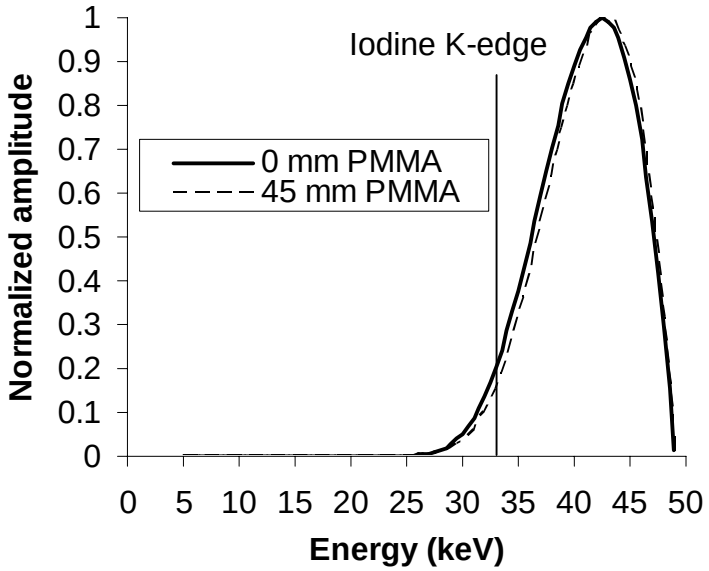

Figure 7.2. *Comparison of pre and post normalized PMMA x-ray spectra at 49 kVp, 0.6 mm Cu, and additional PMMA filtration. Only a marginal decrease in low energy counts is observed.*

Quantum Efficiency (stage 1): As before, the energy dependent QE was computed as

$$g_1(E) = 1 - exp\left[-\left(\mu(E)X_t\right)\right] \quad [2]$$

and the mean QE, $\bar{g}_1$ was computed as

$$\bar{g}_1 = \int g_1(E) q_{rel}(E)\, dE \quad [3]$$

The surface density, ρ_s (mg/cm^2) of the scintillator sample was estimated from manufacturer (Hamamatsu Corp., Bridgewater, NJ) provided data for other similar samples. This was used to compute the packing fraction of the scintillator and the resulting mean QE.

Generation and Emission of Optical Quanta (stage 2): This is the point of demarcation between the previously described model for digital mammography and this model. The

energies in the incident spectra that are above the K-edge of iodine in CsI:Tl causes K-fluorescence to occur in the scintillator.

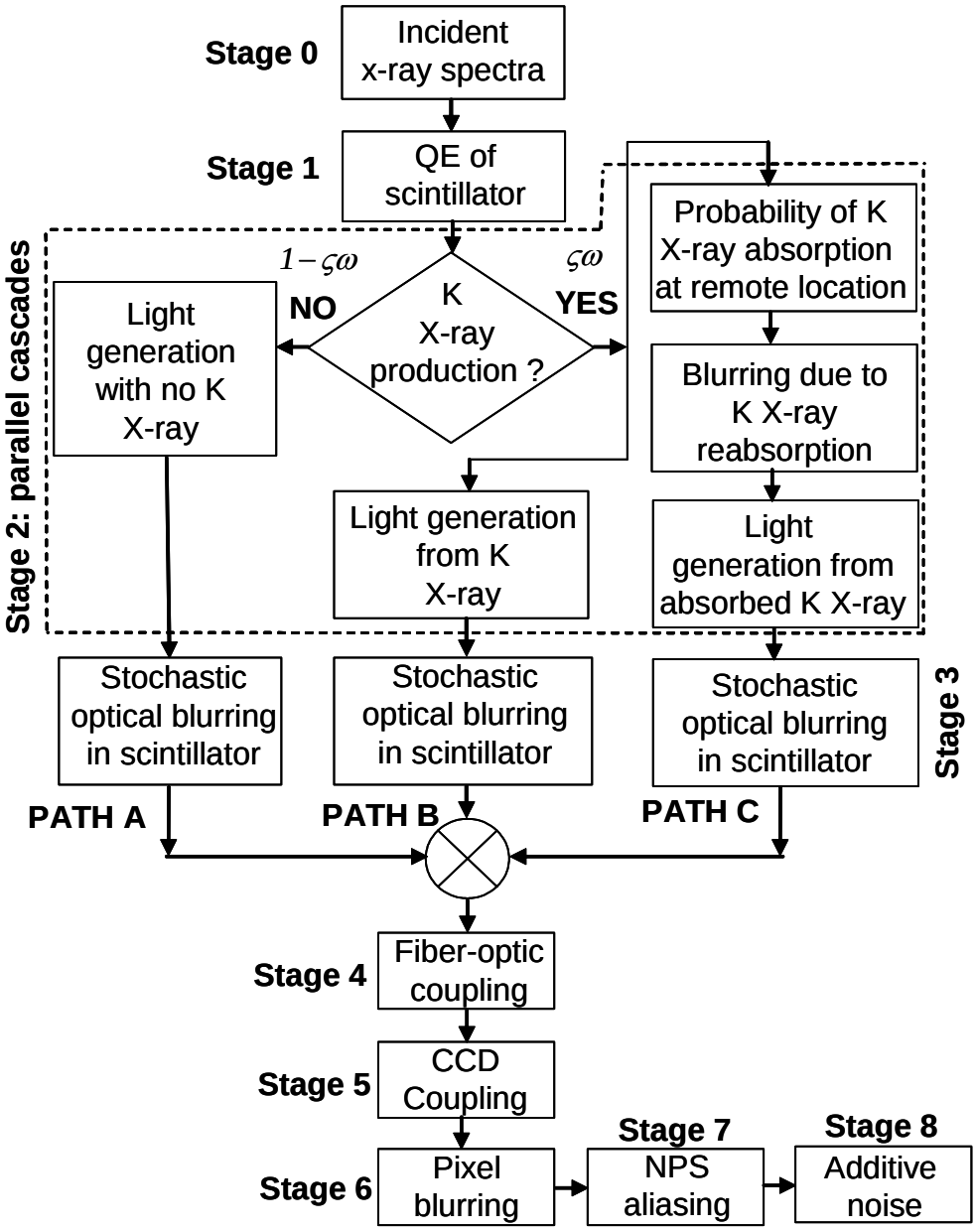

Figure 7.3*. Complete description of the imaging chain that includes the parallel cascaded process (stage 3).*

The absorption of K-x-rays induces spatial blurring resulting in spatial correlation between the primary interaction site and the re-absorption site which results in parallel pathways for signal and noise propagation. This spatial correlation has been shown to exist by Metz and Vyborny (Metz and Vyborny 1983). Very detailed descriptions of the theory of parallel cascades have been provided by Cunningham (Cunningham 1998, Cunningham *et al* 2002) and Yao (Yao and Cunningham 2001). Other investigators have applied the theory for various x-ray imaging detectors (Vedantham *et al* 2004a). A depiction of the complete process is shown in Figure 7.3. Based on the works of Cunningham (Cunningham 1998, Cunningham *et al* 2002) and Yao (Yao and Cunningham 2001), path A corresponds to the case when light emission is produced due to a non-K-fluorescent x-ray, path B corresponds to the case when light emission occurs when a K-fluorescent x-ray is produced and absorbed at the same location, and path C corresponds to the case of light emission when a K-fluorescent x-ray is produced, but absorbed remotely. Assuming a Poisson process, the NPS at the end of Stage 2 along each path can be described using the transfer relationship described by Rabbani *et al*. (Rabbani *et al* 1987) which has been applied in the past for an angiography system (Vedantham *et al* 2004a) as

$$W_2^A = t_f \bar{q}_0 \bar{g}_1 (1 - \varsigma\omega)\bar{m}_A(\bar{m}_A + 1) \quad [4]$$

$$W_2^B = t_f \bar{q}_0 \bar{g}_1 \varsigma\omega\bar{m}_B(\bar{m}_B + 1) \quad [5]$$

$$W_2^C = t_f \bar{q}_0 \bar{g}_1 \varsigma\omega f_K \bar{m}_c(\bar{m}_c + 1) \quad [6]$$

and the signal at the output of each path at the end of stage 2 will be

$$\phi_2^A = t_f \bar{q}_0 \bar{g}_1 (1 - \varsigma\omega)\bar{m}_A \quad [7]$$

$$\phi_2^B = t_f \bar{q}_0 \bar{g}_1 \varsigma \omega \bar{m}_B \quad [8]$$

$$\phi_2^C = t_f \bar{q}_0 \bar{g}_1 \varsigma \omega f_K T_K(u,v) \bar{m}_c \quad [9]$$

where , ς is the probability of K-shell interaction, ω is the fluorescence yield, f_K is the K-absorption probability, and m_A, m_B, and m_C are the mean gains along paths A,B, and C respectively. The term $m_A(m_A + 1)$ can be approximated to m_A^2 for large values of m_A. Similar rationale applies for the gains along B and C paths. The value of f_K was determined using the analytical model of Chan and Doi (Chan and Doi 1983). The stochastic blur of K-fluorescent x-rays, $T_K(u,v)$ was determined based on the description provided by Metz and Vyborny (Metz and Vyborny 1983). The point spread function of the absorption of K-fluorescence was determined by Monte Carlo simulations (Jacques 1998). The values of ς and ω were taken to be 0.83 and 0.87 respectively, based on the fractional weights of Cs and I in CsI:Tl (Ganguly *et al* 2003).

In order to compute the mean gains, m_A, m_B, and m_C along each path, the CsI:Tl scintillator was modeled as consisting of a number of fractional layers of thickness Δt as described in quantum gain section in chapter 4 for digital mammography. For a layer at a distance, Z from the output surface of the phosphor such that the output surface is coupled to a fiber optic plate, the incident x-rays are attenuated by $exp^{-\mu(t-z)}$ before reaching the layer of interest, where a fraction of the x-rays get converted into optical quanta. As before, if $W_{CsI:Tl}$ is the optical photons per keV and E_K the K-edge of CsI:Tl , then the gains can be computed as (Vedantham *et al* 2004a)

$$\overline{m}_A = \frac{\int q_0(E)\left[\int_{z=t}^{0} exp^{-\mu(t-z)}\left(1-exp^{-\mu\Delta t}\right)\eta_{esc}(z)(1-\varsigma\omega)EW_{CsI:Tl}\,dz\right]dE}{\int q_0(E)g_1(E)(1-\varsigma\omega)dE} \quad [10]$$

$$\overline{m}_B = \frac{\int q_0(E)\left[\int_{z=t}^{0} exp^{-\mu(t-z)}\left(1-exp^{-\mu\Delta t}\right)\eta_{esc}(z)\varsigma\omega(E-E_K)W_{CsI:Tl}\,dz\right]dE}{\int q_0(E)g_1(E)\varsigma\omega dE} \quad [11]$$

$$\overline{m}_B = \frac{\int q_0(E)\left[\int_{z=t}^{0} exp^{-\mu(t-z)}\left(1-exp^{-\mu\Delta t}\right)\eta_{esc}(z)\varsigma\omega f_K E_K W_{CsI:Tl}\,dz\right]dE}{\int q_0(E)g_1(E)\varsigma\omega f_K dE} \quad [12]$$

The escape efficiency, $\eta_{esc}(z)$ was determined using the results of Hillen (Hillen *et al* 1991), as described in chapter 4 for digital mammography. The noise from paths B and C are spatially correlated (Cunningham 1998, Yao and Cunningham 2001, Cunningham *et al* 2002) and can be expressed as (Vedantham *et al* 2004a)

$$2W_2^{BC} = 2t_f\overline{q}_0\overline{g}_1\varsigma\omega f_K\overline{m}_B\overline{m}_C T_K(u,v) \quad [13]$$

The summed mean signal at the output of this stage is

$$\phi_2 = t_f\overline{q}_0\overline{g}_1\overline{g}_2 \quad [14]$$

where, the mean gain of this stage, $\overline{g}_2$ is given by

$$\overline{g}_2 = (1-\varsigma\omega)\overline{m}_A + \varsigma\omega\overline{m}_B + \varsigma\omega f_K\overline{m}_C \quad [15]$$

The noise at the output of this stage is

$$W_2(u,v) = t_f\overline{q}_0\overline{g}_1\left[(1-\varsigma\omega)\overline{m}_A^2 + \varsigma\omega\overline{m}_B^2 + \varsigma\omega f_K\overline{m}_C^2 + \overline{g}_2 + 2\varsigma\omega f_K\overline{m}_B\overline{m}_C T_K(u,v)\right] \quad [16]$$

Scintillator Blur (stage 3): The scintillator optical blur, $T_3(u,v)$ was empirically estimated by first measuring the presampling $MTF(f)$ below the K-edge of CsI:Tl and then deconvolving the pixel aperture response. As in the case of digital mammography, the resulting optical blur was fitted to a function of the form $1/1+Hf+Hf^2$ where H is the

fit-parameter and f is the spatial frequency (Vedantham *et al* 2004a). The mean signal at the output of this stage remains the same as the previous stage but the noise changes, based on the NPS transfer relationship (Rabbani *et al* 1987) as

$$W_3(u,v)=t_f\bar{q}_0\bar{g}_1\left[A(u,v)T_3^2(u,v)+\bar{g}_2\right] \quad [16]$$

where,

$$A(u,v)=(1-\varsigma\omega)\bar{m}_A^2+\varsigma\omega\bar{m}_B^2+\varsigma\omega f_K\bar{m}_C^2+\bar{g}_2+2\varsigma\omega f_K\bar{m}_B\bar{m}_C T_K(u,v) \quad [17]$$

Optical Coupling and Absorption Efficiencies (stages 4 and 5): The value of optical coupling efficiency, $\bar{g}_4$ was determined using the technique described by Hejazi and Trauernicht (1997) by taking into account fiber transmission, Fresnel reflection losses, and fiber core fill factor (Hejazi and Trauernicht 1997) and was estimated to be about 0.40. The fiber related parameters were obtained from the data provided by the manufacturer (Schott North America Inc, Southbridge, MA). The QE of the imaging device, $\bar{g}_5$ was determined from the manufacturer (Fairchild Imaging Inc, Milpitas, CA) provided information and was estimated to be ~0.5 corresponding to the emission spectrum of CsI:Tl. The mean signal at the end of this stage was determined as

$$\phi_5 = t_f\bar{q}_0\bar{g}_1\bar{g}_2\bar{g}_4\bar{g}_5 \quad [18]$$

while the frequency dependent signal was computed as

$$\phi_5(u,v) = t_f\bar{q}_0\bar{g}_1\bar{g}_4\bar{g}_5 T_3(u,v)g_2(u,v) \quad [19]$$

where,

$$\bar{g}_2(u,v)=(1-\varsigma\omega)\bar{m}_A+\varsigma\omega\bar{m}_B+\varsigma\omega f_K T_K(u,v)\bar{m}_C \quad [20]$$

Based on the transfer relationship (Rabbani *et al* 1987), the noise was computed as

$$W_5(u,v)=t_f\bar{q}_0\bar{g}_1\bar{g}_2\bar{g}_4\bar{g}_5\left[\bar{g}_4\bar{g}_5 A(u,v)T_3^2(u,v)+\bar{g}_2\right] \quad [21]$$

Pixel Presampling MTF (stage 6): The pixel presampling MTF was approximated as the sinc response of the pixel, $T_6(u,v)$ with pixel dimensions a_x and a_y in the x and y directions. A fill factor, f_f of 0.513 (Vedantham *et al* 2004a) was used based on the pixel geometry of the imager modeled in this study except where specified. The mean signal at the output of this stage was determined as

$$\phi_6(u,v) = \phi_5(u,v) a_x a_y f_f T_6(u,v) \quad [22]$$

and the noise transfer based on the transfer relationship (Rabbani *et al* 1987) was determined as

$$W_6(u,v) = W_5(u,v) a_x^2 a_y^2 f_f^2 T_6^2(u,v) \quad [23]$$

Noise Power Spectra Aliasing and Additive noise (stages 7 and 8): As described before for digital mammography, in order to account for this effect, noise aliasing was introduced (Siewerdsen 1998, Siewerdsen *et al* 1998) as

$$W_7(u,v) = W_6(u,v) ** III(u,v) \quad [24]$$

where, $III(u,v)$ is the Fourier transform of an array of δ functions used to represent the pixel matrix.

Table 7.1. Estimates of input parameters used for contrast enhanced mammography

Photons/keV, $W_{CsI:Tl}$	55
Scintillator surface density (mg/cm^2), ρ_s	48
Fiber optic coupling efficiency, g_4	0.40
Quantum efficiency, g_5	0.5
Gain (e-/DU)	10.6
Pixel fill-factor	0.513
Cover transmission and CsI:Tl substrate transmission @41 keV, t_f	0.9 x 0.95
Probability of K-shell interaction, ς	0.83
Fluorescence yield, ω	0.87

The total additive electronic noise was empirically estimated from dark image acquisitions and added to provide the NPS at the output of the final stage. The values of the parameters used in the model are listed in Table 7.1.

Preliminary Contrast Computation

In order to obtain insights into the potential contrast characteristics of contrast enhanced mammography compared to digital mammography, a first order contrast computation was performed. A 5 cm thick, 50% glandular breast was assumed to contain a 2 mm thick lesion. A 26 kVp, Mo/Mo incident spectra with a mean energy ~16 keV was simulated for digital mammography, while the 49 kVp incident spectra shown in Figure 7.1 was used for contrast enhanced mammography (mean energy ~41 keV). The corresponding attenuation coefficients of breast tissue (Hammerstein *et al* 1979), duct carcinoma (Johns and Yaffe 1987), and iodine(Hubbell and Seltzer 1997) were obtained at the mean energy levels of each spectral condition.

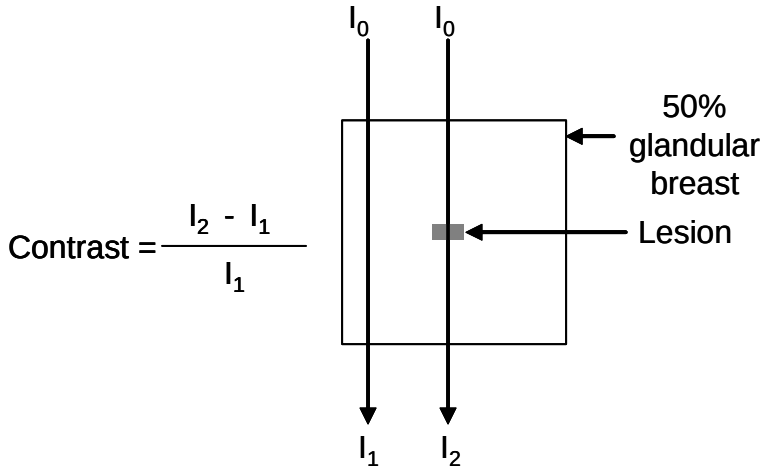

Figure 7.4*. Illustration of contrast computation.*

For the case of contrast enhanced mammography, the weight fraction of carcinoma and iodine was used to compute the mass attenuation coefficient of the lesion for different concentrations of iodine from which the linear attenuation coefficient was calculated. Contrast was then computed as the ratio of the difference in the attenuation between the background and lesion (carcinoma) to the background attenuation. An illustration of the geometry is shown in Figure 7.4.

Results

The mean energy of the incident x-ray spectrum (Figure 7.1) and the spectrum past 45 mm of PMMA (Figure 7.2) were 41 and 41.3 keV. As evident from Figures 7.1 and 7.2 most of the energy components in the incident spectra are above the K-edge of iodine (33.16 keV). Based on the simulated spectra, the computed *pDgN* value for the 5 cm, 50% glandular breast was 8.71 mGy/R.

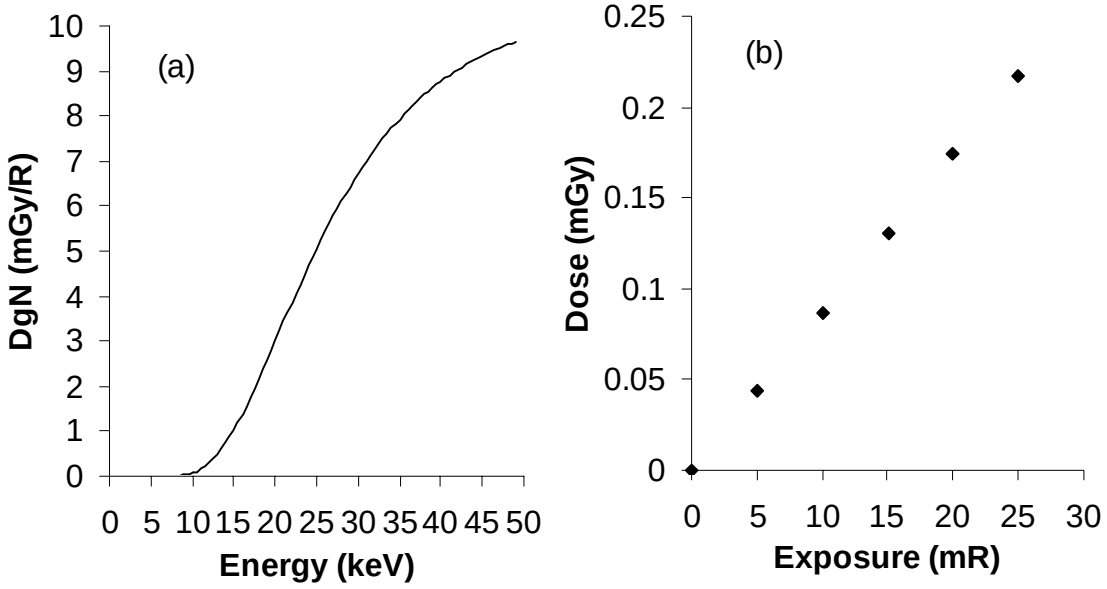

Figure 7.5. *(a) Computed DgN(E) coefficients and (b) dose for a 5 cm, 50% glandular breast based on the x-ray spectra shown in Figure 7.1.*

The air kerma for the incident spectra was 0.95 μGy/mAs at 75 cm from the focal spot which corresponded to 1.49 μGy/mAs at 60 cm (breast entrance). The computed $DgN(E)$ and dose for a 5 cm, 50% glandular breast is shown in Figure 7.5. All the simulated $MTF(f)$ and $DQE(f)$ results reported in this section are for 49Vp, W target, inherent Al filtration of 2.93 mm, Cu filtration of 0.6 mm, 78 μm pixel, and the parameters shown in Table 7.1 unless otherwise stated. A detector entrance exposure of 0.53 mR and 45 mm PMMA was used for all $DQE(f)$ simulations. The simulated $MTF(f)$ characteristics for various CsI:Tl scintillator thickness conditions is shown in Figure 7.6a and the $MTF(f)$ characteristics for various pixel sizes for a 150 μm thick CsI:Tl scintillator is shown in Figure 7.6b. As expected, an increase in Cs:Tl thickness or pixel size causes a drop in $MTF(f)$. The predicted $MTF(f)$ (normalized signal at the end of stage 6, Eq. 22) for a 150 μm thick CsI:Tl scintillator shows good agreement with experimentally measured $MTF(f)$.

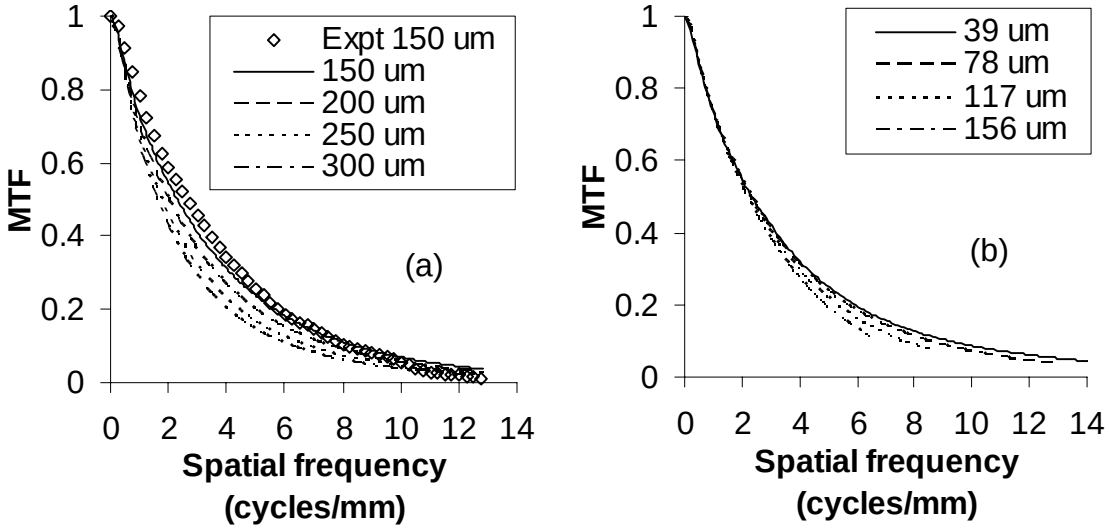

Figure 7.6. *(a) Effect of scintillator thickness and (b) pixel size on the MTF(f) characteristics of the prototype imager.*

However, the degradation in $MTF(f)$ with increasing pixel size is less pronounced. The $DQE(f)$ characteristics exhibit an increasing trend with increasing CsI:Tl scintillator thickness for a pixel size of 78 μm (Figure 7.7a). The increase is more pronounced at lower spatial frequencies compared to the frequencies closer to the Nyquist limit.

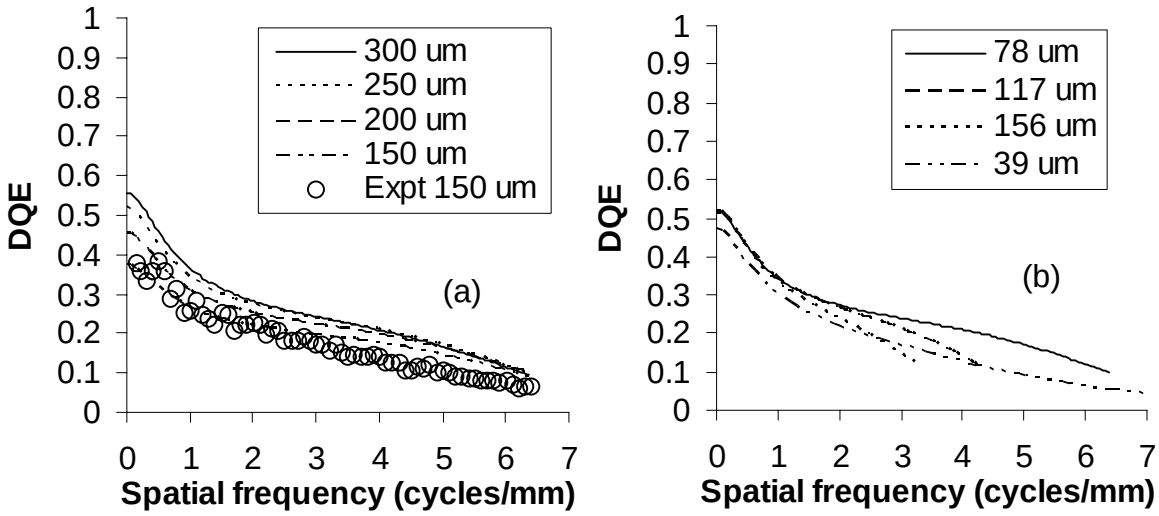

Figure 7. 7. *(a) Effect of scintillator thickness and (b) pixel size on the DQE(f) characteristics of the prototype imager.*

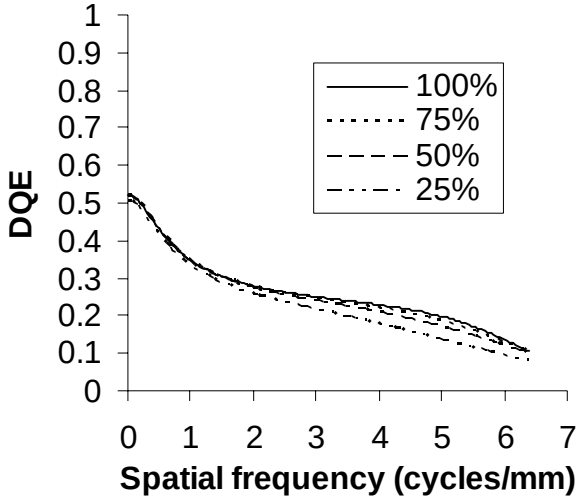

Figure 7.8. *Effect of pixel fill factor on the DQE(f) characteristics of the prototype imager.*

There appears to be good agreement between the theoretically predicted and empirically measured $DQE(f)$ for a 150 μm thick scintillator. The variation in $DQE(f)$ with pixel size for a 250 μm thick CsI:Tl scintillator exhibits a nearly identical DQE(0) for all pixel sizes except 39 μm (Figure 7.7b). However, a faster roll-off in $DQE(f)$ is observed with increasing pixel size. A constant additive noise was assumed for this computation on the basis that change in additive noise with pixel size is marginal compared to quantum noise. The effect of pixel fill-factor on the $DQE(f)$ characteristics of the imager is shown in Figure 7.8 for a 250 μm thick CsI:Tl scintillator. A noticeable impact on the $DQE(f)$ in the mid-to-high spatial frequency range is observed.

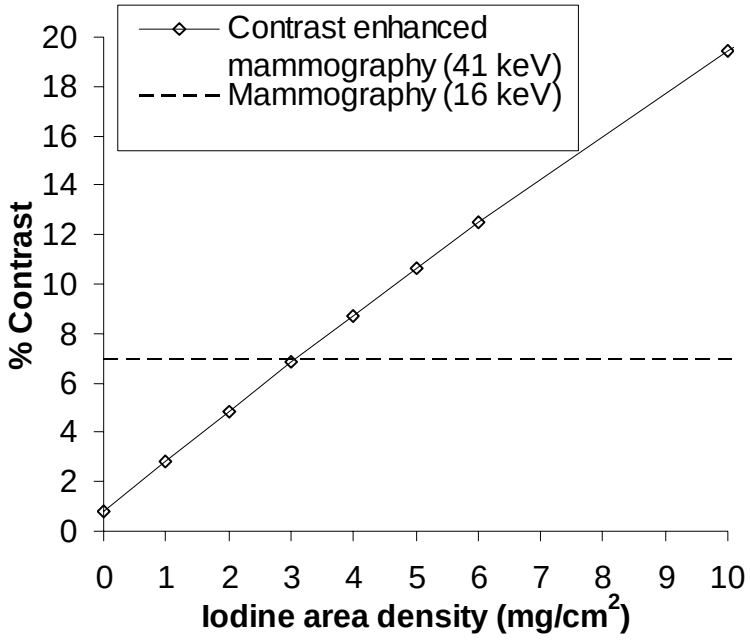

Figure 7.9. *Contrast characteristics of a 2 mm thick lesion in a 5 cm, 50% glandular breast for (a) digital mammography at 16 keV incident energy and (b) contrast enhanced mammography at 41 keV. Iodine area concentration is only relevant to contrast enhanced mammography.*

The computed contrast characteristics for the 0.2 cm thick lesion indicates superior performance of contrast enhanced mammography beyond an iodine uptake area concentration of 3 mg/cm^2 under the conditions investigated (Figure 7.9).

Discussion

The x-ray spectrum used in this study appears to be suitable for contrast enhanced mammography. The attenuation by breast equivalent tissue is minimal (Figure 7.2) and most of the energies are above the K-edge of iodine ensuring substantial absorption by iodine. Further, the dose imparted to the breast at these energy levels are much smaller than the dose levels encountered in routine mammographic screening. The FDA mandates a glandular dose limit of 3 mGy (300 mRad) for a standard cranio-caudal view of a breast with thickness 4.5 cm (FDA 1992). A recent phantom-based survey of 337 FFDM units indicated an average dose was 151.8 mRad (Mourad 2005). It is encouraging to note that the dose imparted to an average glandular breast in contrast enhanced mammography under the conditions investigated in this study could potentially be lower than 0.5 mGy (50 mRad) for the entire examination (Figure 7.5) and much lower dose levels could be achieved by improving detector technologies.

An increase in scintillator thickness appears to have a more predominant degradation effect on system resolution compared to increase in pixel pitch as evident from Figures 7.6a and 7.6b. This could be attributed to the greater spatial spreading of optical photons compared to the loss in resolution due to the pixel aperture response. Further, unlike digital mammography, very small pixel sizes may not be required in contrast enhanced digital mammography as the primary focus would be to image

mass-like lesions with associated angiogenesis. Further, the SNR is expected to be high due to the contrast characteristics of lesions after contrast agent uptake.

The $DQE(f)$ results suggest an increase in $DQE(0)$ with an increase in scintillator thickness which could be directly attributed to the increase in QE (Figure 7.7a). The decrease in $DQE(f)$ at 39 μm is likely due to the relative increase in additive noise compared to the quantum noise of the imaging system. Further, the signal level is reduced for this pixel size which results in a lower $DQE(f)$. However, there is negligible impact on $DQE(0)$ in the pixel range 78-156 μm due to the system being x-ray quantum noise limited at these configurations. The influence of the pixel aperture response is magnified in $DQE(f)$ by its square which causes a reduction in $DQE(f)$ with increasing pixel size (Figure 7.7b). Pixel fill-factor influences the signal collection efficiency of the pixel in the imager as it impacts the active area of the pixel. It also impacts the frequency response of the active pixel dimension (Figure 7.8).

The evaluation of percent contrast characteristics indicate that it might be possible to obtain higher lesion contrast levels at iodine concentration levels beyond 3 mg/cm^2. Recent studies by other investigators suggest similar iodine concentration levels (Skarpathiotakis *et al* 2002, Jong *et al* 2003). It is possible to further reduce concentration of the contrast agent and achieve adequate lesion contrast levels by using lower energy x-ray spectrum (e.g. 45 kVp). Studies indicate that dose consequences in the 41-55 kVp W spectral range are minimal relative to the SNR (Ullman *et al* 2005). However, the number of image frames required for a complete exam and the efficiencies of the detector will ultimately determine the dose to the patient.

The cascaded modeling framework (Jee *et al* 2003) provides a convenient approach to analyze imaging systems by changing a multitude of parameters. Although the parameters used in the model were mostly based on published values or reasonable assumptions, they may not be exact. Further, even published specifications on specific devices may change without notice from the manufacturer. These models are instructive however the interpretation of the results must be used with caution. If the results of the model are in reasonable agreement with the experimental measurements, this does not prove that the model is perfect but does provide a reasonable means to study trends and effects. Important insights on the use of these models and the selection of model input parameters was recently provided by Jee *et al.* (Jee *et al* 2003). The dose calculations performed in this investigation are based on the results of simulations and assumptions of a homogenous breast. These results should be used as a benchmark for comparison purposes and a more robust estimation of dose requirements and performance must be made through clinical investigations (Jong *et al* 2003, Lewin *et al* 2003).

Conclusion

The results of this study demonstrate the feasibility of high resolution contrast enhanced mammography at higher x-ray energy levels and low radiation dose. Based on the conditions investigated in this study, it appears that high contrast characteristics could be achieved at lower dose levels compared to digital mammography. Comprehensive clinical studies are required to determine the nature and types of contrast agents, kinetics, image frames, and dose levels for this application.

CHAPTER 8

EXPERIMENTAL SYSTEM ANALYSIS OF CONTRAST ENHANCED DIGITAL MAMMOGRAPHY

Introduction

In this section, the empirical performance characterization of the prototype high-resolution imager for contrast enhanced mammography is presented. The details of the imaging platform architecture are described in detail in chapter 3. As stated earlier, this imager was modified from a previous design for fluoroscopic applications (Vedantham *et al* 2004b). Nevertheless, the imaging platform was used to obtain insights into the performance of similar architectures for contrast enhanced mammography. As before, metrics such as linearity, $MTF(f)$, $NPS(f)$, and $DQE(f)$ were studied.

This chapter is organized as follows: first, the methods used to measure the exposure to the breast and the imager is described. Next, the measurements of physical parameters such as linearity, $MTF(f)$, $NPS(f)$, and $DQE(f)$ are presented. Finally, the results are discussed and the viability for clinical applications is discussed.

Methods

The x-ray system consisted of an x-ray generator (Indico 100, CPI Inc., Canada) capable of both radiographic and fluoroscopic exposures. The generator was coupled to an x-ray tube (B-150 housing with A-192 tube insert, Varian Medical System, Salt Lake City, UT) with 0.6 and 1.2 mm nominal focal spot sizes and an anode angle of 12^0. All measurements reported in this section were performed at in the radiographic mode with the 0.6 mm focal spot. A tube voltage of 49 kVp with 0.6 mm added Cu filtration was

used throughout the study. An added PMMA thickness of 45 mm was used as before to mimic the attenuation by the breast. This was mounted on a rack situated just below the tube housing in order to minimize scatter effects. Further, the tube housing had an XY translatable collimator which was adjusted to cover the area of an 8 x 8 cm CCD module.

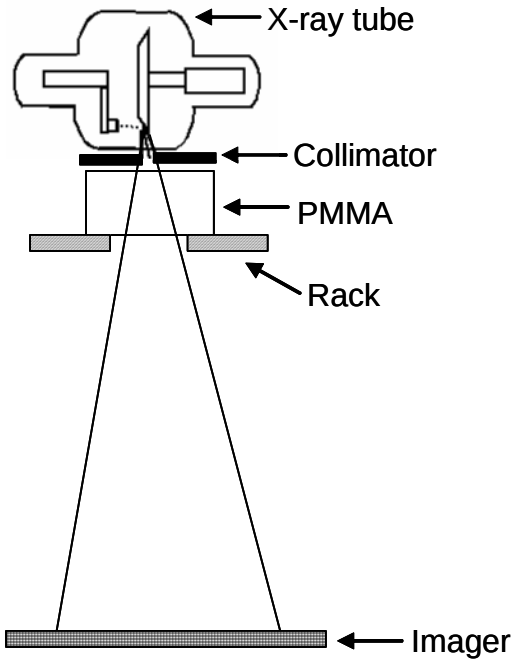

Figure 8.1. *Schematic representation of the image acquisition geometry.*

The focal spot to detector cover plate distance was maintained at 65 cm. No anti-scatter grid was used for any of the measurements. A schematic representation of the x-ray imaging system is shown in Figure 8.1. The imager was operated in the 78 μm pixel mode at 6.865 frames per second. Synchronization between the x-ray generator and the prototype imager was not available, hence a radiographic mode was used throughout the study by setting the x-ray exposure time to 1 sec and capturing an image frame within this time period. Scintillators of thickness 150 and 450 μm were investigated in this study.

Linearity

System linearity measurements were performed using a 450 μm CsI:Tl scintillator. A 45 mm PMMA block was used in the beam path as shown in Figure 8.1. Images were acquired at various mAs settings, dark corrected and the mean signal value in digital units (DU) was computed for an ROI of size 256 x 256 pixles.

Exposure Measurements

The incident exposure was measured with a calibrated mammographic ionization chamber and exposure meter (MDH 1515, RadCal Corp., Monrovia, CA). The exposures were measured 4.5 cm above the imager cover plate and corrected using inverse square law. Lead sheets were placed below the chamber to minimize back scatter. The exposures were measured with and without 45 mm PMMA filtration in the beam path in order to obtain the exposures at breast entrance and imager entrance respectively.

Presampling *MTF(f)* Measurements

As described in chapter 5, the presampling $MTF(f)$, was measured using the slanted slit-technique (Fujita *et al* 1992). The slit was placed on contact with the imager cover plate to minimize magnification. No PMMA was used in the beam path for this measurement to minimize scatter effects.

***NPS(f)* Measurements**

The $NPS(f)$ estimation was performed as described in chapter 5. The geometry shown in Figure 8.1 was used for all $NPS(f)$ measurements. Anti-scatter grid was not

used for any of the $NPS(f)$ measurements and the collimator was adjusted to cover a single module of the imaging array. Measurements were performed for various exposures in the range 0.1-0.53 mR for the 450 μm thick CsI:Tl scintillator. In addititon, the $NPS(f)$ for the 150 μm thick scintillator was estimated at 0.53 mR. The dark $NPS(f)$ was also estimated in order to characterize the imager noise.

For $NPS(f)$ estimation under x-ray exposure conditions, 16 "flood" images were acquired immediately after the acquisition of 16 "dark" images that were acquired at the same exposure time period but without x-rays. All acquisitions were made in the single frame (radiographic) mode. Since automatic synchronization between the CCD and the x-ray system was not available, an exposure time of 1 sec was set on the x-ray system. The CCD frame acquisition time for a single frame was 0.145 sec and this ensured complete capture of the x-rays by the imager. Offset correction was performed by subtracting each dark frame from a subsequently acquired flood image frame. A region of interest (ROI) consisting of 768 x 768 pixels was cropped from each image. Bad pixel correction did not have a major impact as the number of bad pixels was very few in the imager. The images were then flat-field corrected by dividing each image ROI by an average ROI image and scaling the result by the mean value of the average ROI image.

For each experimental condition, nine, non-overlapping 256 x 256 pixel ROIs were extracted from each 768 x 768 pixel image resulting in 144 ROIs (16 x 9) that were used for $NPS(f)$ analysis. Preceding NPS estimation, the ROIs were trend corrected by fitting a two-dimensional polynomial surface fit to the data values in each ROI and subtracting it from the corresponding ROI (Samei and Flynn 2003). For the x-ray

exposure imager, $NPS(f)$ with and without fixed pattern structural components were estimated as (Dobbins *et al* 1995)

$$NPS_{raw}^{struc}(u,v) = \frac{\left\langle \left| FFT(\,difference\ ROI_{struc}(x,y)\right|^2 \right\rangle}{N_x N_y} \Delta_x \Delta_y \qquad [1]$$

where,

$$difference\ ROI_{Struc}(x,y) = ROI(x,y) - \mu_{ROI} \qquad [2]$$

and

$$NPS_{raw}^{No\ struc}(u,v) = \frac{\left\langle \left| FFT(\,difference\ ROI_{No\ struc}(x,y)\right|^2 \right\rangle}{N_x N_y} \Delta_x \Delta_y$$

where,

$$difference\ ROI_{No\ Struc}(x,y) = ROI(x,y) - \left\langle ROI(x,y) \right\rangle \qquad [3]$$

As before, Δ_x and Δ_y are the pixel sizes in x and y directions respectively, and N_x and N_y are the number of elements in the x and y direction respectively, (N_x = 256, N_y = 256). In this case the NPS was corrected for the loss in variance introduced due to the background subtraction procedure in Equation 3 (Granfors and Aufrichtig 2000, Floyd *et al* 2001). The NPS was analyzed both along the serial and parallel read directions of the prototype imager. Normalization was performed as described in chapter 5 by dividing the raw $NPS(f)$ by the square of the mean DU of the corresponding average image ROI.

DQE(f) Measurements

The $DQE(f)$ was computed from the measured $MTF(f)$ and $NPS(f)$ as

$$DQE(f) = MTF^2(f) \Big/ NPS_{norm}(f) q_0 \qquad [4]$$

where, q_0 is in photons/mm^2. The value of q_0/X where X is the exposure (mR) was computed based on the definition of Roentgen (Johns and Cunningham 1983). In order to obtain the exposure/frame on the detector, the measured exposure was scaled by the frame time (0.145 sec) and distance at which the imager was located from the focal spot.

Results

The signal response of the system is shown in Figure 8.2. The linear nature of the system is evident in the mAs range investigated in this study. The measured exposures

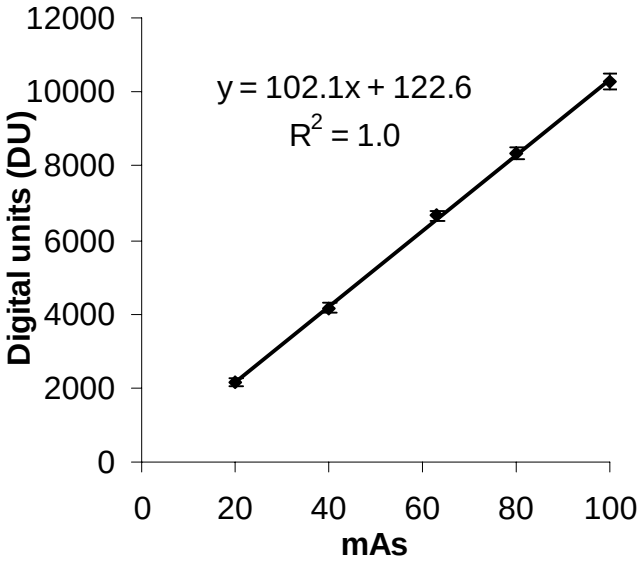

***Figure 8.2**. System signal response for different mAs conditions with 45 mm PMMA in the x-ray beam path.*

with no PMMA at 4.5 cm above the imager cover plate with a 1 sec exposure time, and the exposure values scaled to match the frame time of the imager are shown in Figure 8.3a. The exposure per frame at the entrance of the imager past 45 mm of PMMA is shown in Figure 8.3b.

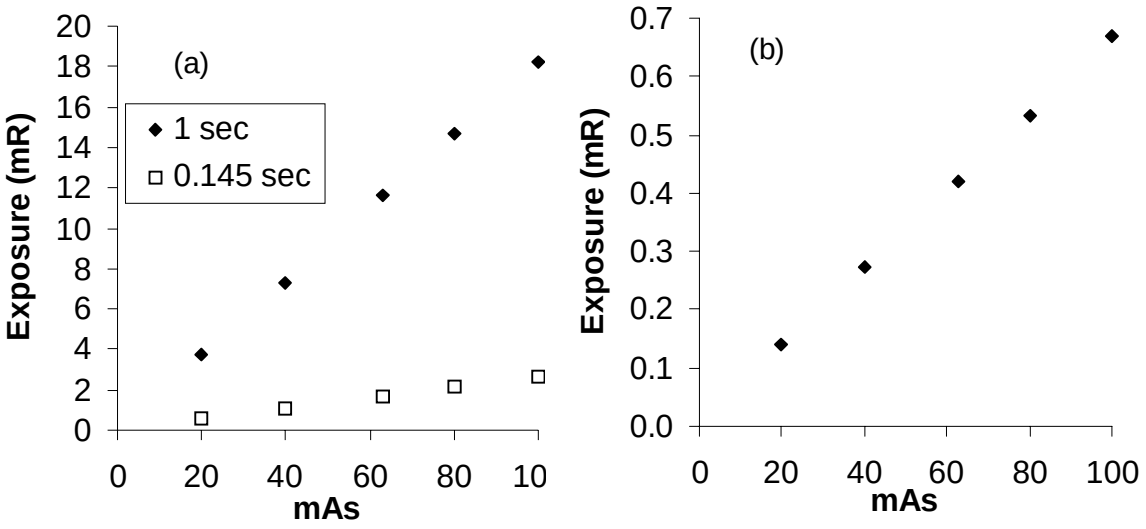

Figure 8.3. *(a) Measured exposures at 45 mm above the imager cover plate with a 1 sec exposure time and scaled to 0.145 sec to match the frame time of the imager. No PMMA was used in the x-ray beam path. (b) Measured exposures with 45 mm PMMA in the x-ray beam path and scaled to match the imager frame time (0.145 sec) and corrected to obtain the imager entrance exposures.*

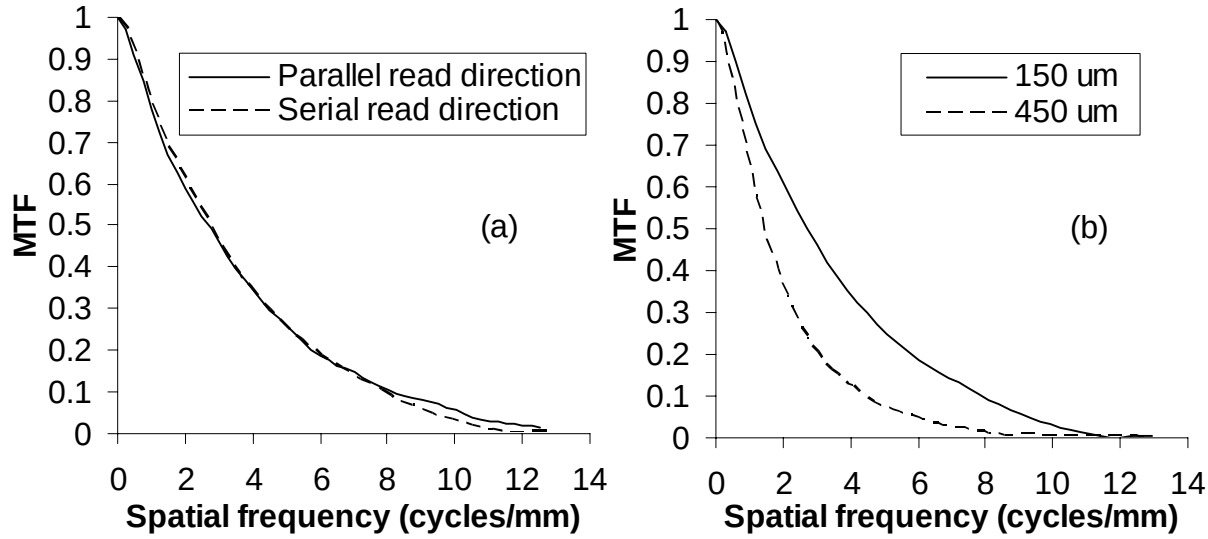

Figure 8.4. *(a) MTF(f) comparison for the 450 μm thick CsI:Tl scintillator along orthogonal directions. (b) MTF(f) characteristics of 150 and 450 μm CsI:Tl scintillators.*

The measured $MTF(f)$ characteristics of the imager along orthogonal directions and at two different scintillator thickness conditions are shown in Figure 8.4. The 2D NPS, $NPS(u,v)$ characteristics of the imager for the 150 and 450 μm thick Cs:Tl scintillator exhibits good symmetry (Figure 8.5).

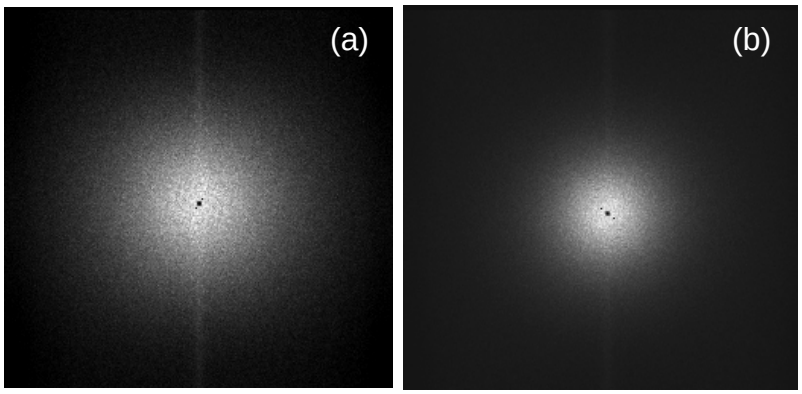

Figure 8.5. *Two-dimensional NPS characteristics of the (a) 150 and (b) 450 μm CsI:Tl scintillators at 0.53 mR.*

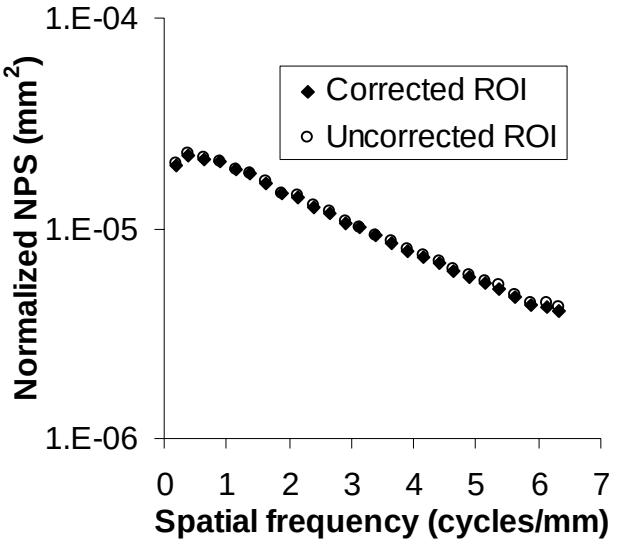

Figure 8.6. *Comparion of NPS(f) with and without bad pixel correction for the 150 μm thick CsI:Tl scintillator at 0.53 mR.*

The $NPS(f)$ of the system with and without bad pixel correction for a 150 μm thick CsI:Tl scintillator is shown in Figure 8.6. The impact of bad pixels appears to be negligible.

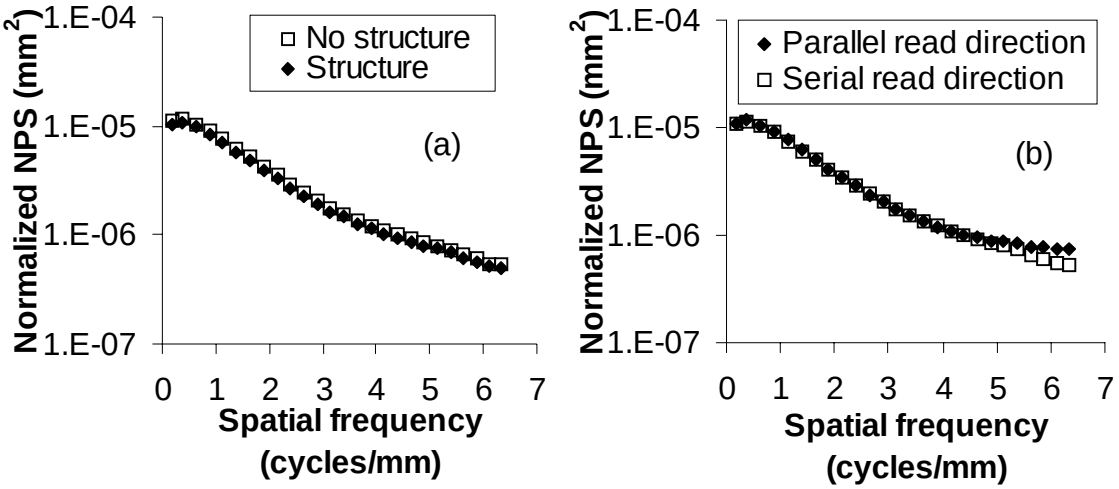

Figure 8.7. *Estimated NPS(f) with the 450 μm thick CsI:Tl scintillator (a) with and without structure removal and (b) along parallel and serial CCD read directions at 0.53 mR.*

The $NPS(f)$ characteristics with the 450 μm thick CsI:Tl with and without structural pattern correction is shown in Figure 8.7a. The orthogonal $NPS(f)$ characteristics are shown in Figure 8.7b. It appears that there is practically no effect of fixed pattern structure or charge read direction on $NPS(f)$ under the conditions investigated.

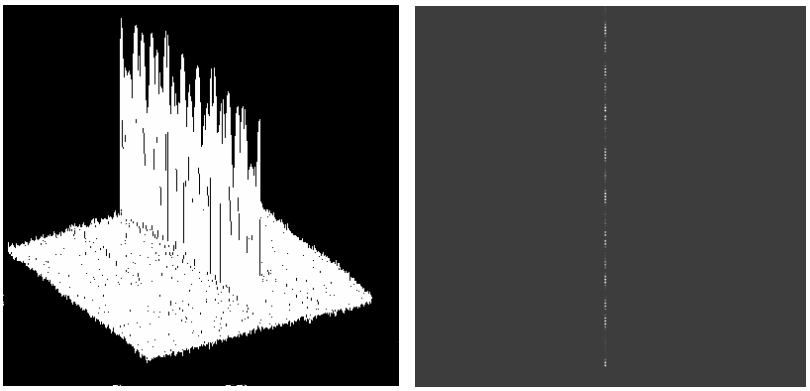

Figure 8.8. *Dark NPS(u,v) characteristics of the imager.*

The 2D dark NPS characteristics are shown in Figure 8.8. A surge in noise levels at very low frequencies is observed.

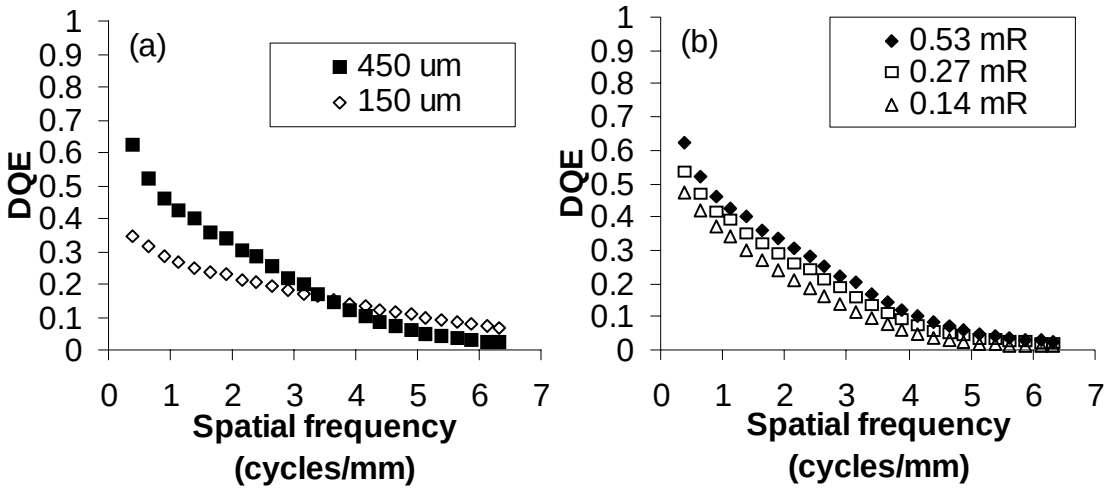

Figure 8.9. *(a) Effect of scintillator thickness and (b) exposure on the DQE(f) characteristics of the imager.*

The effect of scintillator thickness and entrance exposure on the $DQE(f)$ characteristics of the imager is shown in Figure 8.9a and Figure 8.9b respectively.

A schematic representation of the phantom used for qualitative assessment of imaging performance is shown in Figure 8.10. Images of the low-contrast iodine filled artery insert (Model 76-715, Fluke Biomedical, Cleveland, OH) acquired at 40 and 80 mAs is shown in Figure 8.11. The total thickness of the phantom was extended to 4.5 cm by adding PMMA blocks over the artery insert. The phantom comprised of 3 sets of vessels where each set had 4 vessels of diameter 0.5, 1, 2, and 4 mm. The concentration of iodine was 2.5, 5, and 10 mg/cm^3 for the three sets of vessels.

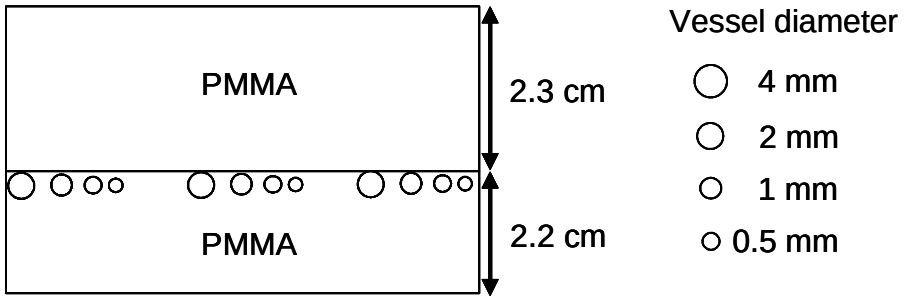

Figure 8.10. *Schematic representation of the low-contrast arterial phantom.*

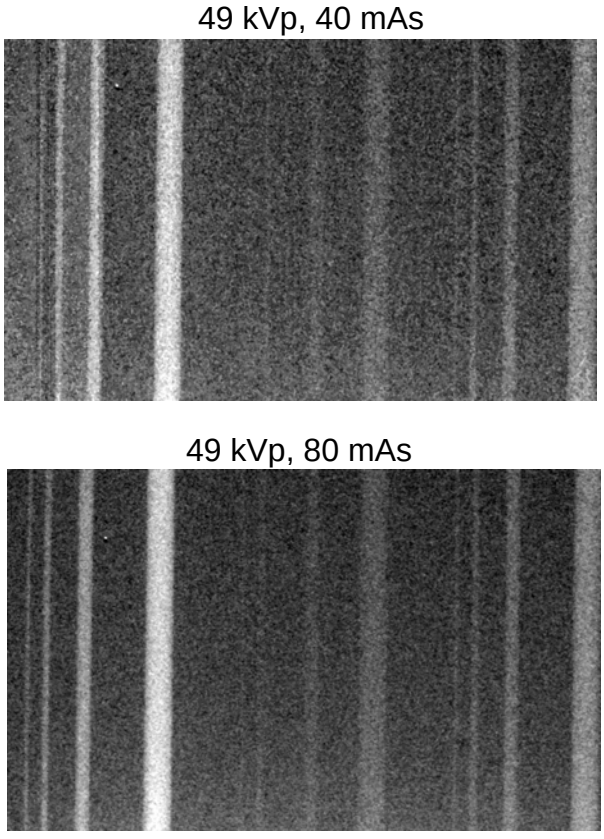

Figure 8.11. *Images of a arterial insert acquired at 49 kVp, W spectrum, and 0.6 mm Cu filtration at 40 and 80 mAs. The total thickness of the phantom was 45 mm.*

Discussion

The physical characteristics of the prototype system appear promising for contrast enhanced mammography. The response of the system is linear over the range of exposures (Figure 8.2) encountered in this study. Another interesting aspect of this study is the possibility of performing contrast enhanced mammography at much lower x-ray dose compared to conventional mammography. Under the conditions investigated, it appears that mean glandular dose levels below 0.5 mGy with 30 image frames can be effectively achieved. Further, with the 4.5 cm thick phantom and a CsI:Tl scintillator of thickness 450 μm, a $DQE(0)$ over 0.65 was achieved at 80 mAs or 0.53 mR per frame at the entrance of the imager (Figure 8.3b). The actual exposure per frame at 80 mAs was about 2 mR at 45 mm above the surface of the detector (breast entrance exposure). Recently reported kinetics of malignant masses in the breast indicate rapid uptake followed by washout (1-2 min) (Jong et al 2003). It also appears that a post-contrast acquisition of about 6-10 frames would suffice (Jong et al 2003). Based on these studies, it appears that with the imaging configuration of the prototype investigated in this study, mean glandular dose ~0.17 mGy with 10 frames and ~0.26 mGy with 15 frames are potentially attainable. These are extremely low dose levels compared to mammography as practiced today and with improved detector technology, further reduction in radiation dose can be envisioned.

The $MTF(f)$ characteristics of the imager along orthogonal directions are nearly identical and does not appear to be impacted by the interline structure (Figure 8.4a). The interline structure was present in the original design of the imager for fast framing applications such as cardiovascular imaging. However, based on the kinetics for contrast

enhanced mammography slower frame rates are likely to be adequate which would obviate the need for such interline structures. The reduction in $MTF(f)$ with increasing CsI:Tl thickness is primarily due to the greater spatial spreading of light in thicker scintillators (Figure 8.4b). However, for contrast enhanced mammography, very high spatial resolution may not be required due to higher contrast characteristics and thicker scintillators could be afforded. At the same time, the spatial resolution, similar to what was achieved with the prototype, could facilitate better visualization of angiogenesis.

The $NPS(u,v)$ characteristics of the prototype imager are symmetric showing nearly identical noise power distribution along all directions (Figure 8.5). The effect of ROI correction was negligible implying that the contribution of direct x-ray hits or bad pixels in the actual device was minimal (Figure 8.6). There appears to be no impact of fixed pattern and varying non-stochastic effects on the $NPS(f)$ of the system (Figure 8.7a), most likely due to the dominance of quantum noise over these effects. Further, the effect of charge readout direction on $NPS(f)$ is minimal (Figure 8.7b), implying a nearly uniform $NPS(f)$ along all directions. The surge in dark $NPS(f)$, near the low spatial frequencies could be attributed to the CCD clocking mechanism for charge transfer and readout (Figure 8.8).

The increase in $DQE(0)$ characteristics with an increase in scintillator thickness could be directly attributed to the increase in QE (Figure 8.9a). At higher frequencies, the frequency response of the system progressively dominates which causes the $DQE(f)$ of the 450 μm thick scintillator to decrease faster than the 150 μm thick scintillator (Figure 8.9a). The improvement in $DQE(f)$ characteristics with increasing exposure

could be attributed to the system becoming more quantum noise limited at higher exposures (Figure 8.9b). Further, an increase in signal level occurs at higher x-ray exposures. The image quality of the system appears to be good at 40 mAs (0.27 mR/frame at imager entrance) and 80 mAs (~0.53 mR/frame at imager entrance) exposures (Figure 8.10) with decrease in quantum noise observed at the higher exposure.

Conclusion

Based on the results of this study, a large-area, high-resolution digital imager with good performance characteristics for contrast enhanced mammography appears feasible. The prototype system exhibits $MTF(f)$ and $DQE(f)$ characteristics that is favorable for this application. It appears that a CsI:Tl scintillator of thickness 250-300 μm might suffice at the spectral conditions studied to achieve good spatial resolution and $DQE(f)$ characteristics. The mean glandular dose levels estimated in this study are encouraging. As a next step, a viable detector technology must be configured for this application. Ultimately, a well designed clinical study is crucial to determine the clinical benefit of contrast enhanced mammography.

CHAPTER 9

CONCLUSIONS

The major objectives of this project were to investigate new directions and applications for digital mammography. At this juncture, it is apparent that the results of this research extend far beyond the development of a device, but rather point towards key factors that could potentially impact the clinical performance of breast cancer detection. The combination of theoretical and experimental approaches facilitated the exploration of a range of system design and physical parameters for improved performance. As stated in the beginning of this manuscript, the main purpose was to demonstrate the desired characteristics of a digital x-ray imager for breast imaging using CCD as the platform technology. It should be noted that while the theoretical formulations and empirical studies conducted as part of this research revealed promising performance characteristics at the system level, the ultimate test is to conduct clinical studies under controlled conditions.

The findings of this study could open up new paradigms in the way we approach digital mammography. This research has successfully demonstrated that it is possible to develop large area high-resolution imaging architectures for digital mammography with favorable image quality characteristics. Based on the investigations performed in this research project, it was found that imagers with high $MTF(f)$ and $DQE(f)$ characteristics can be designed. Further, the theoretical formulations for digital mammography helped study a whole range of system parameters that could be used as a fundamental basis to enhance system performance or change design. The superior performance of the

prototype imager for digital mammography compared to a clinical FFDM, in terms of imager physical characteristics, was encouraging. A very interesting part of this research was the perceptual performance of the high-resolution prototype, which exhibited improved visual information at pixel sizes smaller than 100 μm under the conditions investigated. It was established through this research that improved detection with good detector SNR is possible at pixel sizes below 100 μm, which was considered sufficient for mammography. This could potentially open up the possibility of higher resolution imaging sensors being used for digital mammography than currently available. Another significant milestone that was achieved in this research study was the exploration of the feasibility of high-resolution contrast enhanced digital mammography at very low dose. The results suggest the possibility of improving contrast and visualization of soft tissue lesions. This research also demonstrated that imaging architectures such as those described in this work are viable for contrast enhanced digital mammography. Further, the theoretical and empirical physical characteristics of the imaging platform were very promising for this application. An interesting revelation of this study was the possibility of conducting contrast enhanced digital mammography at x-ray dose levels considerably lower than digital mammography while maintaining good contrast. Qualitative assessment of phantom images with iodinated material demonstrated good contrast and image quality. Other contrast agents based on gadolinium might also be suitable, but was beyond the scope of this study.

Although, the technical aspects and technology feasibility are of paramount importance, the clinical benefits must always be the ultimate objective. There are risks associated with injected contrast material. A recent article reports 1.1-1.2 deaths per

million due to contrast media (Wysowski and Nourjah 2006). However, such risks are low in conjunction with the potential benefits. There have been reports on the risk of cancer induction by low energy x-rays such as those encountered in mammography (Heyes and Mill 2004, Heyes *et al* 2006). However, there is currently no consensus on the induced cancer risk and even the studies that allude to the risk of cancer induction by mammography recommend cautious application of the procedure based on patient population. At the same time, other reports indicate benefit to risk ratios in the order of 100 to 1 for mammographic screening (Faulkner and Law 2006) and justify the importance of mammography in saving lives (Law and Faulkner 2001, Faulkner 2006). With further improvements in imager performance, it may be possible to attain higher benefit to risk ratios. In a recent article on image quality and dose, Busch and Faulkner (Busch and Faulkner 2006) illustrated the potential of dose reduction with digital systems due to their higher DQE characteristics compared to SF technology, based on phantom studies. If we assumed that the trends observed in the perception study in chapter 6 could be reproducible in a clinical setting, then a first order computation indicates that on average, about 40% dose reduction could potentially be achieved with the high-resolution prototype while equalizing the CD characteristics of the clinical FFDM system under the conditions investigated in the study.

The low mean glandular dose values from contrast enhanced digital mammography could potentially result in higher benefit/risk. The radiation risk factors reported for breast cancer screening (Faulkner and Law 2006) indicate a direct link between induced breast cancers and radiation dose with progressively decreasing risk with age. However, it should be noted that the induced cancers are in the order of 7-19

cancers per million per mGy (Faulkner and Law 2006). Based on this data any reduction in x-ray dose would reduce the risk, however the benefits of earlier and enhanced detection could far outweigh the impact of x-ray dose reduction. This beckons the need for novel approaches for breast imaging such as high-resolution digital mammography (Suryanarayanan *et al* 2005), contrast enhanced mammography (Skarpathiotakis *et al* 2002, Jong *et al* 2003, Lewin *et al* 2003), tomosynthesis (Niklason *et al* 1997, Niklason *et al* 1998, Suryanarayanan *et al* 2000, Wu *et al* 2003), and breast computed tomography (Boone *et al* 2001, Glick *et al* 2002, Ning *et al* 2004). The future of x-ray breast imaging is moving towards three-dimensions using imaging techniques such as tomosynthesis and computed tomography. The possibilities of injected contrast enhanced imaging of the breast in three-dimensions are also likely.

REFERENCES

ACS Breast cancer facts & figures 2005-2006
http://www.cancer.org/docroot/STT/stt_0.asp (Accessed on January 27, 2006)

Albagli D, Hudspeth H, Possin G E, Lee J U, Granfors P R and Giambattista B W 2003 Performance of advanced a-Si/CsI-based flat-panel x-ray detectors for mammography *Proc SPIE* **5030** 553-63.

Antonuk L E, el-Mohri Y, Siewerdsen J H, Yorkston J, Huang W, Scarpine V E and Street R A 1997 Empirical investigation of the signal performance of a high-resolution, indirect detection, active matrix flat-panel imager (AMFPI) for fluoroscopic and radiographic operation *Med Phys* **24** 51-70.

Antonuk L E, Jee K W, El-Mohri Y, Maolinbay M, Nassif S, Rong X, Zhao Q, Siewerdsen J H, Street R A and Shah K S 2000 Strategies to improve the signal and noise performance of active matrix, flat-panel imagers for diagnostic x-ray applications *Med Phys* **27** 289-306.

Arakawa S, Itoh W, Kohda K and Suzuki T 1999 Novel computed radiography system with improved image quality by detection of emissions from both sides of an imaging plate *Proc SPIE* **3659** 572-81.

Arakawa S, Itoh W, Kohda K and Suzuki T 2000 Improvement of image quality in CR mammography by detection of emissions from dual sides of an imaging plate *Proc SPIE* **3977** 590-600.

Arfelli F *et al* 1998 Low-dose phase contrast x-ray medical imaging *Phys Med Biol* **43** 2845-52.

Aslund M, Cederstrom B, Lundqvist M and Danielsson M 2004 Scatter rejection in scanned multislit digital mammography *Proc SPIE* **5368** 478-87.

Aufrichtig R 1999 Comparison of low contrast detectability between a digital amorphous silicon and a screen-film based imaging system for thoracic radiography *Med Phys* **26** 1349-58.

Aufrichtig R and Xue P 2000 Dose efficiency and low-contrast detectability of an amorphous silicon x-ray detector for digital radiography *Phys Med Biol* **45** 2653-69.

Bath M S, Sund P and Mansson L G 2002 Evaluation of the imaging properties of two generations of a CCD-based system for digital chest radiography *Med Phys* **29** 2286-97.

Birch R and Marshall M 1979 Computation of bremsstrahlung x-ray spectra and comparison with spectra measured with a Ge(Li) detector *Phys Med Biol* **24** 505-17.

Boone J M 2001 Determination of the presampled MTF in computed tomography *Med Phys* **28** 356-60.

Boone J M 2002 Normalized glandular dose (DgN) coefficients for arbitrary X-ray spectra in mammography: computer-fit values of Monte Carlo derived data *Med Phys* **29** 869-75.

Boone J M, Nelson T R, Lindfors K K and Seibert J A 2001 Dedicated breast CT: radiation dose and image quality evaluation *Radiology* **221** 657-67.

Boyle E R, Pak D and Williams J B 1999 Motion artifact seen on slot-scanning direct digital mammography *AJR Am J Roentgenol* **172** 697-701.

Bradford C D, Peppler W W and Dobbins J T, 3rd 1999 Performance characteristics of a Kodak computed radiography system *Med Phys* **26** 27-37.

Burgess A E 1995 Comparison of receiver operating characteristic and forced choice observer performance measurement methods *Med Phys* **22** 643-55.

Busch H P and Faulkner K 2006 Image quality and dose management in digital radiography: a new paradigm for optimisation *Radiat Prot Dosimetry* Epub ahead of print.

Chakraborty D P and Eckert M P 1995 Quantitative versus subjective evaluation of mammography accreditation phantom images *Med Phys* **22** 133-43.

Chan H P and Doi K 1983 Energy and angular dependence of x-ray absorption and its effect on radiographic response in screen-film systems *Phys Med Biol* **28** 565-79.

Chan H P, Lo S C, Niklason L T, Ikeda D M and Lam K L 1996 Image compression in digital mammography: effects on computerized detection of subtle microcalcifications *Med Phys* **23** 1325-36.

Chen B and Ning R 2002 Cone-beam volume CT breast imaging: feasibility study *Med Phys* **29** 755-70.

Cowen A R, Launders J H, Jadav M and Brettle D S 1997 Visibility of microcalcifications in computed and screen-film mammography *Phys Med Biol* **42** 1533-48.

Cranley K, Gilmore B J, Fogarty G W A and Desponds L 1997 Catalogue of diagnostic x-ray spectra and other data, Report No. 78, Institute of Physics and Engineering in Medicine.

Cunningham I A 1998 Linear-systems modeling of parallel cascaded stochastic processes: the NPS of radiographic screens with reabsorption of characteristic x-radiation *Proc SPIE* **3336** 220-30.

Cunningham I A and Reid B K 1992 Signal and noise in modulation transfer function determinations using the slit, wire, and edge techniques *Med Phys* **19** 1037-44.

Cunningham I A, Westmore M S and Fenster A 1994 A spatial-frequency dependent quantum accounting diagram and detective quantum efficiency model of signal and noise propagation in cascaded imaging systems *Med Phys* **21** 417-27.

Cunningham I A, Yao J and Subotic V 2002 Cascaded models and the DQE of flat-panel imagers: noise aliasing, secondary quantum noise, and reabsorption *Proc. SPIE* **4682** 61-72.

Dobbins J T, 3rd, Ergun D L, Rutz L, Hinshaw D A, Blume H and Clark D C 1995 DQE(f) of four generations of computed radiography acquisition devices *Med Phys* **22** 1581-93.

Drewery J S, Cho G, Fujieda I, Jing T, Kaplan S N, Perez-Mendez V, Wildermuth D and Street R A 1991 Amorphous silicon pixel arrays *Nucl Instrum Methods Phys Res A* **310** 165-70.

El-Mohri Y, Antonuk L E, Jee K W, Kang Y, Li Y, Sawant A R, Su Z, Wang Y, Yamamoto J and Zhao Q 2003 Evaluation of novel direct- and indirect-detection active matrix flat-panel imagers (AMFPIs) for mammography *Proc SPIE* **5030** 168-80.

Evans D S, Workman A and Payne M 2002 A comparison of the imaging properties of CCD-based devices used for small field digital mammography *Phys Med Biol* **47** 117-35.

Faulkner K 2006 Mammographic screening: is the benefit worth the risk? *Radiat Prot Dosimetry* Epub ahead of print.

Faulkner K and Law J 2006 Mammographic breast cancer screening for women previously treated with high breast doses for diseases such as hodgkin's *Radiat Prot Dosimetry* Epub ahead of print.

FDA Mammography Quality Standards Act of 1992 (MQSA) http://www.fda.gov/cdrh/mammography/robohelp/annual_equipment_qc_tests.htm (Accessed on March 1, 2006)

Fetterly K A and Hangiandreou N J 2001 Effects of x-ray spectra on the DQE of a computed radiography system *Med Phys* **28** 241-9.

Fetterly K A and Schueler B A 2003 Performance evaluation of a "dual-side read" dedicated mammography computed radiography system *Med Phys* **30** 1843-54.

Flanagan F L, Murray J G, Gilligan P, Stack J P and Ennis J T 1995 Digital subtraction in Gd-DTPA enhanced imaging of the breast *Clin Radiol* **50** 848-54.

Floyd C E, Warp R J, Dobbins J T, Chotas H G, Baydush A H, Voracek V R and Ravin C E 2001 Imaging characteristics of an amorphous silicon flat-panel detector for digital chest radiography. *Radiology* **218** 683-8.

Flynn M J and Samei E 1999 Experimental comparison of noise and resolution for 2k and 4k storage phosphor radiography systems *Med Phys* **26** 1612-23.

Fujita H, Tsai D Y, Itoh T, Doi K, Morishita J, Ueda K and Ohtsuka A 1992 A simple method for determining the modulation transfer function in digital radiography *IEEE Tran Med Imaging* **11** 34-9.

Gambaccini M, Taibi A, Del Guerra A, Marziani M and Tuffanelli A 1996 MTF evaluation of a phosphor-coated CCD for x-ray imaging *Phys Med Biol* **41** 2799-806.

Ganguly A, Rudin S, Bednarek D R and Hoffmann K R 2003 Micro-angiography for neuro-vascular imaging. II. Cascade model analysis *Med Phys* **30** 3029.

Ginzburg A and Dick C E 1993 Image information transfer properties of x-ray intensifying screens in the energy range from 17 to 320 keV *Med Phys* **20** 1013-21.

Glick S J, Vedantham S and Karellas A 2002 Investigation of optimal kVp settings for CT mammography using a flat-panel imager *Proc SPIE* **4682** 392-402.

Graeve T and Weckler G P 2001 High-resolution CMOS imaging detector *Proc. SPIE* **4320** 68-76.

Granfors P R and Aufrichtig R 2000 Performance of a 41X41-cm^2 amorphous silicon flat panel x-ray detector for radiographic imaging applications *Med Phys* **27** 1324-31.

Hall T J, Insana M F, Harrison L A, Soller N M and Schlehr K J 1995 Ultrasound contrast-detail analysis: a comparison of low-contrast detectability among scanhead designs *Med Phys* **22** 1117-25.

Hamamatsu The next generation of X-ray imaging devices series "ALS", "ACS", "FPS" http://hamamatsu.fr/assets/pdf/parts_misc/ALS_ACS_FOS.pdf (Accessed on February 8, 2006)

Hammerstein G R, Miller D W, White D R, Masterson M E, Woodard H Q and Laughlin J S 1979 Absorbed radiation dose in mammography *Radiology* **130** 485-91.

Hejazi S and Trauernicht D P 1997 System considerations in CCD-based x-ray imaging for digital chest radiography and digital mammography *Med Phys* **24** 287-97.

Hemdal B, Herrnsdorf L, Andersson I, Bengtsson G, Heddson B and Olsson M 2005 Average glandular dose in routine mammography screening using a Sectra MicroDose mammography unit *Radiat Prot Dosimetry* **114** 436-43.

Herron J M, Daxon E G, Gur D, Good F W, Maitz G S and Miller S L 1990 X-ray imaging with 2048 x 2048 CCD array *Proc SPIE* **1231** 374-80.

Herron J M, Kennedy W H, Gur D, Miller S L, Good F W, Good B C, Latchaw R E and Yonas H 1984 X-ray imaging with two-dimensional charge-coupled device (CCD) arrays *Proc SPIE* **486** 141-5.

Heyes G J and Mill A J 2004 The neoplastic transformation potential of mammography x-rays and atomic bomb spectrum radiation *Radiat Res* **162** 120-7.

Heyes G J, Mill A J and Charles M W 2006 Enhanced biological effectiveness of low energy x-rays and implications for the UK breast screening programme *Br J Radiol* **79** 195-200.

Hillen W, Eckenbach W, Quadflieg P and Zaengel P 1991 Signal-to-noise performance in cesium iodide x-ray fluorescent screens *Proc SPIE* **1443** 120-31.

Holdsworth D W, Gerson R K and Fenster A 1990 A time-delay integration charge-coupled device camera for slot-scanned digital radiography *Med Phys* **17** 876-86.

Hubbell J H and Seltzer S M 1997 Tables of X-Ray Mass Attenuation Coefficients and Mass Energy-Absorption Coefficients (verison 1.03) [On-line]. Available: http://physics.nist.gov/xaamdi. National Institute of Standards and Technology, Gaithersburg, MD, Report

Jacques S L 1998 Light distribution from points, line and plane sources for photochemical reactions and fluorescence in turbid biological tissues *Photochem Photobiol* **67** 23-32.

Jee K W, Antonuk L E, El-Mohri Y, Maolinbay M and Zhao Q 2001 Evaluation of direct detection and indirect detection active matrix flat-panel imagers (AMFPIs) for digital mammography *Proc SPIE* **4320** 13-23.

Jee K W, Antonuk L E, El-Mohri Y and Zhao Q 2003 System performance of a prototype flat-panel imager operated under mammographic conditions *Med Phys* **30** 1874-90.

Jing Z, Huda W and Walker J K 1998 Scattered radiation in scanning slot mammography *Med Phys* **25** 1111-7.

Johns H E and Cunningham J R 1983 *The physics of radiology* 4th edn (Springfield, Ill., U.S.A.: Charles C. Thomas).

Johns P C and Yaffe M 1987 X-ray characterization of normal and neoplastic breast tissues *Phys Med Biol* **32** 675-95.

Johns P C and Yaffe M J 1985 Theoretical optimization of dual-energy x-ray imaging with application to mammography *Med Phys* **12** 289-96.

Jong R A, Yaffe M J, Skarpathiotakis M, Shumak R S, Danjoux N M, Gunesekara A and Plewes D B 2003 Contrast-enhanced digital mammography: initial clinical experience *Radiology* **228** 842-50.

Kanno I, Maetki S, Aoki H, Nomiya S and Onabe H 2003 Low exposure x-ray transmission measurements for contrast media detection with filtered x-rays *J Nucl Sci Tech* **40** 457-63.

Karellas A, Harris L J, Liu H, Davis M A and D'Orsi C J 1992 Charge-coupled device detector: performance considerations and potenital for small-field mammographic imaging applications *Med Phys* **19** 1015-23.

Karellas A, Vedantham S and Suryanarayanan S 2004 Digital mammography image acquisition technology In: *Advances in Breast Imaging: Physics, Technology, and Clinical Applications, Categorical Course Syllabus* ed A Karellas and M L Giger (Oak Brook, IL: Radiological Society of North America) pp 87-99.

Kriege M *et al* 2004 Efficacy of MRI and mammography for breast-cancer screening in women with a familial or genetic predisposition **351** 427-37.

Law J and Faulkner K 2001 Cancers detected and induced, and associated risk and benefit, in a breast screening programme *Br J Radiol* **74** 1121-7.

Lawaczeck R, Diekmann F, Diekmann S, Bick U, Press W R, Schirmer H, Schon K and Weinmann H J 2003 New contrast media designed for x-ray energy subtraction imaging in digital mammography *Invest Radiol* **38** 602-8.

Lewin J M, D'Orsi C J, Hendrick R E, Moss L J, Isaacs P K, Karellas A and Cutter G R 2002 Clinical comparison of full-field digital mammography and screen-film mammography for detection of breast cancer *AJR* **179** 671-7.

Lewin J M, Hendrick R E, D'Orsi C J, Isaacs P K, Moss L J, Karellas A, Sisney G A, Kuni C C and Cutter G R 2001 Comparison of full-field digital mammography with screen-film mammography for cancer detection: results of 4,945 paired examinations *Radiology* **218** 873-80.

Lewin J M, Isaacs P K, Vance V and Larke F J 2003 Dual-energy contrast-enhanced digital subtraction mammography: feasibility *Radiology* **229** 261-8.

Liu H, Fajardo L L, Barrett J R and Baxter R A 1997 Contrast-detail detectability analysis: comparison of a digital spot mammography system and an analog screen-film mammography system *Acad Radiol* **4** 197-203.

Maidment A D, Yaffe M J, Plewes D B, Mawdsley G E, Soutar I C and Starkoski B G 1993 Imaging performance of a prototype scanned slot digital mammography system *Proc SPIE* **1896** 93-103.

Mainprize J G, Ford N L, Yin S, Gordon E E, Hamilton W J, Tumer T O and Yaffe M J 2002 A CdZnTe slot-scanned detector for digital mammography. *Med Phys* **29** 2767-81.

Metz C E and Vyborny C J 1983 Wiener spectral effects of spatial correlation between the sites of characteristic x-ray emission and reabsorption in radiographic screen-film systems *Phys Med Biol* **28** 547-64.

Mourad W G Average glandular dose in FDA-approved FFDM systems http://www.fda.gov/cdrh/mammography/scorecard-article10.html (Accessed on March 1, 2006)

Muller S 1999 Full-field digital mammography designed as a complete system *Eur J Radiol* **1** 25-34.

Nagarkar V, Tipnis S V, Gaysinskiy V B, Miller S R, Karellas A and Vedantham S New design of a structured CsI(Tl) screen for digital mammography *Proc SPIE* **5030** 541-6.

Neitzel U, Maack I and Kohfahl G S 1994 Image quality of a digital chest radiography system based on a selenium detector *Med Phys* **21** 509-16.

Niklason L T *et al* 1997 Digital tomosynthesis in breast imaging *Radiology* **205** 399-406.

Niklason L T, Kopans D B and Hamberg L M 1998 Digital breast imaging: tomosynthesis and digital subtraction mammography *Breast Dis* **10** 151-64.

Ning R, Yu Y, Conover D L, Lu X, He H, Chen Z, Schiffhauer L and Cullinan J 2004 Preliminary system characterization of flat-panel-detector-based cone-beam CT for breast imaging *SPIE* **5368** 292.

Nishikawa R M, Mawdsley G E, Fenster A and Yaffe M J 1987 Scanned-projection digital mammography *Med Phys* **14** 717-27.

Noel A and Thibault F 2004 Digital detectors for mammography: the technical challenges *Eur Radiol* **14** 1990-8.

Oestmann J W, Kopans D B, Hal D A, McCarthy K A, Rubens J R and Greene R 1988 A comparison of digitized storage phosphors and conventional mammography in the detection of malignant microcalcifications *Invest Radiol* **23** 725-8.

Ohara K, Doi K, Metz C E and Giger M L 1989 Investigation of basic imaging properties in digital radiography. 13. effect of simple structured noise on the detectability of simulated stenotic lesions *Med Phys* **16** 14-21.

Orel S G and Schnall M D 2001 MR imaging of the breast for detection, diagnosis, and staging of breast cancer *Radiology* **220** 13-30.

Pisano E D *et al* 2005 Diagnostic performance of digital versus film mammography for breast-cancer screening *N Engl J Med* **353** 1773-83.

Pisano E D *et al* 2000 Human breast cancer specimens: diffraction-enhanced imaging with histologic correlation--improved conspicuity of lesion detail compared with digital radiography *Radiology* **214** 895-901.

Rabbani M, Shaw R and Van Metter R 1987 Detective quantum efficiency of imaging systems with amplifying and scattering mechanisms *J Opt Soc Am A* **4** 895-901.

Raptopoulos V, Baum J K, Hochman M, Karellas A, Houlihan M J and D'Orsi C J 1996 High resolution CT mammography of surgical biopsy specimens *J Comput Assist Tomogr* **20** 179-84.

Roehrig H, Fajardo L L, Yu T and Schempp W V 1994 Signal, noise, and detective quantum efficiency in CCD-based x-ray imaging systems for use in mammography *Proc SPIE* **2163** 320-32.

Rong X J *et al* 2002 Microcalcification detectability for four mammographic detectors: flat-panel, CCD, CR, and screen/film) *Med Phys* **29** 2052-61.

Rosenberg R D, Hunt W C, Williamson M R, Gilliland F D, Wiest P W, Kelsey C A, Key C R and Linver M N 1998 Effects of age, breast density, ethnicity, and estrogen replacement therapy on screening mammographic sensitivity and cancer stage at diagnosis: review of 183,134 screening mammograms in Albuquerque, New Mexico *Radiology* **209** 511-8.

Rosenberg R D, Lando J F, Hunt W C, Darling R R, Williamson M R, Linver M N, Gilliland F D and Key C R 1996 The New Mexico Mammography Project: Screening Mammography Performance in Albuquerque New Mexico, 1991 to 1993 *Cancer* **78** 1731-9.

Rowlands J A, Hunter D M and Araj N 1991 X-ray imaging using amorphous selenium: a photoinduced discharge readout method for digital mammography *Med Phys* **18** 421-31.

Rowlands J A, Ji W G and Zhao W 2001 Effect of depth-dependent modulation transfer function and K-fluorescence reabsorption on the detective quantum efficiency of indirect-conversion flat-panel x-ray imaging systems using CsI *Proc SPIE* **4320** 257-67.

Rowlands J A and Taylor K W 1983 Absorption and noise in cesium iodide x-ray image intensifiers *Med Phys* **10** 786-95.

Ruschin M, Hemdal B, Andersson I, Borjesson S, Hakansson M, Bath M, Grahn A and Tingberg A 2005 Threshold pixel size for shape determination of microcalcifications in digital mammography: a pilot study *Radiat Prot Dosimetry* **114** 415-23.

Samei E and Flynn M J 2003 An experimental comparison of detector performance for direct and indirect digital radiography systems *Med Phys* **30** 608-22.

Sanada S, Doi K, Xu X W, Yin F F, Giger M L and MacMahon H 1991 Comparison of imaging properties of a computed radiography system and screen-film systems *Med Phys* **18** 414-20.

Saunders R S, Jr., Samei E, Jesneck J L and Lo J Y 2005 Physical characterization of a prototype selenium-based full field digital mammography detector *Med Phys* **32** 588-99.

Schaetzing R, Fasbender R and Kersten P 2002 New high-speed scanning technique for computed radiography *Proc SPIE* **4682** 511-20.

Schnall M D 2001 Application of magnetic resonance imaging to early detection of breast cancer *Breast Cancer Res* **3** 17-21.

Schnall M D 2003 Breast MR imaging *Radiol Clin North Am* **41** 43-50.

Seibert J A, Boone J M, Cooper V N and Lindfors K K 2004 Cassette-based digital mammography *Technol Cacer Res Treat* **3** 413-27.

Shaber G S, Lockard C and Boone J M 1988 High-resolution digital radiography utilizing CCD planar array *Proc SPIE* **914** 262-9.

Shtern F 1992 Digital mammography and related technologies: A perspective from the National Cancer Institute Radiology **183** 629-30.

Shumak R S, Jong R A, Danjoux N M, Gunasekara A, Skarpathiotakis M and Yaffe M J 2001 Pilot clinical evaluation of digital subtraction mammography *Radiology* **221(P)** 339.

Siebert J A, Boone J M, Cooper V N and Lindfors K K 2004 Cassette-based digital mammography *Technol Cacer Res Treat* **3** 413-27.

Siewerdsen J H, Antonuk L E, el-Mohri Y, Yorkston J, Huang W, Boudry J M and Cunningham I A 1997 Empirical and theoretical investigation of the noise performance of indirect detection, active matrix flat-panel imagers (AMFPIs) for diagnostic radiology *Med Phys* **24** 71-89.

Siewerdsen J H 1998 Ph.D. Thesis, University of Michigan, Ann Arbor.

Siewerdsen J H, Antonuk L E, El-Mohri Y, Yorkston J, Huang W and Cunningham I A 1998 Signal, noise power spectrum, and detective quantum efficiency of indirect-detection flat-panel imagers for diagnostic radiology *Med Phys* **25** 614-28.

Skaane P, Young K and Skjennald A 2003 Population-based mammography screening: comparison of screen-film and full-field digital mammography with soft-copy reading--Oslo I study *Radiology* **229** 877-84.

Skarpathiotakis M, Yaffe M J, Bloomquist A K, Rico D, Muller S, Rick A and Jeunehomme F 2002 Development of contrast digital mammography *Med Phys* **29** 2419-26.

Smith S T, Bednarek D R, Wobschall D C, Jeong M, Kim H and Rudin S 1999 Evaluation of a CMOS image detector for low-cost and power medical x-ray imaging applications *Proc SPIE* **3659** 952-61.

Sonoda M, Takano M, Miyahara J and Kato H 1983 Computed radiography utilizing scanning laser stimulated luminescence *Radiology* **148** 833-8.

Stoutjesdijk M J *et al* 2001 Magnetic resonance imaging and mammography in women with a hereditary risk of breast cancer *J Natl Cancer Inst* **93** 1095-102.

Suryanarayanan S, Karellas A and Vedantham S 2004a Physical characteristics of a full-field digital mammography system *Nucl Instrum Methods Phys Res A* **- 533 -** 570.

Suryanarayanan S, Karellas A, Vedantham S, Baker S P, Glick S J, D'Orsi C J and Webber R L 2001 Evaluation of linear and nonlinear tomosynthetic reconstruction methods in digital mammography *Acad Radiol* **8** 219-24.

Suryanarayanan S, Karellas A, Vedantham S, Glick S J, D'Orsi C J, Baker S P and Webber R L 2000 Comparison of tomosynthesis methods used with digital mammography *Acad Radiol* **7** 1085-97.

Suryanarayanan S, Karellas A, Vedantham S and Onishi S K 2005 High-resolution imager for digital mammography: physical characterization of a prototype sensor *Phys Med Biol* **50** 3957-69.

Suryanarayanan S, Karellas A, Vedantham S, Ved H, Baker S P and D'Orsi C J 2002 Flat-panel digital mammography system: contrast-detail comparison between screen-film radiographs and hard-copy images *Radiology* **225** 801-7.

Suryanarayanan S, Karellas A, Vedantham S, Waldrop S M and D'Orsi C J 2004b A Perceptual Evaluation of JPEG 2000 Image Compression for Digital Mammography: Contrast-Detail Characteristics *J Digit Imaging*

Swank R K 1973 Absorption and noise in x-ray phosphors *J Appl Phys* **44** 4199-203.

Taibi A, Guerra D, Gambaccini M, Marziani M and Tuffanelli A 1997 Evaluation of a digital x-ray detector based on a phosphor-coated CCD for mammography *Nucl Instrum Methods Phys Res A* **A392** 210-3.

Tesic M M, Fisher Piccaro M and Munier B 1999 Full field digital mammography scanner *Eur J Radiol* **31** 2-17.

Thurfjell E L and Lindgren J A 1996 Breast cancer survival rates with mammographic screening: similar favorable survival rates for women younger and those older than 50 years *Radiology* **201** 421-6.

Tkaczyk E J, LeBlanc J, Nevin R, Kautz G, Albagli D, Sandrik J and Granfors P R 2001 Modeling the x-ray energy characteristics of DQE for full-field digital mammography *Proc SPIE* **4320** 570-81.

Trauernicht D P and Van Metter R 1988 The measurement of conversion noise in x-ray intensifying screens *Proc SPIE* **914** 100-16.

Trauernicht D P and Van Metter R 1990 Conversion noise measurement for front and back x-ray intensifying screens *Proc SPIE* **1231** 262-70.

Tuncbilek N, Unlu E, Karakas H M, Cakir B and Ozyilmaz F 2003 Evaluation of tumor angiogenesis with contrast-enhanced dynamic magnetic resonance mammography *Breast J* **9** 403-8.

Turhal N S, Dane F, Dede F, Gumus M, Yumuk P F, Cakalagaoglu F, Savci D, Karaman M, Gulluoglu B and Turoglu H T 2004 99m-Tc-MDP-Scintimammography in the evaluation of breast masses or tumor angiogenesis *Anticancer Res* **24** 1999-2006.

Ullman G, Sandborg M, Dance D R, Yaffe M and Alm Carlsson G 2005 A search for optimal x-ray spectra in iodine contrast media mammography *Phys Med Biol* **50** 3143-52.

Vedantham S, Karellas A and Suryanarayanan S 2004a Solid-state fluoroscopic imager for high-resolution angiography: parallel-cascaded linear systems analysis *Med Phys* **31** 1258-68.

Vedantham S *et al* 2000a Full breast digital mammography with an amorphous silicon-based flat panel detector: physical characteristics of a clinical prototype *Med Phys* **27** 558-67.

Vedantham S, Karellas A, Suryanarayanan S, D'Orsi C J and Hendrick R E 2000b Breast imaging using an amorphous silicon-based full-field digital mammographic system: stability of a clinical prototype *J Digit Imaging* **13** 191-9.

Vedantham S, Karellas A, Suryanarayanan S, Levis I, Sayag M, Kleehammer R, Heidsieck R and D'Orsi C J 2000c Mammographic imaging with a small format CCD-based digital cassette: physical characteristics of a clinical system *Med Phys* **27** 1832-40.

Vedantham S, Karellas A, Suryanarayanan S and Onishi S K 2004b Solid-state fluoroscopic imager for high-resolution angiography: physical characteristics of an 8 cm x 8 cm experimental prototype *Med Phys* **31** 1462-72.

Waechter D, Huang Z, Zhao W, Blevis I and Rowlands J A 1996 Characteristics of dual-gate thin-film transistors for applications in digital radiology *Can J Phys* **74** 131-4.

Wang J and Langer S 1997 A brief review of human perception factors in digital displays for picture archiving and communications systems *J Digit Imaging* **10** 158-68.

Warner E *et al* 2001 Comparison of breast magnetic resonance imaging, mammography, and ultrasound for surveillance of women at high risk for hereditary breast cancer *J Clin Oncol* **19** 3524-31.

Watt A C, Ackerman L V, Shetty P C, Burke M, Flynn M, Grodsinsky C, Fine G and Wilderman S J 1985 Differentiation between benign and malignant disease of the breast using digital subtraction angiography of the breast *Cancer* **56** 1287-92.

Watt A C, Ackerman L V, Shetty P C, Burke M, Flynn M, Grodsinsky C, Fine G and Wilderman S J 1986 Breast lesions: differential diagnosis using digital subtraction angiography *Radiology* **159** 39-42.

Williams M B, Mangiafico P A and Simoni P U 1999a Noise power spectra of images from digital mammography detectors *Med Phys* **26** 1279-93.

Williams M B, Simoni P U, Smilowitz L, Stanton M, Phillips W and Stewart A 1999b Analysis of the detective quantum efficiency of a developmental detector for digital mammography *Med Phys* **26** 2273-85.

Wu T *et al* 2003 Tomographic mammography using a limited number of low-dose cone-beam projection images *Med Phys* **30** 365-80.

Wu T, Zhang J, Moore R, Rafferty E, Kopans D, Meleis W and Kaeli D 2004 Digital tomosynthesis mammography using a parallel maximum-likelihood reconstruction method *Proc SPIE* **5368** 1-11.

Wu X and Liu H 2003 Clinical implementation of x-ray phase-contrast imaging: theoretical foundations and design considerations *Med Phys* **30** 2169-79.

Wysowski D K and Nourjah P 2006 Deaths attributed to x-ray contrast media on U.S. death certificates *AJR Am J Roentgenol* **186** 613-5.

Yaffe M, Nishikawa R, Maidment A and Fenster A 1988 Development of a digital mammography system *Proc SPIE* **914** 182-8.

Yaffe M J and Rowlands J A 1997 X-ray detectors for digital radiography *Phys Med Biol* **42** 1-39.

Yamada T, Ishibashi T, Sato A, Saito M, Saito H, Matsuhashi T and Takahashi S 2003 Comparison of screen-film and full-field digital mammography: image contrast and lesion characterization *Radiat Med* **21** 166-71.

Yao J and Cunningham I A 2001 Parallel cascades: New ways to describe noise transfer in medical imaging systems *Med Phys* **28** 2020-38.

Zhao W, Ji W G, Debrie A and Rowlands J A 2003 Imaging performance of amorphous selenium based flat-panel detectors for digital mammography: characterization of a small area prototype detector *Med Phys* **30** 254-63.

Zhao W, Ji W G and Rowlands J A 2001 Effects of characteristic x rays on the noise power spectra and detective quantum efficiency of photoconductive x-ray detectors *Med Phys* **28** 2039-49.

Zhao W and Rowlands J A 1997 Digital radiology using active matrix readout of amorphous selenium: theoretical analysis of detective quantum efficiency *Med Phys* **24** 1819-33.